Volume 69C
Number 3
July–Sept. 1965

Engineering and Instrumentation

U.S. DEPARTMENT OF COMMERCE

SECTION C

JOURNAL OF RESEARCH

NATIONAL BUREAU OF STANDARDS

Journal of Research
of the
National Bureau of Standards

C. Engineering and Instrumentation

JULY–SEPT. • 1965

VOLUME • 69C

NUMBER • 3

Editor: Martin Greenspan

Associate Editors: G. F. Montgomery, R. V. Smith

Publication dates:
Feb. 15, May 15, Aug. 15, Nov. 15, 1965

JOURNAL OF RESEARCH

The National Bureau of Standards Journal of Research reports research and development in the fields of activity shown at right. Also included from time to time are survey articles on topics closely related to the Bureau's scientific and technical program.

The Journal is published in four separate sections as follows:

A. Physics and Chemistry

Contains papers of interest primarily to scientists working in these fields. Issued six times a year. Annual subscription: domestic, $4.00; foreign, $4.75. Single copy, 70¢.

B. Mathematics and Mathematical Physics

Presents studies and computations designed mainly for the mathematician and the theoretical physicist. Issued quarterly. Annual subscription: domestic, $2.25; foreign, $2.75. Single copy, 75¢.

C. Engineering and Instrumentation

Reports research and development results of interest chiefly to the engineer and the applied scientist. Issued quarterly. Annual subscription: domestic, $2.25; foreign, $2.75. Single copy, 75¢.

D. Radio Science (formerly Radio Propagation)

Published in cooperation with U.S. National Committee of URSI. Presents papers in radio propagation, communications, and radio science generally. Issued monthly. Annual subscription: domestic, $9.00; foreign, $11.50. Single copy, $1.00.

The National Bureau of Standards is a principal focal point in the Federal Government for assuring maximum application of the physical and engineering sciences to the advancement of technology in industry and commerce. Its responsibilities include development and maintenance of the national standards of measurement, and the provisions of means for making measurements consistent with those standards; determination of physical constants and properties of materials; development of methods for testing materials, mechanisms, and structures, and making such tests as may be necessary, particularly for government agencies; cooperation in the establishment of standard practices for incorporation in codes and specifications; advisory service to government agencies on scientific and technical problems; invention and development of devices to serve special needs of the Government; assistance to industry, business, and consumers in the development and acceptance of commercial standards and simplified trade practice recommendations; administration of programs in cooperation with United States business groups and standards organizations for the development of international standards of practice; and maintenance of a clearinghouse for the collection and dissemination of scientific, technical, and engineering information.

Institute for Basic Standards. Electricity. Metrology. Heat. Radiation Physics. Mechanics. Applied Mathematics. Atomic Physics. Physical Chemistry. Laboratory Astrophysics.* Radio Standards Laboratory: Radio Standards Physics; Radio Standards Engineering.** Office of Standard Reference Data.

Institute for Materials Research. Analytical Chemistry. Polymers. Metallurgy. Inorganic Materials. Reactor Radiations. Cryogenics.** Office of Standard Reference Materials.

Central Radio Propagation Laboratory.** Ionosphere Research and Propagation. Troposphere and Space Communications. Radio Systems. Upper Atmosphere and Space Physics.

Institute for Applied Technology. Textiles and Apparel Technology Center. Building Research. Industrial Equipment. Information Technology. Performance Test Development. Instrumentation. Transport Systems. Office of Technical Services. Office of Weights and Measures. Office of Engineering Standards. Office of Industrial Services.

*NBS Group, Joint Institute for Laboratory Astrophysics at the University of Colorado.
**Located at Boulder, Colo.

U.S. DEPARTMENT OF COMMERCE
John T. Connor, Secretary
NATIONAL BUREAU OF STANDARDS
A. V. Astin, Director

Order all publications from the Superintendent of Documents
U.S. Government Printing Office, Washington, D.C., 20402.

Use of funds for printing this publication approved by the Director of the Bureau of the Budget (June 19, 1961).

JOURNAL OF RESEARCH of the National Bureau of Standards—C. Engineering and Instrumentation
Vol. 69C, No. 3, July-September 1965

Two-Terminal Dielectric Measurements Up to 6×10^8 Hz

Martin G. Broadhurst and Anthony J. Bur

(February 23, 1965)

A two-terminal dielectric specimen holder has been constructed and used to make dielectric constant and loss measurements on a single disk specimen at room temperature over a frequency range from 10^{-2} to 6×10^8 Hz. The measurement procedures are outlined and a detailed analysis of the working equations and measurement errors is presented.

1. Introduction

It is often important for the study of dielectric properties that measurements be made on a single specimen using a minimum amount of the material over as wide a range of temperatures and frequencies as possible. Low-frequency measurements can conveniently be made on a single disk-shaped specimen, but at higher frequencies conventional equipment requires the use of cylindrical or rectangular specimens of various sizes to fit different microwave guides and cavities. If the dielectric properties of a material are sensitive to differences in specimen preparation, then the use of different specimens to cover the desired frequency range could lead to results which seriously misrepresent the frequency dependence of the dielectric constant and loss even though the individual measurements may themselves be quite accurate.

The two-terminal parallel-plate dielectric specimen holder described in this paper was designed to make measurements on single disk-shaped specimens (about 1 to 2 g of material) over as wide a range of frequencies as possible. Minimum specimen and holder size together with simplicity of construction and operation have been emphasized in order that the cell could easily be fitted with an insulating jacket and operated at temperatures from −200 to +200 °C. The variable temperature operation of the holder will be reported in a later paper.

In this paper, we will discuss the construction of the holder currently in operation at room temperature, and develop the equations for its use with the low-frequency Scheiber bridge [1],[1] the General Radio Models 716C Schering Bridge and 1615A Transformer Bridge, and the Boonton Radio Corporation Models 260A, 280A, and 190A Q-meters. Dielectric constant and loss data obtained with the holder for a disk of commercial poly(methyl methacrylate) over a frequency range of 10^{-2} to 6×10^8 Hz will be presented to illustrate the use of the holder. The experimental errors will be analyzed and discussed in detail. Use of the holder to measure liquid specimens is described in a separate paper [2]. Some of the measurement techniques used here are related to techniques described in a previous publication from this laboratory [3].

[1] Figures in brackets indicate the literature references at the end of this paper.

2. Design and Construction of Specimen Holder

A schematic diagram of the specimen holder is shown in figure 1. The case, cap, and electrodes are made of brass, gold-plated to reduce surface losses at high frequency. The lower electrode, which is operated at high potential, is supported and insulated from the case by a fused silica ring, which in turn is supported by the bottom rim on the holder case. The lower electrode and silica ring are held fixed by small beads of epoxy cement. The upper electrode is connected securely to a brass pin, finely threaded on the upper end to accommodate the spacing nut.

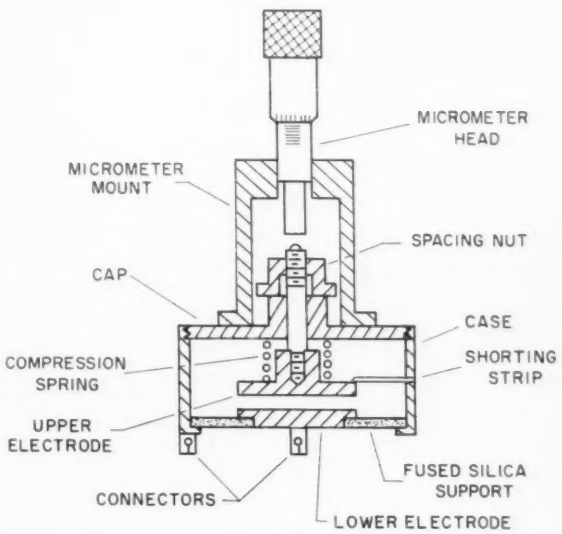

FIGURE 1. *A schematic diagram of the two-terminal dielectric specimen holder.*

The compression spring holds the spacing nut against the shoulder on the holder cap and rotation of the spacing nut raises or lowers the electrode and hence regulates the spacing. The spacing between the electrodes is determined by measuring the position of a steel ball, mounted at the top of the upper electrode assembly, with a micrometer barrel mounted rigidly to the holder cap. Electrical connection to the upper (ground potential) electrode is made by soldering four flexible gold foil strips between the upper electrode and case. Such an arrangement was preferred to conventional metal bellows mounting because of the former's shorter electrical path. Electrical connection to the holder is made through two connector caps soldered to the case and lower electrode, which fit snugly over pins suitably attached to the measuring equipment. The holder electrodes are 2.54 cm in diameter. The micrometer measures 10 μ per division and readings are estimated to 1 μ (1 $\mu = 10^{-6}$ m).

3. Theory of Measurements

Each dielectric constant and loss determination involves a specimen in and specimen out measurement of the holder impedance at the measurement frequency, and two calibration measurements of the empty bolder capacitance at some convenient audio frequency. The calibration measurements can either be done separately and compiled in the form of a curve of measured capacitance versus electrode spacing which is then applicable to all measurement frequencies, or they can be performed at the time of each determination with increased accuracy.

Figure 2 shows a schematic diagram of the two-terminal holder for the two measurement frequency conditions, together with the assumed equivalent circuit and the effective series resistance and capacitance of the cell. The symbols used in figure 2 are explained in table 1. The two audio-frequency calibration measurements can be represented in a way similar to figure 2b except that the effects of lead inductance can be ignored. When the measurement frequency is itself in the audio range then the general measurement procedure outlined here can be simplified as is described in the following section.

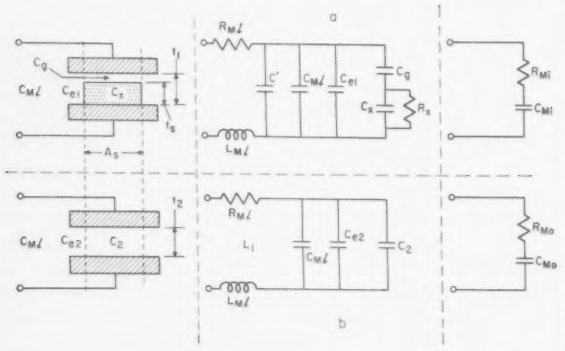

FIGURE 2. *A schematic representation of the two-terminal holder with (a) and without (b) a specimen and the corresponding assumed equivalent circuits.*

The symbols are defined in table 1.

TABLE 1. *Description of symbols used in text*

$C_x = \epsilon' \epsilon_0 \frac{A_s}{t_s}$ = equivalent parallel capacitance of the specimen.

$C_v = \epsilon_0 \frac{A_s}{t_s}$ = equivalent parallel vacuum capacitance of the specimen.

R_x = equivalent parallel resistance of the specimen.

$C_g = \epsilon_0 \frac{A_s}{t_1 - t_s}$ = capacitance of the airgap between the specimen and electrode.

$C_2 = \epsilon_0 \frac{A_s}{t_2}$ = capacitance berween adjacent areas A_s of the electrodes. C_1 corresponds to t_1.

C_c = the capacitance reading of the standard capacitor in a bridge when the cell is connected. C_{c1} corresponds to t_1 and C_{c_2} to t_2.

C_e = capacitance between the remainder of the electrodes including that portion outside the area A_s and the edges. C_{e_1} corresponds to spacing t_1 and C_{e_2} to t_2.

C_{Ml} = capacitance between the leads when the holder is in the measurement circuit.

C' = error capacitance due to distortion of the electric field (see discussion of errors).

R_{Ml}, L_{Ml} = equivalent resistance and inductance of holder leads when the holder is in the measurement circuit.

R_{Mi}, C_{Mi} = effective series resistance and capacitance of holder with specimen in.

C_{lc} = capacitance between the leads when the holder is in the calibration circuit.

Δf = the difference in frequency between the upper and lower half-power points of an L–C–R series resonant circuit.

R_{Mo}, C_{Mo} = effective series resistance and capacitance of holder with specimen out.

t_s, A_s = thickness and area of specimen.

t_1, t_2 = separation of electrodes at settings 1 and 2.

ϵ' = dielectric constant.

ϵ_0 = permittivity of free space.

ϵ'' = dielectric loss.

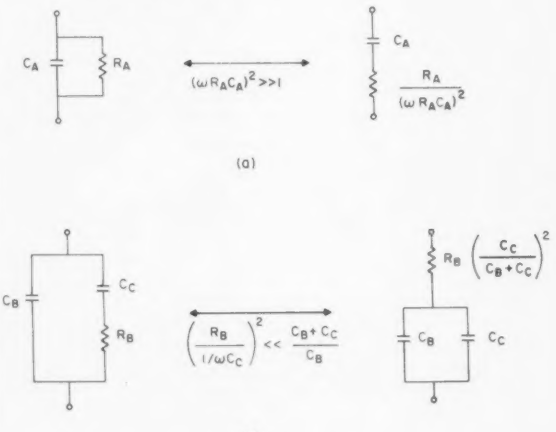

FIGURE 3. *Two simple transformations used to derive the working equations.*

In order to relate the equivalent circuits in figure 2 to their effective measured circuits, the approximate transformations shown in figure 3 were used. The approximations will be suitable for most low loss materials such as many polymers, glasses, and organic compounds. The validity criteria are shown in figure 3, and in general if $\epsilon''/\epsilon' < 0.1$ the transformation approximations will introduce less than 1 percent error in the results.

At the measurement frequency, the effective measured series capacitance and resistance of the holder with specimen in, C_{Mi} and R_{Mi}, and with specimen out, C_{Mo} and R_{Mo}, can be expressed as follows:

$$C_{Mi}=\frac{C_{Hi}}{1-\omega^2 L_{Mi} C_{Hi}} \tag{1}$$

$$R_{Mi}=R_{Mi}+\frac{R_x}{(\omega C_x R_x)^2}\left[\frac{C_x C_g}{C_{Hi}(C_x+C_g)}\right]^2 \tag{2}$$

$$C_{Mo}=\frac{C_{Ho}}{1-\omega^2 L_{Mi} C_{Ho}} \tag{3}$$

$$R_{Mo}=R_{Mi} \tag{4}$$

where

$$C_{Hi}=C'+C_{Mi}+C_{e_1}+\frac{C_x C_g}{C_x+C_g} \tag{5}$$

and

$$C_{Ho}=C_{Mi}+C_{e_2}+C_2. \tag{6}$$

One can write an expression for C_x which is independent of frequency or the type of electrical equipment used. If C_{Mo} is experimentally set equal to C_{Mi}, eqs (1) and (3) can be equated with the result,

$$C_x=\frac{C_g[C_2+(C_{e_2}-C_{e_1})-C']}{C_g-[C_2+(C_{e_2}-C_{e_1})-C']}. \tag{7}$$

From the calibration measurements (circuits correspond to that of figure 2b ignoring the lead inductance),

$$C_{c_1}=C_{lc}+C_{e_1}+C_1$$

$$C_{c_2}=C_{lc}+C_{e_2}+C_2, \tag{8}$$

one finds

$$C_2+(C_{e_2}-C_{e_1})=(C_{c_2}-C_{c_1}+C_1), \tag{9}$$

which can be substituted into eq (7) to give

$$C_x=\frac{C_g[(C_{c_2}-C_{c_1})+C_1-C']}{C_g-[(C_{c_2}-C_{c_1})+C_1-C']}. \tag{10}$$

Writing C_g and C_1 in the numerator in terms of measured quantities and applying the definition of ϵ' one finds

$$\epsilon'=\frac{C_x}{C_v}=\frac{1}{C_v}\left[(C_{c_2}-C_{c_1})+\frac{\epsilon_0 A_s}{t_1}-C'\right] \times\left[1-\frac{t_1-t_s}{t_1}-\frac{(C_{c_2}-C_{c_1})}{C_g}+\frac{C'}{C_g}\right]^{-1}. \tag{11}$$

The last term in brackets is the airgap correction term whose value is close to unity. It should be noted that this airgap term will be used in this form throughout the text. The effect of the error capacitance C' is also small (see discussion of errors) and hence the value of ϵ' is primarily dependent on the difference between two empty holder capacitances measured at audio frequencies and on the sample dimensions and initial holder spacing.

Since the holder is a part of the measurement circuit when the specimen is both in and out of the holder, the lead losses R_{Mi} can be eliminated by combining eqs (2) and (4), giving,

$$\Delta R_M=R_{Mi}-R_{Mo}=\frac{C_x D_x}{\omega}\left[\frac{C_g}{C_{Hi}(C_x+C_g)}\right]^2 \tag{12}$$

or

$$\epsilon''=\frac{C_x}{C_v}D_x=\frac{\omega}{C_v}\Delta R_M\left[\frac{C_{Hi}(C_x+C_g)}{C_g}\right]^2. \tag{13}$$

Unfortunately, there is not a convenient way to make resistance substitutions for the specimen loss so that the calculation of R_x will depend on the particular methods used at the measurement frequency.

4. Measurement Procedure

4.1. Q-Meter Procedure of Measurement

For Q-meter measurements in the frequency range 10^5 Hz to 2.5×10^8 Hz, two Q-meters were used, the Boonton Radio 260A Q-meter (100 kHz to 20 MHz) and the Boonton Radio 190A Q-meter (20 MHz to 250 MHz). The measurement procedure used is as follows: The holder is mounted on top of the Q-meter and connected in parallel with the Q-meter capacitor, C_s, with the shortest possible leads. With the specimen in the holder, the circuit is brought to resonance by tuning the Q-meter capacitor, C_s, to C_s'. The values of C_s', the electrode spacing t_1, and the Q of the circuit with the specimen in the holder, Q_i, are recorded. The specimen is then removed from the holder and the electrode spacing is decreased until resonance is achieved while holding C_s fixed at C_s'. The electrode spacing t_2 and the Q of the circuit with the specimen out, Q_o, are recorded.

The two resonant situations, with the specimen in and with the specimen out, occur at the same frequency and the total capacitance in the resonant circuits must be the same in both cases. The value of the total capacitance, C_T, is taken as the value of C_s when the Q-meter is tuned to resonance with the holder removed.

For the Q-meter measurement, the circuits of figure 2 may be viewed in parallel with the Q-meter capacitance C_s'. Considering figure 2a, one finds that if C_{Mi} and R_{Mi} are placed in parallel with C_s' then the transformation of figure 3b can be used to reduce the circuit to a simple L–C–R series circuit, for which the total series capacitance, the total series resistance and the Q of the resonant circuit with the specimen in the holder, C_T, R_{si}, and Q_i, are given as

$$C_T = C_{Mi} + C_s', \tag{14}$$

$$R_{si} = R_{Mi}\left(\frac{C_{Mi}}{C_T}\right)^2, \tag{15}$$

and

$$1/Q_i = \omega R_{si} C_T \tag{16}$$

where C_{Mi} and R_{Mi} are defined by eqs (1) and (2).

Likewise, with the specimen out and with the holder at spacing t_2, the resonant circuit can be represented by figure 2b in parallel with C_s'. The total capacitance, the total series resistance and the Q of the resonant circuit with the specimen out of the holder, C_T, R_{so}, and Q_o, are given as

$$C_T = C_{Mo} + C_s', \tag{17}$$

$$R_{so} = R_{Mo}\left(\frac{C_{Mo}}{C_T}\right)^2 \tag{18}$$

and

$$1/Q_o = \omega R_{so} C_T, \tag{19}$$

where C_{Mo} and R_{Mo} are given by eqs (3) and (4).

Equating the expression for C_T in eqs (14) and (17) will yield eq (11) of the previous section for the measured value of ϵ'.

An expression for ϵ'' is obtained from the difference, $Q_i^{-1} - Q_o^{-1}$, using eqs (16) and (19). Thus,

$$\Delta\left(\frac{1}{Q}\right) = Q_i^{-1} - Q_o^{-1} = \frac{\omega R_x}{(\omega R_x C_x)^2}\left[\frac{C_x C_g}{C_{Hi}(C_x + C_g)}\right]^2\left(\frac{C_{Mo}}{C_T}\right)^2 C_T. \tag{20}$$

Rearranging, dividing through by C_v, and using $C_{Hi} = C_{Ho}$, one obtains,

$$\epsilon'' = \frac{1}{\omega R_x C_v} = \left[\frac{C_T}{C_v}\Delta\left(\frac{1}{Q}\right)\right]\left(\frac{C_{Ho}}{C_{Mo}}\right)^2\left(\frac{C_x + C_g}{C_g}\right)^2. \tag{21}$$

In the above equation, the term in brackets is the dominant term and it alone would be present if there were no airgap or lead inductance. The term $(C_{Ho}/C_{Mo})^2$ results from the effect of lead inductance, which becomes significant above 30 MHz (see eq (3)). The third term, $[(C_x + C_g)/C_g]^2$, is the airgap correction.

Equation (21) can be reduced to following working equation:

$$\epsilon'' = \frac{C_T}{\epsilon_o A_s/t_s}\Delta\left(\frac{1}{Q}\right)\left(\frac{C_{Ho}}{C_T - C_s'}\right)^2\left[1 - \frac{t_1 - t_s}{t_1} - \frac{C_{c_2} - C_{c_1}}{C_g} + \frac{C'}{C_g}\right]^{-2}. \tag{22}$$

In the above equation C_{Mo} has been replaced by $C_T - C_s'$ in accordance with eq (17). The capacitances, C_T and C_s', are obtained from the calibrated Q-meter capacitor. The capacitance C_{Ho} is obtained from the audio frequency calibration. Omitted from the above equations are the high-frequency corrections which must be applied to the values of Q and C_s as read from the 190A Q-meter. The manner in which these corrections are carried out is explicitly stated in the 190A Q-meter manual.

A more detailed description of Q-meter dielectric measurements may be obtained from a paper by Hazen [4] in which he shows how the Q-meter circuit may be adapted for the measurement of very low losses.

4.2. Two-Terminal Measurements at Audio Frequencies

The General Radio (GR) 716C Schering bridge was used for audio frequencies from 10^2 Hz to 10^5 Hz, and the GR 1615A transformer ratio arm bridge was used from 5×10^2 Hz to 2×10^4 Hz.

For audio frequencies the effects of the lead inductance can be ignored, and the circuits of figure 2 without the inductance are considered here. With these bridges one measures the dissipation factor and the effective series capacitance of the unknown. However, when $\epsilon''/\epsilon' < 0.1$ the series capacitance and the parallel capacitance of the unknown are equal (within 1 percent) and this case is treated here. For $\epsilon''/\epsilon' > 0.1$ the GR bridge manuals should be consulted.

If the holder and specimen are connected as a two-terminal device in an arm of the bridge and if the procedure of measurement which was used with the Q-meter is also used with the bridge, then the result for ϵ' is the same as eq (11) and

$$\epsilon'' = \frac{C_T}{C_v}(D_i - D_o)\left(\frac{C_x + C_g}{C_g}\right)^2, \tag{23}$$

where D_i and D_o are the dissipation factors with the specimen in and out of the holder, and C_T is the total capacitance in the arm of the bridge which contains the holder. Just as with the Q-meter measurement, C_T must be the same for the D_i and D_o measurements.

A variation on the above experimental procedure which utilizes the standard capacitor in the bridge is preferable when using a bridge circuit and null detector for a two-terminal measurement. First, a bridge balance is obtained with the specimen and holder in the bridge circuit. Then t_1, D_i, and the standard bridge capacitor reading C_{si} are recorded.

The sample is taken out of the holder. Keeping the spacing fixed at t_1, the capacitance of the standard capacitor, C_s, is varied to rebalance the bridge. The specimen-out values, C_{so} and D_o are recorded.

If a bridge measurement is made by changing the standard capacitor while holding the electrode spacing at t_1, then a distinction must be made between using the substitution method of measurement and using the bridge as a direct reading instrument. In the substitution method, the unknown is connected in parallel with the standard capacitor, whereas for the direct method the unknown is connected in the bridge arm electrically opposite the standard capacitor. The GR 1615A is most conveniently used to measure C and D directly. The substitution method is used with the GR 716C bridge by connecting a precision air ballast capacitor to the "unknown direct" terminals.

When the electrode spacing is t_1 for both "in" and "out" measurements and a direct measurement is made, the total capacitance in the unknown bridge arm will be different for the "in" and "out" balances. Let C_{Ti} and C_{To} be the total capacitance in the unknown bridge arm with the sample in and out of the holder respectively. For a direct measurement we have,

$$C_{Hi}=C_{Mi}+C_{c_1}+C'+\frac{C_xC_g}{C_x+C_g}, \tag{24}$$

$$C_{Ho}=C_{Mi}+C_{c_1}+C_1 \tag{25}$$

from which ϵ' can be calculated in terms of measurable quantities. Using $C_{Hi}-C_{Ho}=C_{si}-C_{so}$ we have for a direct measurement

$$\epsilon'=\frac{1}{\epsilon_0A_s/t_s}\left(C_{si}-C_{so}+\frac{\epsilon_0A_s}{t_1}-C'\right)\times\left[1-\frac{t_1-t_s}{t_1}-\frac{C_{si}-C_{so}}{C_g}+\frac{C'}{C_g}\right]^{-1} \tag{26}$$

and

$$\epsilon''=\frac{C_{Ti}}{\epsilon_0A_s/t_s}\left(D_i-\frac{C_{To}}{C_{Ti}}D_o\right)\left[1-\frac{t_1-t_s}{t_1}-\frac{C_{si}-C_{so}}{C_g}+\frac{C'}{C_g}\right]^{-2}. \tag{27}$$

For a direct measurement with the GR 1615A transformer bridge it is conveniently true that $C_{To}=C_{so}$ and $C_{Ti}=C_{si}$.

On the other hand, for the substitution measurement, $C_{To}=C_{Ti}=C_T$ and $C_{si}<C_{so}$. For ϵ' and ϵ'' we have,

$$\epsilon'=\frac{1}{\epsilon_0A_s/t_s}\left(C_{so}-C_{si}+\frac{\epsilon_0A_s}{t_1}-C'\right)\times\left[1-\frac{t_1-t_s}{t_1}-\frac{C_{so}-C_{si}}{C_g}+\frac{C'}{C_g}\right]^{-1} \tag{28}$$

and

$$\epsilon''=\frac{C_T}{\epsilon_0A_s/t_s}(D_i-D_o)\left[1-\frac{t_1-t_s}{t_1}-\frac{C_{so}-C_{si}}{C_g}+\frac{C'}{C_g}\right]^{-2} \tag{29}$$

where the bracketed term in eqs (26) to (29) is the airgap correction term. To obtain the total capacitance, C_T, in the unknown arm of the GR 716C Schering bridge a separate bridge measurement is necessary. During the "in" and "out" measurement the ballast capacitance, C_B, remains fixed at C_T. After the specimen holder has been disconnected, C_B is measured by switching the bridge to "direct" and balancing the bridge by changing the standard capacitor. The dial reading of the standard capacitor is calibrated by measuring a known C_B. The calibration should also include the 1 pF capacitance of the bridge terminals.

4.3. Measurements at Ultra-Low Frequencies

The Scheiber ultra-low-frequency bridge was used in the frequency range 10^{-2}Hz to 2×10^{2}Hz [1]. Although the bridge was designed for use with a three-terminal dielectric cell, we have found that it may be easily adapted for measurements with a two-terminal cell. Ordinarily the leads from the bridge to the electrodes are shielded at ground potential and the shield encompasses the entire cell. For the two-terminal holder the electrode leads are shielded but the shield is abandoned at the base of the holder where the electrodes connect. A shield around the entire cell was improvised by lowering an aluminum box over the holder and connecting the the box to ground.

The substitution method of measurement with the electrode spacing fixed at t_1 for the "in" and "out" bridge balance is used. Equations (22) and (23) of Scheiber's paper [1] in conjunction with the airgap correction term of this paper were used to calculate the capacitance and conductance of the unknown.

For measurements below 10 Hz the surface conductivity of the sample can become a problem. It can be eliminated by wiping and cleaning the edges of the sample and thereafter handling the sample with tweezers and by introducing dry nitrogen through one of the ports of the cell.

4.4. Self-Resonant Measurements

The two-terminal holder can be used up to 600 MHz by shorting the terminals with an appropriate length conductor and exciting the resulting circuit at its self-resonant frequency. The Boonton model 280A UHF Q-meter was used as a combined oscillator and detector. The oscillator was coupled to the holder through a variable attenuator by means of a single-loop inductive probe. The signal was picked up with a capactive probe and rectified to give a d-c voltage which was applied to a voltemeter in the model 280A. The voltmeter is calibrated in

full and half-power levels which can be conveniently checked by switching 3 dB into the inductive probe. The oscillator frequency was measured with a Hewlett Packard model 524C frequency meter and 540A transfer oscillator.

Measurements were made by placing the specimen in the holder and tuning the circuit by adjusting the oscillator frequency. The frequency corresponding to the half-power points is then determined and recorded along with the electrode spacing. The specimen is then removed and the circuit retuned by adjusting the holder electrode spacing. The frequencies corresponding to the half-power points are again measured and recorded. One or more additional measurements of electrode spacing and corresponding resonance frequency must be made in order to determine the change in capacitance with resonance frequency.

Calculations are based on eqs (1) through (6), where the terminals in figures 2a and 2b are shorted. Thus we treat the problem as a simple series $L_T C_T R_T$ circuit for which the dissipation factor D_T and total capacitance C_T are

$$D_T = \omega C_T R_T, \tag{30}$$

$$C_T = \frac{1}{\omega^2 L_T}. \tag{31}$$

One may obtain ϵ' from eq (11) and ϵ'' from eq (13) remembering that here $C_{Hi} = C_T$ and

$$\Delta D_M = D_{Mi} - D_{Mo} = \omega C_T (R_{Mi} - R_{Mo}). \tag{32}$$

Substituting (32) into eq (13) gives

$$\epsilon'' = \frac{C_T}{C_v} \Delta D_M \left(\frac{C_x + C_g}{C_g}\right)^2. \tag{33}$$

The ratio of the frequency separation of the half-power points to the resonance frequency is measured to obtain the dissipation factor. The total capacitance which cannot be measured directly can be obtained by differentiating eq (31) to obtain

$$\frac{dC_T}{df_M} = -\frac{2}{f_M} C_T. \tag{34}$$

Hence we can write

$$\epsilon'' = -\frac{dC_T}{df_M} \cdot \frac{\Delta f_i - \Delta f_0}{2C_v} \left(\frac{C_x + C_g}{C_g}\right)^2. \tag{35}$$

Since the only part of C_T which changes with spacing, t, is the calibration capacitance C_c of the holder one can write

$$\epsilon'' = -\frac{dt}{df_M} \cdot \frac{dC_c}{dt} \cdot \frac{\Delta f_i - \Delta f_0}{2C_v} \left(\frac{C_x + C_g}{C_g}\right)^2. \tag{36}$$

Finally

$$\epsilon'' = -\frac{dt}{df_M} \cdot \frac{dC_c}{dt} \cdot \frac{\Delta f_i - \Delta f_0}{2\epsilon_0 A_s / t_s} \times \left[1 - \frac{t_1 - t_s}{t_1} - \frac{C_{c2} - C_{c1}}{C_g} + \frac{C'}{C_g}\right]^{-2}. \tag{37}$$

5. Sample Data

In order to illustrate the results which can be obtained with the dielectric specimen holder described in this paper, room temperature measurements were made on two specimens machined from the same 2.54-cm-diam poly(methyl methacrylate) rod into disks of average thicknesses 0.3150 cm and 0.1577 cm. The disk faces were made flat and parallel to better than 10 μ and no contact electrodes were applied. Both specimens were kept at about 23 °C at a relative humidity of 50 percent for several months before being measured. The measuring techniques used are those described in detail in the previous sections, and the measurements on the two specimens over the whole frequency range took about 10 hr. Calculations of ϵ' and ϵ'' were done by hand. The results of the measurements are shown in figure 4 which is a plot of the values of ϵ' and ϵ'' versus log frequency for the 0.3150-cm-thick specimen of poly(methyl methacrylate).

The data for the two specimens measured were found to agree to within 1 percent for ϵ' and 5 percent for ϵ'' at all frequencies, and with just a few exceptions, the agreement was within 0.3 percent for ϵ' and 2 percent for ϵ'' over the frequency range covered. In addition, the highest frequency values, which are the most crucial as far as the magnitude of the circuit correction is concerned, agree with each other and with measurements made using a reentrant cavity [3] within 0.3 percent in ϵ' and 2 percent in ϵ''. Additional measurements made on specimens of polychlorotrifluoroethylene and fused silica gave results which were also accurate to within the limits claimed in this paper except for the loss in fused silica which could not be detected at high frequency.

6. Discussion of Measurement Errors

The two-terminal method described in this paper was intended to provide values of ϵ' and ϵ'' over the entire range of applicable frequencies without imposing rigid requirements on specimen preparation and cell construction. In addition to uncertainties in the quantities explicitly appearing in the working equations of the previous section, attention must be given to the assumptions and approximations upon which these equations are based, the errors due to which will appear in an error capacitance term C'.

The error capacitance (in fig. 2 and eq (5)) includes corrections to the ideal assumed capacitance

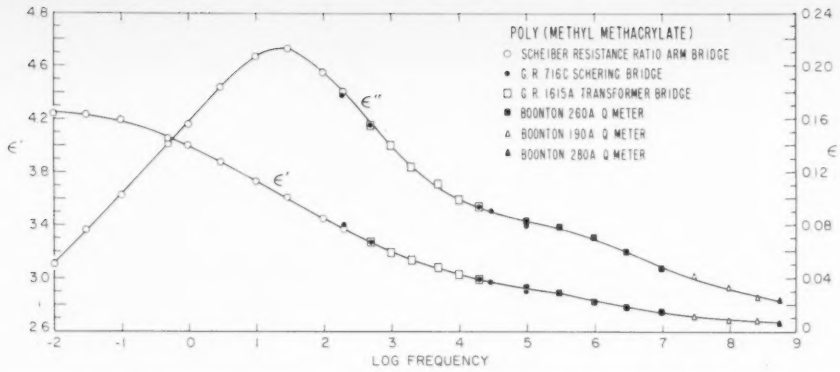

FIGURE 4. *The dielectric constant (ϵ') and loss index (ϵ'') of a 0.3150-cm-thick disk of commercial poly(methyl methacrylate) as a function of frequency as measured with the two-terminal dielectric specimen holder using various measuring equipment.*

resulting from distortions of the electric field between the measuring electrodes because of (a) tilted, misalined or nonflat electrode surfaces, (b) the presence of an airgap, (c) departure of the specimen geometry from an ideal right circular cylinder, (d) electrode edge effects, and (e) the presence of air between the electrodes.

(a) The errors due to nonideal electrodes are all second order effects with the actual capacitance given by

$$C=\epsilon'\epsilon_0\frac{A}{t}\left[1+0\left(\frac{\Delta}{t}\right)^2\right]$$

where A and t are the electrode area and separation and Δ represents the variation in t in the case of tilted or uneven electrodes or the distance between axes of the electrodes in the case of misalined electrodes. It is not difficult to keep mechanical errors to within 25 μ (25 μ=0.001 in.). With typical separations, t, of 1000 μ these errors amount to roughly $<$0.1 percent. In addition, the tilt error increases the capacitance whereas the misalinement error decreases it. Also since each determination of C involves a difference between two measurements, the effects tend to cancel. Thus the mechanical construction need not require special attention.

(b) The airgap causes some distortion of the field at the edge of the specimen (which increases with gap width and dielectric constant) and makes the actual capacitance higher than its uncorrected value. This in turn leads to a high value for the specimen capacitance C_x. An upper limit to this error ($\epsilon'=\infty$) for a typical measurement was calculated to be 0.2 percent [6], and one can reasonably conclude that in most cases the error from this source is $<$0.1 percent.

(c) Geometric imperfections in the specimen also lead to distortions. Rounded corners would cause an error similar to the airgap error. Uneven or nonparallel specimen surfaces lead to an actual capacitance greater than that assumed. The airgap capacitance is particularly affected by nonideal specimen surfaces. The specimen surface may well be tilted with respect to the adjacent electrode surface so that the airgap is a wedge of average thickness t=15 μ and variation Δ=10 μ. In this case the assumed airgap capacitance may be in error by 20 percent. (This calculation is based on the worst case—the capacitance of two concentric but mutually tilted circular disks in the limit of minimum separation.) Fortunately, the airgap capacitance enters the calculations in a very insensitive way so that an error of 20 percent in C_g would result in an error of perhaps 0.5 percent in C_x, and the error would be such as to increase the value of C_x above its true value. The geometry of the specimen does not appear to be particularly critical and special molding and machining techniques are not required.

(d) Electrode edge effects have been studied extensively [5]. With the specimen in place the edge capacitance is higher than one assumes and hence the calculated value of C_x is too high. In general, this error increases with ϵ' and also with the proximity of the specimen to the edge of the electrode. If the distance between the specimen and the electrode edges is twice the separation of the electrodes then this error is $<$0.1 percent [5]. Thus it is advisable to design the holder accordingly keeping in mind that measurement sensitivity decreases as the ratio of electrode area to specimen area increases, i.e., as C_x becomes a smaller part of the total capacitance.

(e) Since ϵ' for air is about 0.06 percent higher than assumed, then the actual capacitance with specimen removed is higher than calculated, thus lowering ϵ' by $<$0.1 percent. The effect on the airgap is negligible.

A final approximation of the accuracy of the measurements can be obtained from an estimate of the accuracy of the measured quantities in the working equations. Generally, the calibration capacitances can be measured to the nearest 0.1 percent, the linear dimensions to the nearest micron and the area of the sample using a traveling microscope to 0.02 percent. Considering eq (11) for ϵ' the factors and

their percent uncertainty are C_v, ±0.3 percent; $[(C_{c_2} - C_{v_1} + \epsilon_0 A_s/t_s - C']$, ±0.3 percent; the airgap correction term, ±0.5 percent. In eqs (22), (23), (27), and (29) for ϵ'', the factors and their percent uncertainty are C_T, ±0.2 percent; $\epsilon_0 A_s/t_s$, ±0.3 percent; $\Delta\left(\frac{1}{Q}\right)$, ±3 percent; $C_{Ho}/(C_T - C_x')$, ±0.3 percent; $(D_i - D_o)$, ±(0.5% +0.00005) for GR 1615A; $(D_i - D_o)$, ±(2% +0.0005) for GR 716C; and the airgap correction ±1 percent. For eq (37) the percent uncertainty of the terms are dt/df_M, ±0.5 percent; dC_c/dt, ±1 percent; and Δf_i and Δf_o, ±(0.2%+10kHz).

The total percent uncertainty for ϵ' and ϵ'' is obtained from the square root of the sum of the squares of the uncertainties in the working equations. For ϵ' the percent uncertainty is ±0.7 percent over the entire frequency range 10^{-2} to 6×10^8 Hz. For ϵ'' we have ±(1.5%+0.0005) for the ultra low frequency bridge, ±(1.8%+0.0005) for the GR 716C bridge, ±(0.6%+0.0001) for the GR 1615A bridge, ±(4%+0.0005) for the 260A and 190A Q-meters, and ±(1.6%+0.0005) for the self-resonant measurements.

7. References

[1] D. J. Scheiber, J. Res. NBS **65C** (Eng. and Instr.), No. 1, 23(1961).

[2] A. J. Bur, 1964 Annual Report of the Conference on Electrical Insulation, National Academy of Sciences-National Research Council Publication 1238, p. 70.

[3] A. H. Scott, D. J. Scheiber, A. J. Curtis, J. I. Lauritzen, Jr., and J. D. Hoffman, J. Res. NBS **66A** (Phys. and Chem.), No. 4, 269(1962).

[4] T. Hazen, Presented to the 13th Annual Wire and Cable Symposium, Atlantic City, New Jersey, December 2–4, 1964.

[5] A. H. Scott and H. L. Curtis, J. Res NBS **22,** 747(1939) RP 1217.

[6] J. I. Lauritzen, Jr., unpublished results.

(Paper 69C3–195)

JOURNAL OF RESEARCH of the National Bureau of Standards—C. Engineering and Instrumentation
Vol. 69C, No. 3, July–September 1965

Improved Ten-Picofarad Fused Silica Dielectric Capacitor[1]

R. D. Cutkosky and L. H. Lee

(March 8, 1965)

Some defects in a set of fused silica dielectric capacitors constructed in 1961 are listed, and methods for their reduction or elimination are described. The construction of a new set of capacitors completed in 1964 is described in detail. Preliminary stability data presented indicate that the typical drift of the 1964 capacitors with respect to their mean was less than two parts in 10^7 in five months.

1. Introduction

Capacitors utilizing fused silica as the dielectric have been under investigation at NBS and elsewhere [1][2] for many years. Early indications were that suitably constructed capacitors of this type would be at least as stable as air capacitors, and additionally would be sufficiently rugged to withstand shipment between laboratories.

A set of four fused silica dielectric 10-pF capacitors was constructed at NBS in 1961 [2]. The capacitance elements of these capacitors consisted of fused silica disks 7 cm in diameter and 1 cm thick. Silver electrodes were fired on the two faces of the disks and a third electrode was fired on the cylindrical surface. The cell in which the element was mounted shielded the face electrodes from each other in the region external to the fused silica element, and was connected electrically to the cylindrical electrode of the element. The housing contained a four-terminal resistance thermometer for temperature measurement and was hermetically sealed.

One of the 1961 capacitors was successfully hand-carried to several distant laboratories and returned. These laboratories included NRC (Canada), NPL (England), and NBS Boulder. The largest change in capacitance observed upon completion of the round trip was 0.2 parts in 10^6 (ppm). A shipment of this capacitor by commercial carrier was not successful and resulted in a change in its capacitance of 36 ppm. This change was traced to a sensitivity to severe mechanical shock.

The 1961 capacitors had a number of undesirable features, the shock sensitivity being by far the most important. Further investigation indicated that all of the capacitors in the set suffered from this flaw, and that the change in capacitance was caused by motion of the fused silica element in its cell. The element was supported in the cell by means of phosphor bronze springs which permitted motion of the element along the cell axis. The element could not return to its equilibrium position after displacement because of frictional forces between the cylindrical surface of the element and the spring contacts attached to the cell. This mechanism could not have caused a capacitance change if the direct electrical field between the face electrodes had been entirely within the fused silica. Unfortunately, the direct capacitance included a small contribution due to fields from the back of a face electrode which entered the fused silica element at the insulation gap between this face electrode and the cylindrical shield electrode, and terminated at the opposite face electrode. Motion of the element within its cell altered the leakage field and consequently changed the total direct capacitance.

A second flaw in the 1961 capacitors was a pronounced dependence of capacitance upon voltage. It was necessary to restrict the voltage applied to these capacitors to 10 V rms to reduce the measurement uncertainty from this cause below 0.1 ppm. Since sufficient sensitivity is available at this voltage to see one part in 10^7, the voltage dependence did not seriously limit measurement accuracy. An investigation into the mechanism of the voltage dependence was made, and it was found that the dependence could be almost eliminated by increasing the thickness of the fired silver electrodes. The evidence indicates that the existence of islands of silver on the dielectric surface which are not in good electrical contact with the body of the electrode is in some way responsible for the large voltage dependence. A similar effect has been observed in mica capacitors with fired or deposited silver electrodes [3].

Measurements of capacitance and dissipation factor as a function of frequency indicated a capacitance difference from 50 Hz to 20 kHz of about 25 ppm, with a maximum slope and a maximum dissipation factor at about 1600 Hz. The shape of the curve suggested a relaxation mechanism involving polar impurities in the fused silica. An investigation of several optical grades of fused silica disclosed that the use of a grade possessing exceptionally good ultraviolet transmission characteristics resulted in capacitors with very much smaller frequency dependencies and with dissipation factors not greater than 3×10^{-6} throughout the audio-frequency region.

Examination of the published optical characteristics for the various grades tested disclosed no correla-

[1] This work was supported in part by the Metrology Engineering Center, Bureau of Naval Weapons, Pomona, Calif.
[2] Figures in brackets indicate the literature references at the end of this paper.

tion between optical absorption and audio-frequency behavior. It is felt that the presence or absence of the audio-frequency relaxation phenomenon is an accidental result of the technique for producing fused silica. It is possible that changes in manufacturing technique which have no effect on the optical properties of the fused silica may greatly affect the audio-frequency characteristics.

The temperature coefficients of the 1961 capacitors were about 14 ppm/°C. The large values were believed to be the result of a large temperature coefficient of dielectric constant in fused silica. Resistance thermometers were built into the capacitor housings to eliminate the measurement uncertainties caused by unknown temperatures.

A set of twelve 10-pF fused silica dielectric capacitors was built in 1964. Care was taken to reduce greatly all of the flaws listed above. The capacitance elements were constructed of type II Suprasil,[3] and were supported in their cells by means of tightly fitting polytetrafluoroethylene (PTFE) rings. Care was taken to keep the gaps between the face electrodes and the cylindrical shield electrode as small as seemed consistent with operation up to 200 V rms. The voltage dependence of each capacitor was measured before final sealing, and the electrodes were replated when necessary. The 1964 capacitors are physically smaller and much lighter than the 1961 capacitors, but were not designed with this as a principal objective.

The construction of these new capacitors is described in some detail to allow their reproduction elsewhere. Some characteristics of the completed set are then presented.

2. Construction

2.1. Housing

A cross section of the capacitance standard is shown in figure 1. The exterior of the assembly is constructed entirely of stainless steel. The hermetically sealed region at the bottom containing the fused silica element is welded shut upon completion, and after baking, the container is filled with dry N_2 through a copper sealoff tube. Electrical connections are made to the capacitor element and to the four-terminal resistance thermometer by means of glass-Kovar seals soft soldered to the sealed compartment.

Electrostatic shields not shown in figure 1 isolate the two face electrode leads from each other and from the resistance thermometer leads. The face electrode leads pass through stainless steel tubes as shown to a pair of coaxial connectors located above the liquid level of a constant-temperature oil bath. The resistance thermometer leads are attached to four binding posts located below the liquid level. Details of the construction can be seen in figure 2.

[3] Available from Amersil Quartz Company.

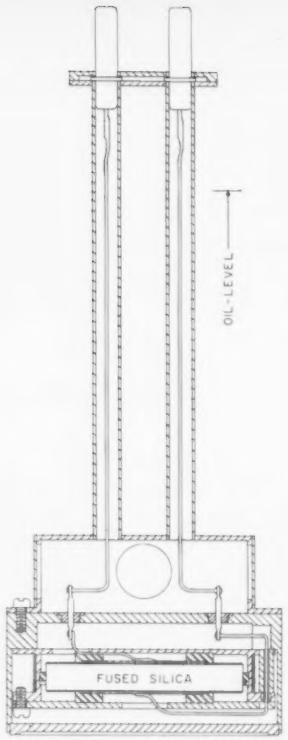

FIGURE 1. *Cross section of the capacitance standard.*

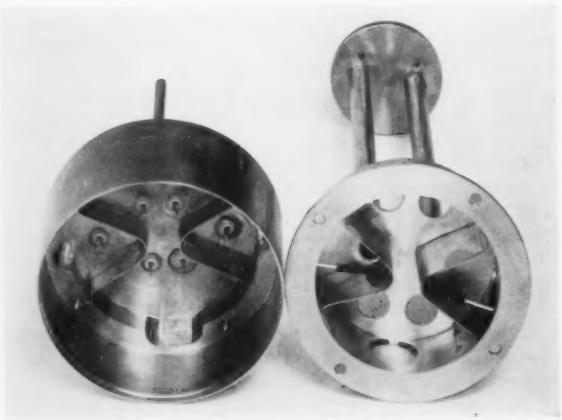

FIGURE 2. *Details of the capacitor housing and superstructure.*

The dimensions of the fused silica element and its mounting are shown in figure 3. The PTFE radial support is inserted into the slot of the brass cell before the inside diameter of the PTFE is finish machined. Each fused silica element is individually fitted to its cell by machining this radial support so

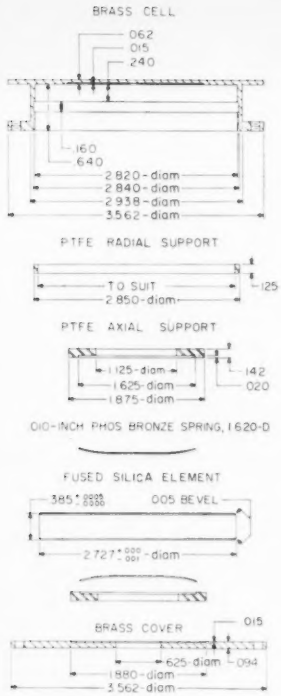

FIGURE 3. *Fused silica capacitance element and cell dimensions*

FIGURE 4. *Partially assembled capacitance element cell.*

that the element with its silver electrodes in place can just be removed from the cell with a rubber suction cup. The axial (vertical) constraint on the element is controlled by the use of shims or by machining, so that an axial interference of about 0.001 in. is obtained. This results in a slight compression of the PTFE axial supports.

Electrical connections to the face electrodes on the fused silica element are made by means of wires soldered to the phosphor bronze disk springs shown in figure 3. The disks are cut to the shape of an X and bent as shown in figure 4. Electrical connection between the cylindrical electrode and the cell is made by inserting three 0.030-in. diam phosphor bronze wires about 2 in. long into the circular gap between the cell and the element. The ends of these wires lie in the slot at the sides of the cell with the PTFE radial support. The three wires are positioned uniformly around the circumference of the cell and provide three points of electrical contact.

2.2. Resistance Thermometer

The four-terminal thermometer is located on the outside of the cell containing the fused silica element, as shown in figures 1 and 4. The cell is prepared by cementing a layer of linen cloth over it with shellac and baking at 100 °C. A length of B & S No. 36 Formvar insulated copper wire with a resistance of 25 Ω is doubled over and wound bifilarly over the linen. More shellac is then applied and baked. Leads to the current and potential terminals are connected to the resistance wire with soft solder. The junctions are tied down securely and shellac is applied. The completed thermometer is baked for 24 hr at 75 °C.

2.3. Fused Silica Element

The fused silica element is ground to the dimensions shown in figure 3 with conventional toolroom grinding equipment. Some care is necessary to prevent chipping of the edges. After inspection for chips, the element is cleaned with alcohol, and then with soap and water. It is next immersed in an ultrasonic cleaning bath containing a wetting agent, and rinsed with water. Finally, it is immersed in an ultrasonic cleaning water bath and rinsed with distilled water. After drying at 100 °C, Dupont Silver Paint #4666 is sprayed onto one face and the cylindrical surface, and allowed to air dry. The other face is then sprayed and dried, and the silver is fired onto the element at 480 °C. It is found that single silver deposits thicker than 0.0005 in. are often defective, and that a single application is not sufficient to prevent a dependence of capacitance upon voltage. A satisfactory remedy is to buff the electrode surface with fine steel wool and apply two additional coats of paint to the electrodes. The preferred final electrode thickness is between 0.0010 and 0.0015 in. If the electrode thickness is increased to 0.002 in., the large thermal expansion coefficient of the silver often causes the fused silica element to chip when it is

cooled from the firing temperature. No noticeable chipping occurs when the silver thickness is less than 0.0015 in.

After the third electrode coat has been fired, the edges of the element are very lightly beveled to separate the cylindrical electrode from the face electrodes. This is done by hand with a diamond wheel and a special jig, using water as a lubricant. Care must be taken at this point to avoid making the gap excessively wide and to remove all traces of silver from the beveled portions of the fused silica. If the diamond wheel is allowed to become contaminated with silver, a thin layer of silver will remain on the fused silica, and a large dependence of capacitance upon voltage will result.

The element is next fitted to its cell by machining the PTFE radial support. The element is then baked 24 hr in vacuum at 175 °C to eliminate adsorbed water, placed in its cell, and the cell is evacuated. The baking and evacuation are essential to produce a small dissipation factor and a stable capacitance.

After the capacitor has reached room temperature, it is measured and the adjustment necessary to produce exactly 10 pF at 25 °C is estimated. Using the element and cell dimensions shown in figure 3, the capacitance will probably not depart from 10 pF by more than ± 0.05 percent. An adjustment as small as this can be made quite easily by cutting a cavity into either a face or the cylindrical surface of the element with a small diamond wheel. The cavity is then sprayed with silver paint and refired. The adjustment sensitivity depends upon the diamond wheel diameter and thickness, the depth of cut, and the position of the cavity on the element. A jig may be readily set up to regulate depth of cut, and a calibration of capacitance change versus depth of cut measured with a trial element. Usually two or three successive adjustments suffice to produce a capacitance of 10 pF ± 50 ppm. A typical fused silica element after adjustment is shown in figure 5.

After final adjustment, a test is made for voltage dependence, and if necessary, the entire element is replated. The stainless steel housing is then welded shut, and the system is baked at 65 °C with a vacuum pump attached to the sealoff tube. After cooling, the housing is filled with dry N_2 at atmospheric pressure, and the sealoff tube is pinched off and soldered. A series of temperature cyclings is made between 50 and 0 °C, and the unit is placed into operation. Figure 6 shows a completed capacitor.

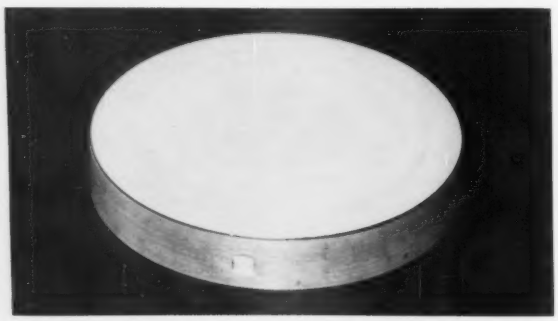

FIGURE 5. *Completed fused silica element with an adjustment of minus 50 ppm.*

3. Performance

3.1. Capacitance Stability

All measurements of capacitance stability reported here were made at 1592 Hz using a 10:1 bridge, with all capacitors in an oil bath maintained at 25.0 °C. The measurements seemed to indicate that these capacitors were at least as stable as any other capacitors in our laboratory. Accordingly, the mean of five of these capacitors, numbers 108, 109, 110, 112, and 113 was taken to be the basis for the comparisons. No temperature corrections were applied since the capacitors were at nearly the same temperature and had nearly identical temperature coefficients. The application of individual corrections for temperature slightly reduces the scatter in the measurement series reported below. Initially, all measurements were made with 10 V rms applied to the capacitors to allow ready comparison with the 1961 set of capacitors which had large voltage dependencies. Bridge readings were recorded under these conditions to the

FIGURE 6. *Completed capacitance standard.*

nearest part in 10^7. Beginning November 9, 1964, the new capacitors were intercompared at 100 V rms. This allowed considerably greater precision, but prevented simple comparison with the 1961 fused silica capacitors.

Capacitance differences between each capacitor in the set and the mean of the select five are listed in table 1. The table demonstrates that most of the capacitors are stable with respect to each other, but they could possibly all be drifting at the same rate. Comparisons of the 1964 set of capacitors with the 1961 set indicate no appreciable relative drifts, but conclusive proof of stability must await the completion of a new calculable capacitor.

TABLE 1. *Relative stability of eleven fused silica capacitors*

Decimal points indicate parts in 10^6.

Date	Capacitor										
	108	109	110	111	112	113	114	115	116	117	118
8/4/64	−2.5	+1.6	−28.3	+5.0	+18.2	+10.8					
8/4	−2.5	+1.6	−28.3	+5.0	+18.2	+10.9					
8/17	−2.5	+1.5	−28.3	+5.0	+18.3	+10.9	+31.5				
8/26	−2.5	+1.5	−28.3	+4.9	+18.2	+10.9	+31.5				
9/8	−2.6	+1.6	−28.2	+5.0	+18.2	+10.9	+31.5	+21.6	+15.6	−23.2	
9/11	−2.6	+1.5	−28.2		+18.2	+10.9	+31.6	+21.4	+15.5	−23.1	
9/22	−2.6	+1.5	−28.2		+18.2	+10.9	+31.5	+21.4	+15.6	−23.1	
10/5	−2.6	+1.5	−28.2		+18.2	+10.9	+31.5	+21.5	+15.6	−23.0	
10/20	−2.5	+1.6	−28.2		+18.2	+11.0	+31.6	+21.6	+15.8	−22.9	+6.1
10/22	−2.5	+1.6	−28.2		+18.2	+11.0	+31.5	+21.6	+15.8	−22.9	+6.1
10/30	−2.5	+1.6	−28.1		+18.2	+11.0	+31.5	+21.6	+15.8	−22.9	+6.1
11/5	−2.5	+1.5	−28.2		+18.2	+10.9	+31.5	+21.5	+15.7	−22.9	+6.1
11/9	−2.57	+1.58	−28.18		+18.19	+10.98	+31.49	+21.59	+15.76	−22.85	+6.23
11/16	−2.53	+1.57	−28.18		+18.18	+10.97	+31.46	+21.59	+15.73	−22.87	+6.20
11/24	−2.53	+1.54	−28.15		+18.10	+11.04	+31.38	+21.60	+15.67	−22.76	+6.22
11/30	−2.58	+1.55	−28.13		+18.11	+11.06	+31.40	+21.62	+15.69	−22.73	+6.26
12/7	−2.59	+1.56	−28.13		+18.12	+11.05	+31.41	+21.60	+15.68	−22.74	+6.24
12/14	−2.62	+1.56	−28.12		+18.12	+11.07	+31.41	+21.59	+15.68	−22.69	+6.27
12/21	−2.52	+1.55	−28.15		+18.08	+11.04	+31.37	+21.60	+15.66		+6.21
12/28	−2.56	+1.55	−28.14		+18.09	+11.06	+31.37	+21.56	+15.64	−22.70	+6.21
1/4/65	−2.51	+1.54	−28.15		+18.08	+11.04	+31.36	+21.54	+15.64	−22.69	+6.20
1/12	−2.50	+1.54	−28.15		+18.07	+11.04	+31.36	+21.56	+15.65	−22.68	+6.21
1/19	−2.50	+1.54	−28.15		+18.06	+11.04	+31.36	+21.56	+15.65	−22.68	+6.19
1/26	−2.50	+1.54	−28.15		+18.07	+11.04	+31.37	+21.56	+15.65	−22.67	+6.21

Capacitor number 117 exhibits a fairly steady increase of capacitance with time. The electrodes of this capacitor were about 0.002 in. thick. This capacitor also has a large voltage dependence of capacitance, as will be seen later. It is believed that the diamond wheel used to bevel the edges of the element was contaminated with silver.

3.2. Resistance Stability

Measurements of each resistance thermometer are plotted in figure 7. The effect of variations in the mean oil bath temperature was eliminated from the data by plotting the differences between each resistance and the mean of the resistances of capacitors 108, 109, 110, 112, and 113.

Figure 7 indicates that the resistance thermometers are quite stable relative to each other, but shows a flaw in our oil bath. Between September 20 and October 10, a blast of air from a fan was directed at the southwest corner of the oil bath, where capacitor number 115 was located. This blast of air introduced a temperature gradient of about 0.02 °C into the bath and is believed responsible for the relative variations observed on September 22 and October 5.

The stabilities of the copper resistance thermometers were determined from a series of measurements made with a Mueller bridge. A calibrated platinum resistance thermometer in conjunction with measured data for the dependence of the copper resistances upon temperature was used to refer all measurements

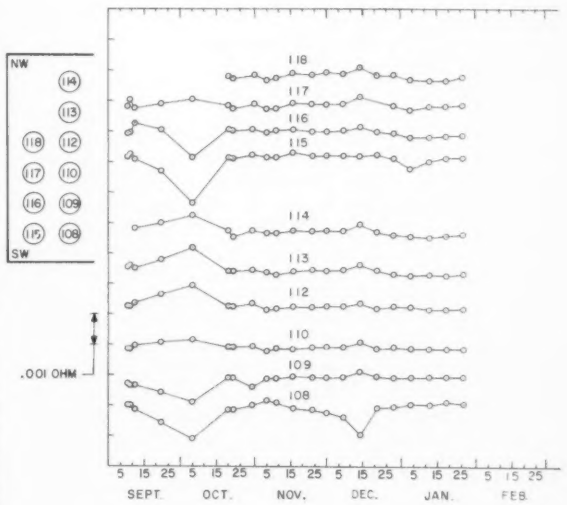

FIGURE 7. *Relative resistance thermometer stability.*

Insert shows relative positions in the oil bath. The southwest corner was abnormally cold between September 20 and October 10. A resistance change of 0.001 Ω corresponds to a temperature change of about 0.01 °C, or a capacitance change of about 0.1 ppm.

to a standard temperature. The limited information currently available indicates that the mean of the five selected resistances at a constant temperature has not changed more than 0.0001 Ω in 2 months. This corresponds to about 0.001 °C; or, referred to a capacitance correction, about 0.01 ppm.

3.3. Temperature Coefficients

The temperatures of the capacitance standards may be measured by means of the internal 25-Ω resistance thermometers. The capacitances at a specific temperature may then be determined if the capacitance temperature coefficients are known.

In practice, the temperature is usually treated as an implicit variable. A report of capacitance calibration then contains values for the capacitance and for the thermometer resistance at a temperature near 25 °C. A later measurement yielding a different thermometer resistance is corrected to the standard resistance thermometer value by reference to a plot of capacitance versus resistance for the standard.

Measurements of the capacitance-resistance function have been made over the temperature range 20 °C to 30 °C. The curves deviate from a straight line by about 2 ppm at the extremes and are all concave upwards. The slopes at 25 °C range from 100.4 ppm/Ω to 110.0 ppm/Ω. The actual capacitance temperature coefficients are about 10 ppm/°C which is substantially smaller than the 14 ppm/°C temperature coefficients of the 1961 fused silica capacitors. No explanation for this difference has been found.

3.4. Hysteresis

The capacitances of most air or solid dielectric standards at a given temperature depend upon the previous temperatures to which the standards have been subjected. Table 2 shows the magnitude of this hysteresis effect in the 1964 set of capacitors. Prior to September 8 all of the capacitors were subjected to a temperature of 50 °C, and then replaced in the oil bath at 25 °C. On September 8, their capacitances were measured with respect to a capacitor maintained at 25 °C throughout the experiment. Following these measurements, the capacitors were cooled to 0 °C, and then placed back into the oil bath. They were measured a second time on September 9. Table 2 shows that the capacitances increased an average of 0.28 ppm following the 0 °C treatment. A second subjection to 50 °C and a return to 25 °C resulted in the September 11 data in table 2. The capacitances returned most of the way to their original September 8 values, but an average capacitance increase of 0.06 ppm remained. Since the data were only recorded to the nearest part in 10^7, this overall change may not be real. The effect illustrated by table 2 represents one of the most serious faults in the capacitors, and one for which the mechanism is not completely understood. It is believed that the large differential expansion coefficient between the fused silica element and the silver electrodes may be partially responsible.

TABLE 2. *Dependence of capacitance upon prior thermal history*

September 8 and September 11 data were taken at 25 °C after subjection to 50 °C; September 9 data were taken at 25 °C after subjection to 0 °C (see text). Capacitance differences from the September 8 data are given in parts per million.

Capacitor	September 8	September 9	September 11
108	0	+0.15	+0.1
109	0	+.35	.0
110	0	+.45	+.1
112	0	+.35	+.1
113	0	+.25	+.1
114	0	+.25	+.1
115	0	+.35	−.1
116	0	+.35	.0
117	0	+.05	+.1
Mean change		+.28	+.06

3.5. Voltage Dependence

Some techniques and apparatus were developed recently at NBS for measuring the dependence of 100 and 1000 pF capacitors upon voltage, with uncertainties in the order of 1 part in 10^9 [4]. The equipment was used for measuring the voltage dependencies of the 10 pF capacitors with slightly larger uncertainties. Table 3 shows the capacitance differences observed when the voltage was changed from 100 V to 200 V. The computed probable error of the data in table 3 is 6 parts in 10^{10}, and the systematic error is estimated to be less than 2 parts in 10^9. Since the voltage dependence of a standard depends upon which electrode is at ground potential, all of the standards are marked with a "D" near the coaxial connector chosen for the ground potential lead.

TABLE 3. *Dependence of capacitance and dissipation factor upon voltage*

The increases in capacitance and dissipation factor due to increasing the voltage from 100 V to 200 V rms at 1592 Hz are shown.

Capacitor	$\frac{\Delta C}{C}$	$\frac{\Delta G}{\omega C}$
108	$+1.3\times10^{-9}$	-3.4×10^{-9}
109	−3.6	−2.2
110	−5.2	+1.2
112	−5.0	−4.6
113	−2.6	+0.6
114	−1.0	+1.0
115	+4.8	−0.1
116	−1.8	−.3
117	+12.4	−2.2
118	+9.8	−1.4

3.6. Frequency Dependence and Dissipation Factor

The result of comparing the fused silica capacitors with two 10 pF air capacitors at three frequencies is reported in table 4. Capacitor A was constructed with concentric cylindrical electrodes, and capacitor B with rigid parallel plates. Identical results were obtained at 159 Hz, using the two capacitors, but a significant difference was observed at 15900 Hz. The cause of the discrepancy is not known, but probably involves either mechanical resonances or excessive series inductances in one or both of the

air capacitors. The measurements at 159 Hz were extremely difficult to make due to poor bridge sensitivity. The computed probable error of the 159 Hz data in table 4 is 2×10^{-7}.

TABLE 4. *Frequency dependence of the fused silica capacitors relative to two air capacitors (see text)*

Capacitor	159 Hz	1592 Hz	15900 Hz A	15900 Hz B
	ppm		*ppm*	*ppm*
108	+1.3	0	−0.6	−1.9
109	+1.0	0	−.2	−1.5
110	+1.8	0	−.8	−2.1
112	+0.2	0	+.2	−1.1
113	+1.9	0	−.9	−2.2
114	+0.1	0	+.2	−2.1
115	+1.2	0	−.8	−3.1
116	+0.3	0	−.3	−2.6
117	+1.6	0	−1.2	−3.5
118	+1.8	0	−0.6	−1.9

Accurate measurements of dissipation factor cannot be made at NBS at this time. Comparisons of the fused silica dielectric capacitors with several types of air capacitors suggest that the dissipation factors of the fused silica capacitors are probably between 0 and $+3\times10^{-6}$ at 1592 Hz.

3.7. Shock Sensitivity

The capacitors were tested upon completion for shock sensitivity by dropping them onto a hardwood table. Various angles of impact and various heights up to 8 in. were tried. The largest capacitance change observed was 1 part in 10^7 which occurred when a capacitor fell about 8 in. in an upright position. Falls through smaller distances usually produced no observable change in capacitance.

3.8. Transportation Experiences

A fused silica dielectric capacitor designated number 107 and which was identical with those described in this paper was shipped to the National Research Council of Canada (NRC) on July 28, 1964, via air parcel post. Prior to shipment, it was compared with capacitor number 108. Number 108 was hand-carried to NRC and returned between August 4 and August 17, 1964, and again between December 8 and December 11, 1964. Comparisons of the two capacitors at NRC indicated no relative change in the two capacitances larger than 0.2 ppm; and as can be seen from table 1, no change in number 108 occurred during either of the two round trips.

4. Conclusion

Much more data is needed to evaluate conclusively the reliability of the 1964 set of fused silica dielectric capacitors. Existing evidence suggests that stabilities in the order of a few parts in 10^7 may be expected, and that the capacitors can probably withstand normal handling during shipment between laboratories.

Some further modifications of the design may result in an improved standard. A study of the mechanism which produces the capacitance hysteresis effect with large temperature changes would be of value, and consideration might be given to improving the support system for the fused silica element.

It is felt that the choice of 10 pF for a fused silica dielectric capacitor results in a design of nearly optimum stability. Other values would be useful as secondary standards and should not be difficult to construct.

5. References

[1] M. Kanno, Researches on standard capacitors, researches of the electrotechnical laboratory (Japan), No. 597, April 1961 (in Japanese).

[2] R. D. Cutkosky and L. H. Lee, The construction and behavior of a transportable ten picofarad capacitor, comite consulatif d'electricite, Aupres Du "Comite International Des Poids et Mesures," 10 Session 1963, p. 44.

[3] Standard capacitors and their accuracy in practice, Notes on Applied Science **13,** (NPL) 1955.

[4] J. Q. Shields, The voltage dependence of precision air capacitors, to be published.

(Paper 69C3–196)

JOURNAL OF RESEARCH of the National Bureau of Standards—C. Engineering and Instrumentation
Vol. 69C, No. 3, July–September 1965

Errors in the Series-Parallel Buildup of Four-Terminal Resistors

Chester H. Page

(April 20, 1965)

The use of n equal resistors (a) in series and (b) in parallel provides an n^2:1 ratio of potentially high accuracy. Such devices are important for extending the use of the national one-ohm standard to the hundred-ohm, and thence to the 10 000-ohm, level.

Formulas are derived for the error in the ratio, expressed (a) in terms of design tolerance, and (b) in terms of first-order residual misadjustments which combine to yield the second-order error of the ratio.

It seems feasible to construct a 1:100 ohm buildup device with a ratio uncertainty of less than 1 in 10^8.

The use of n equal resistors (a) in series and (b) in parallel provides an n^2:1 ratio of potentially high accuracy. Such devices are important for extending the use of the national 1-Ω standard to the 100-Ω, and thence to the 10 000-Ω level.

The first stage of this step-up involves the use of ten 10-ohm resistors, which must be four-terminal resistors to avoid large errors due to the connecting networks.

Hamon [1] has described an arrangement of four-terminal resistors permanently connected in series, and convertible to a parallel connection by adding jumpers. In that paper, he shows the use of compensating resistors in the potential leads to eliminate errors introduced by the added connections.

Compensated lead "fans" may be used for the potential terminals of the paralleled resistors, for the current terminals, or for *both*. The aim of the present paper is to present a complete analysis of the general case, and formulas for the errors introduced by imperfectly compensated fans.

[1] B. V. Hamon, A 100Ω build-up resistor for the calibration of standard resistors, J. Sci. Instr. **31**, 450–453 (Dec. 1954).

We consider four-terminal resistors connected in series by means of "tetrahedral" junctions, having the equivalent circuit shown in figure 1. Each junction supplies current and potential leads. This array can be converted to a parallel connection by adding four "terminal fans," as in figure 2. For analysis, the junction resistances can be considered as absorbed in the fan-conductor resistances. The problem is to make the four-terminal resistance of the combination precisely equal to R/n. If the resistances of the various arms of the current fan are adjusted to make each main resistor (R) carry identical current, the corresponding voltage drops will be identical and there will be no circulating current in the potential fans, and the potential across V_1-V_2 will be independent of the resistances of the potential fans, and equal to IR/n. This requires that each arm of the current fan on the left have the same resistance, say r, except for the top and bottom arms, each of which feeds only one main resistor. These end arms must have the resistance $2r$. For the right-hand current fan, each arm must have the same resistance, say r'. The reciprocity theorem leads to the conclusion that if we use these compensated fans as potential fans, the four-terminal

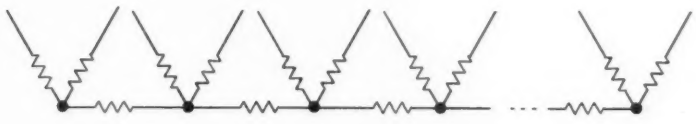

FIGURE 1

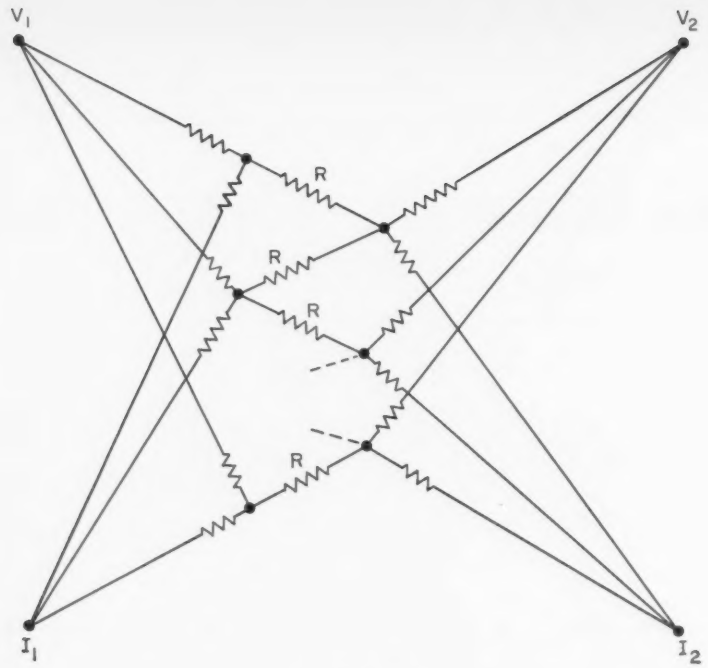

FIGURE 2

resistance would be R/n, independent of the current-fan resistances. Since the potential fans can tolerate larger resistance than can the current fans, the compensation is usually made in the potential fans; resistances of several tenths of an ohm can be added to the arms, allowing adjustment to reasonable accuracy.

Making either set of fans perfect yields zero error. This suggests that the overall error is in the nature of a product of fan errors, and suggests the possibility of reducing the effect of residual potential fan errors by making at least a rough adjustment of the current fan. For analysis, we consider four perfectly compensated fans as a nominal condition, with arbitrary maladjustments allowed in each arm. In addition each main resistor is allowed a departure from nominal.

The complete circuit to be analyzed is shown in figure 3, where the labels indicate *conductance* rather than resistance. Capital letters indicate "average" values, i.e.,

$$\sum a_i=\sum b_i=\sum c_i=\sum d_i=\sum g_i=0.$$

Considering terminal G as the "ground" terminal, we have a network possessing three external nodes, and $(n+1)$ internal nodes. A complete description of the network requires $3+(n+1)$ simultaneous equations, and we must eliminate the last $n+1$.

If we impress currents I_{I}, I_{II}, I_{III} into the external nodes, and I_1, I_2 . . . I_{n+1} into the internal nodes, the voltages on these nodes are implied by the simultaneous equations:

$$\begin{aligned}
I_{\text{I}} &= Y_{\text{I I}}V_{\text{I}}+Y_{\text{I II}}V_{\text{II}}+ \quad +Y_{\text{I}1}V_1+ \quad +Y_{\text{I}\,n+1}V_{n+1}\\
I_{\text{II}} &= Y_{\text{II I}}V_{\text{I}}+ \quad +Y_{\text{II}\,n+1}V_{n+1}\\
&\vdots\\
I_{n+1} &= Y_{n+1\,\text{I}}V_{\text{I}}+ \quad +Y_{n+1\,n+1}V_{n+1}
\end{aligned} \tag{1}$$

These equations are conveniently symbolized by the matric equation

$$I=YV \tag{2}$$

where I and V are column vectors (each having $n+4$ components), and Y is an $(n+4)\times(n+4)$ square matrix.

Consider I_{I}, I_{II}, and I_{III} as components of an "external" current vector, I_e, and I_1 . . . I_{n+1} as components of an "internal" current vector, I_i; similarly consider "external" and "internal" unknown voltage vectors, V_e and V_i. Grouping the terms appropriately:

$$\begin{aligned}
I_e &= \alpha V_e+\beta V_i\\
I_i &= \tilde{\beta} V_e+\gamma V_i
\end{aligned} \tag{3}$$

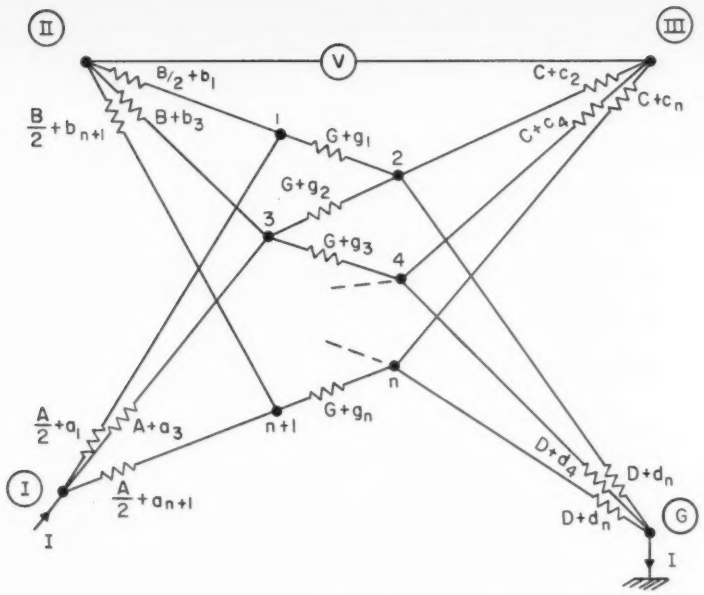

FIGURE 3

where α is a 3×3 matrix, β is a $3\times(n+1)$ matrix, $\tilde{\beta}$ is its transpose, and γ is an $(n+1)\times(n+1)$ matrix. In other words, the matrix is partitioned:

$$I=\begin{pmatrix}\alpha & \beta\\ \tilde{\beta} & \gamma\end{pmatrix}V. \tag{4}$$

Since we are interested in knowing the external voltage with *no* impressed internal current, we must eliminate V_i from

$$\begin{aligned} I_e&=\alpha V_e+\beta V_i\\ 0&=\tilde{\beta}V_e+\gamma V_i \end{aligned} \tag{5}$$

finding

$$\begin{aligned} I_e&=(\alpha-\beta\gamma^{-1}\tilde{\beta})V_e\\ V_e&=(\alpha-\beta\gamma^{-1}\tilde{\beta})^{-1}I_e. \end{aligned} \tag{6}$$

This last equation can be written as

$$\begin{pmatrix}V_{\mathrm{I}}\\ V_{\mathrm{II}}\\ V_{\mathrm{III}}\end{pmatrix}=\begin{pmatrix}z_{11} & z_{12} & z_{13}\\ z_{21} & z_{22} & z_{23}\\ z_{31} & z_{32} & z_{33}\end{pmatrix}\begin{pmatrix}I_{\mathrm{I}}\\ I_{\mathrm{II}}\\ I_{\mathrm{III}}\end{pmatrix}. \tag{7}$$

The required four-terminal resistance is the transfer resistance $(V_{\mathrm{II}}-V_{\mathrm{III}})/I_{\mathrm{I}}$ under the condition $I_{\mathrm{II}}=I_{\mathrm{III}}=0$, hence

$$R=(z_{21}-z_{31})\equiv(0,\,1,-1)z\begin{pmatrix}1\\0\\0\end{pmatrix}. \tag{8}$$

The problem is to carry out all the indicated algebraic manipulations, with all resistors subject to arbitrary tolerances. This will be done in an appendix, using the following strategy.

First, we carry out the manipulations required for $(\alpha-\beta\gamma^{-1}\tilde{\beta})^{-1}$ assuming the nominal values of the network elements; then, assuming that the departures from nominal are small, find the resulting correction to the nominal $R_0\left(=\dfrac{1}{nG}\right)$ as a series in powers of the perturbations. This yields a formula for the fractional error as a sum of terms of the type g_ig_j; g_ia_i, g_ib_i, etc.; a_ib_i, c_id_i. The terms involving the g_i (tolerances in the resistors of the series-parallel set) are ordinarily negligible compared with the pure measurement-network errors. These latter give (from eq (A38)):

$$\begin{aligned}\text{Error}=\frac{4}{n}\frac{G}{A+B}\Big(&2\frac{a_1}{A}\frac{b_1}{B}+\frac{a_3}{A}\frac{b_3}{B}\\ &+\frac{a_5}{A}\frac{b_5}{B}+\cdots+2\frac{a_{n+1}}{A}\frac{b_{n+1}}{B}\Big)\\ +\frac{4}{n}\frac{G}{C+D}\Big(&\frac{c_2}{C}\frac{d_2}{D}+\frac{c_4}{C}\frac{d_4}{D}+\cdots+\frac{c_n}{C}\frac{d_n}{D}\Big).\end{aligned} \tag{9}$$

Since $\Sigma a_i=0$, etc., this error arises from accidental correlation between errors of fan connections to common points. The worst case is where half the a_i have maximum positive error, the other half having maximum negative error—and where these pair up with the same situation among the b_i. Normal design would have $D=A$, $B=C$, and $A>>B$. Now let the maximum fractional error in the voltage fans be ϵ_v; in the current fans, ϵ_i. The resulting extreme error is $4\frac{G}{A}\epsilon_v\epsilon_i$. Reasonable estimates are $\frac{1}{G}=10\ \Omega$, $\frac{1}{A}=1\ \text{m}\Omega$, $\epsilon_i=10^{-1}$, $\epsilon_v=10^{-3}$, yielding a maximum error in the series-parallel ratio of 4×10^{-8}. Fractional errors of 10^{-5} in the main resistors make the g_i contributions completely negligible.

The above computation is for *maximum* error. Random pairing of the fan errors gives a much smaller expected error.

The next problem is to adjust the device after it has been constructed, and to evaluate the residual error. We note that if the current fans are perfect, there will be no voltage across any arm of the potential fans, hence any voltage across an arm of a potential fan is a measure of current-fan errors.

The potential fans have relatively high resistance, so are conveniently "trimmed" on a resistance bridge. To adjust the current fans, we can connect a microvoltmeter across each potential fan resistor in turn. This essentially measures the deviation of the potentials on the internal nodes, from their average. The current-fan arms can be filed to reduce these voltages to approximately zero.

In the analysis, we have treated the tetrahedral junctions as though their centers were available terminals. Any adjustment procedure must take cognizance of the fact that these terminals are fictitious; any physical connection is separated from the tetrahedron center by a low resistance. This could cause errors in direct measurement of current-fan resistance. The proposed scheme of measuring potential-fan resistances and voltage drops avoids this difficulty, since the potential fans are loaded with additional resistance.

In appendix A, we evaluate these residual adjustment errors quantitatively. We find to first order that the voltage across the arm $B+b_3$ is given by

$$IX_3=\frac{2}{n(A+B)}\frac{a_3}{A}I \tag{10}$$

and similarly the voltage across $A+a_3$, for current I into terminal (II) and out of terminal (III), is

$$IW_3=\frac{2}{n(A+B)}\frac{b_3}{B}I. \tag{11}$$

Comparison with eq (9) yields

$$\text{Error}=nG\Big\{(A+B)\left(\frac{X_1W_1}{4}+X_3W_3+X_5W_5+\ldots+\frac{X_{n+1}W_{n+1}}{4}\right)+(C+D)(X_2W_2+X_4W_4+\ldots+X_nW_n)\Big\}. \tag{12}$$

For a test current of 1 A, the fan tolerances assumed before yield voltages of the order

$$IX\sim2\times10^{-5}\text{V}$$
$$IW\sim2\times10^{-7}\text{V}$$

with

$$nGA\sim10^3.$$

Note that the larger voltage is generated by the current-fan error (under the assumed construction tolerances); this should make it feasible to adjust the current fan to the next order of magnitude.

The most sensitive set of measurements for evaluating the residual error is probably the set of residual adjustment errors; i.e., the residual potential-fan resistance differences and voltage drops. The appropriate formula is (from eq (A34)):

$$\text{Residual error}=2G\{X_1b_1/B+X_3b_3/B\ldots+X_{n+1}b_{n+1}/B-X_2c_2/C-X_4c_4/C-\ldots-X_nc_n/C\} \tag{13}$$

where positive X_i is associated with node i positive with respect to the appropriate potential terminal.

Note that the *measured* error quantities are first-order effects in the network tolerances; the computed residual error is a second-order product of these terms, so can be reasonably accurately evaluated by this procedure.

There are, of course, additional errors not attributable to the current and potential fans. The first of these arises from the fact that the *series* resistance is not n/G, but is

$$R_s=\Sigma\frac{1}{G+g_i}\doteq\frac{n}{G}\left(1+\frac{1}{n}\Sigma g_i^2/G^2\right)$$

yielding a fractional error of only 10^{-10} for $g_i/G\sim10^{-5}$. Another source of error lies in the imperfections of the tetrahedral junctions. Under conditions of suitable design and proper adjustment procedure, these junctions can be balanced to transfer resistances of less than $10^{-8}\ \Omega$. In a string of 10-Ω resistors, this is then a potential source of error of the order of 10^{-9}.

It seems feasible, therefore, to construct a 1:100 Ω buildup device with a ratio uncertainty of less than 1 in 10^8.

Appendix A

The submatrices of equation (4) are

$$\alpha=\begin{bmatrix} \frac{A}{2}+a_1+A+a_3+\ldots & 0 & 0 \\ 0 & \frac{B}{2}+b_1+B+b_3+\ldots & 0 \\ 0 & 0 & C+c_2+C+c_4+\ldots \end{bmatrix}$$

$$=\begin{bmatrix} \frac{nA}{2} & 0 & 0 \\ 0 & \frac{nB}{2} & 0 \\ 0 & 0 & \frac{nC}{2} \end{bmatrix}=\frac{n}{2}\begin{bmatrix} A & 0 & 0 \\ 0 & B & 0 \\ 0 & 0 & C \end{bmatrix} \tag{A1}$$

$$\beta=\begin{bmatrix} -\left(\frac{A}{2}+a_1\right) & 0 & -(A+a_3) & 0 & -(A+a_5)\ldots \\ -\left(\frac{B}{2}+b_1\right) & 0 & -(B+b_3) & 0 & -(B+b_5)\ldots \\ 0 & -(C+c_2) & 0 & -(C+c_4) & 0\ldots \end{bmatrix}. \tag{A2}$$

$$\gamma=\begin{bmatrix} G+g_1+\frac{A}{2}+a_1+\frac{B}{2}+b_1 & -(G+g_1) & 0\ldots \\ -(G+g_1) & 2G+g_1+g_2+C+c_2+D+d_2 & -(G+g_2)\ldots \\ 0 & -(G+g_2) & 2G+g_2+g_3+A+a_3+B+b_3\ldots \\ \vdots & \vdots & \vdots \end{bmatrix}. \tag{A3}$$

It is convenient to decompose these matrices into sums of nominal values and perturbations:

Let

$$\beta\equiv\beta_0+\beta_1$$

$$\gamma\equiv\Gamma+\gamma_0+\gamma_1+\gamma_2 \tag{A4}$$

where

$$\beta_0=\begin{bmatrix} -A/2 & 0 & -A & 0 & -A & \ldots \\ -B/2 & 0 & -B & 0 & -B & \ldots \\ 0 & -C & 0 & -C & 0 & \ldots \end{bmatrix} \tag{A5}$$

$$\beta_1=\begin{bmatrix} -a_1 & 0 & -a_3 & 0 & \ldots \\ -b_1 & 0 & -b_3 & 0 & \ldots \\ 0 & -c_2 & 0 & -c_4 & \ldots \end{bmatrix} \tag{A6}$$

$$\Gamma=\begin{bmatrix} \frac{A+B}{2} & 0 & 0 & \ldots & 0 \\ 0 & C+D & 0 & \ldots & 0 \\ 0 & 0 & A+B & \ldots & 0 \\ \cdot & & & & \cdot \\ \cdot & & & & \cdot \\ \cdot & & & & \cdot \\ 0 & \ldots & & & \frac{A+B}{2} \end{bmatrix} \tag{A7}$$

$$\gamma_0\equiv GS$$

$$S=\begin{bmatrix} 1 & -1 & 0 & 0 & \ldots & 0 \\ -1 & 2 & -1 & 0 & \ldots & 0 \\ 0 & -1 & 2 & -1 & \ldots & 0 \\ \cdot & & & & & \cdot \\ \cdot & & & & & \cdot \\ \cdot & & & & & \cdot \\ & & & & -1 & 2 & -1 \\ 0 & \ldots & & & -1 & 1 \end{bmatrix} \tag{A8}$$

$$\gamma_1=\begin{pmatrix} a_1+b_1 & 0 & 0 & \dots & 0 \\ 0 & c_2+d_2 & 0 & \dots & 0 \\ 0 & 0 & a_3+b_3 & \dots & 0 \\ \cdot & & & & \cdot \\ \cdot & & & & \cdot \\ \cdot & & & & \cdot \\ 0 & \dots & & & a_{n+1}+b_{n+1} \end{pmatrix} \tag{A9}$$

$$\gamma_2=\begin{pmatrix} g_1 & -g_1 & 0 & 0 & \dots & 0 \\ -g_1 & g_1+g_2 & -g_2 & 0 & \dots & 0 \\ 0 & -g_2 & g_2+g_3 & -g_3 & \dots & 0 \\ \cdot & & & & & \cdot \\ \cdot & & & & & \cdot \\ \cdot & & & & & \cdot \\ & & & & g_{n-1}+g_n & -g_n \\ 0 & \dots & & & -g_n & g_n \end{pmatrix} \tag{A10}$$

We write the admittance matrix as the sum of a nominal value and a perturbation:

$$Y=\begin{pmatrix} \alpha & \beta_0 \\ \tilde{\beta}_0 & \Gamma+\gamma_0 \end{pmatrix}+\begin{pmatrix} 0 & \beta_1 \\ \tilde{\beta} & \gamma_1+\gamma_2 \end{pmatrix}$$

$$\equiv Y_0\begin{pmatrix} 0 & \beta_1 \\ \tilde{\beta}_1 & \epsilon \end{pmatrix}. \tag{A11}$$

Let

$$Y_0^{-1}\equiv\begin{pmatrix} Z_0 & Z_1 \\ \tilde{Z}_1 & Z_2 \end{pmatrix} \tag{A12}$$

where

$$Z_0=(\alpha-\beta_0(\Gamma+\gamma_0)^{-1}\tilde{\beta}_0)^{-1} \tag{A12a}$$

$$Z_1=-Z_0\beta_0(\Gamma+\gamma_0)^{-1} \tag{A12b}$$

$$Z_2=(\Gamma+\gamma_0)^{-1}-(\Gamma+\gamma_0)^{-1}\tilde{\beta}_0 Z_1. \tag{A12c}$$

Now $(\Gamma+\gamma_0)^{-1}$ is not readily found, but the combination $\beta_0(\Gamma+\gamma_0)^{-1}$ is, from appendix B:

$$\beta_0(\Gamma+\gamma_0)^{-1}=-[1+2G(E+F)]^{-1}$$
$$\left\{2GEF\begin{pmatrix} A & A & A\dots \\ B & B & B\dots \\ C & C & C\dots \end{pmatrix}\right.$$
$$\left.+\begin{pmatrix} AE & 0 & AE & 0 & \dots \\ BE & 0 & BE & 0 & \dots \\ 0 & CF & 0 & CF & \dots \end{pmatrix}\right\} \tag{A13}$$

where

$$E\equiv\frac{1}{A+B},\ F\equiv\frac{1}{C+D}.$$

This yields

$$Z_0=\frac{1}{n}\begin{pmatrix} \frac{2}{A}+\frac{1}{G}+\frac{2}{D} & \frac{1}{G}+\frac{2}{D} & \frac{2}{D} \\ \frac{1}{G}+\frac{2}{D} & \frac{2}{B}+\frac{1}{G}+\frac{2}{D} & \frac{2}{D} \\ \frac{2}{D} & \frac{2}{D} & \frac{2}{C}+\frac{2}{D} \end{pmatrix} \tag{A14}$$

$$Z_1=\frac{1}{n}\begin{pmatrix} \frac{1}{G}+\frac{2}{D} & \frac{2}{D} & \frac{1}{G}+\frac{2}{D}\cdots \\ \frac{1}{G}+\frac{2}{D} & \frac{2}{D} & \frac{1}{G}+\frac{2}{D}\cdots \\ \frac{2}{D} & \frac{2}{D} & \frac{2}{D}\ \cdots \end{pmatrix}. \tag{A15}$$

These matrices are readily verified by inspection of the circuit when the elements have their nominal values.

The matrix Z_2 involves the term $(\Gamma+\gamma_0)^{-1}$ standing by itself; we shall eventually need this term and shall use a series expansion for it.

The four-terminal resistance of interest is the transfer resistance expressed as $V_{II}-V_{III}$ for $I_I=1$, all other input currents being zero:

$$R=[(0\quad 1-1)(0\quad 0\dots 0]Y^{-1}\begin{bmatrix}\begin{pmatrix}1\\0\\0\end{pmatrix}\\ \begin{pmatrix}0\\0\\\cdot\\\cdot\\\cdot\\0\end{pmatrix}\end{bmatrix}. \tag{A16}$$

In (A16), we have partitioned the vectors into "external" and "internal" vectors, corresponding to the partitioning of Y. For the nominal case we find

$$R_0=(0\quad 1-1)Z_0\begin{pmatrix}1\\0\\0\end{pmatrix}=\frac{1}{nG}. \tag{A17}$$

We are also interested in the transfer resistances that are measured as voltage drops across the potential-fan arms:

$$X_1=[(0-1\quad 0)(1\quad 0\quad 0\dots 0)]Y^{-1}\begin{bmatrix}\begin{pmatrix}1\\0\\0\end{pmatrix}\\ \begin{pmatrix}0\\\cdot\\\cdot\\\cdot\\0\end{pmatrix}\end{bmatrix}$$

$$X_2=[(0\quad 0-1)(0\quad 1\quad 0\ldots 0)]Y^{-1}\begin{bmatrix}\begin{pmatrix}1\\0\\0\end{pmatrix}\\ \begin{pmatrix}0\\\cdot\\\cdot\\\cdot\\0\end{pmatrix}\end{bmatrix}$$

$$X_3=[(0-1\quad 0)(0\quad 0\quad 1\quad 0\ldots 0)]Y^{-1}\begin{bmatrix}\begin{pmatrix}1\\0\\0\end{pmatrix}\\ \begin{pmatrix}0\\\cdot\\\cdot\\\cdot\\0\end{pmatrix}\end{bmatrix}.$$

$$\cdot$$
$$\cdot$$
$$\cdot \qquad \text{(A18)}$$

All $X_i=0$ for the nominal case.

The perturbation from nominal is found by expanding Y^{-1} in a series (as shown in appendix B for $(\Gamma+\gamma_0)^{-1}$):

$$Y^{-1}=Y_0^{-1}-Y_0^{-1}\begin{pmatrix}0 & \beta_1\\ \tilde{\beta}_1 & \epsilon\end{pmatrix}Y_0^{-1}$$

$$+Y_0^{-1}\begin{pmatrix}0 & \beta_1\\ \tilde{\beta}_1 & \epsilon\end{pmatrix}Y_0^{-1}\begin{pmatrix}0 & \beta_1\\ \tilde{\beta}_1 & \epsilon\end{pmatrix}Y_0^{-1}+\ldots \qquad \text{(A19)}$$

to second order in the perturbation.

The algebra will be alleviated by noting some special properties of the matrices β_1, γ_1, and γ_2:

$$(1\quad 0\quad 1\quad 0\ldots)\tilde{\beta}_1=(0\quad 0\quad 0)$$
$$(0\quad 1\quad 0\quad 1\ldots)\tilde{\beta}_1=(0\quad 0\quad 0) \qquad \text{(A20)}$$

since $\Sigma a_i=\Sigma b_i=\Sigma c_i=0$

$$\begin{aligned}
(1\quad 0\quad 1\quad 0\ldots)\gamma_1&=(a_1+b_1 \quad 0 \quad a_3+b_3 \quad 0 \quad \ldots)\\
(0\quad 1\quad 0\quad 1\ldots)\gamma_1&=(0 \quad c_2+d_2 \quad 0 \quad c_4+d_4 \quad \ldots)\\
(1\quad 0\quad 1\quad 0\ldots)\gamma_2&=(g_1 \quad -(g_1+g_2) \quad (g_2+g_3) \quad \ldots)\\
(0\quad 1\quad 0\quad 1\ldots)\gamma_2&=(-g_1 \quad (g_1+g_2) \quad -(g_2+g_3) \quad \ldots).
\end{aligned} \qquad \text{(A21)}$$

Note that premultiplication of either γ_1 or γ_2 by either $(1\quad 0\quad 1\quad 0\ldots)$ or $(0\quad 1\quad 0\quad 1\ldots)$, followed by postmultiplication by either

$$\begin{pmatrix}1\\0\\1\\0\\\cdot\\\cdot\end{pmatrix} \text{ or } \begin{pmatrix}0\\1\\0\\1\\\cdot\\\cdot\end{pmatrix} \text{ results in a null vector.}$$

Thus from (A12b) and (A13) in conjunction with (A20) and (A21), we have the very useful relations:

$$Z_1\tilde{\beta}_1=\mathbf{0}$$
$$Z_1\gamma_1\tilde{Z}_1=\mathbf{0}$$
$$Z_1\gamma_2\tilde{Z}_1=\mathbf{0}. \qquad \text{(A22)}$$

These simplify the multiplications required by eq (A19):

$$Y_0^{-1}\begin{pmatrix}0 & \beta_1\\ \tilde{\beta}_1 & \epsilon\end{pmatrix}=\begin{pmatrix}Z_0 & Z_1\\ \tilde{Z}_1 & Z_2\end{pmatrix}\begin{pmatrix}0 & \beta_1\\ \tilde{\beta}_1 & \epsilon\end{pmatrix}=\begin{pmatrix}0 & Z_0\beta_1+Z_1\epsilon\\ Z_2\tilde{\beta}_1 & \tilde{Z}_1\beta_1+Z_2\epsilon\end{pmatrix}$$

$$\equiv\begin{pmatrix}0 & M\\ Z_2\tilde{\beta}_1 & \tilde{Z}_1\beta_1+Z_2\epsilon\end{pmatrix}. \qquad \text{(A23)}$$

Note that

$$M\tilde{Z}_1=Z_0\beta_1\tilde{Z}_1+Z_1\epsilon\tilde{Z}_1=\mathbf{0}, \qquad Z_1\tilde{M}=\mathbf{0} \qquad \text{(A24)}$$

so that

$$Y_0^{-1}\begin{pmatrix}0 & \beta_1\\ \tilde{\beta}_1 & \epsilon\end{pmatrix}Y_0^{-1}=\begin{pmatrix}0 & MZ_2\\ Z_2\tilde{M} & Z_2\tilde{\beta}_1Z_1+\tilde{Z}_1\beta_1Z_2+Z_2\epsilon Z_2\end{pmatrix} \qquad \text{(A25)}$$

and finally

$$Y_0^{-1}\begin{pmatrix}0 & \beta_1\\ \tilde{\beta}_1 & \epsilon\end{pmatrix}Y_0^{-1}\begin{pmatrix}0 & \beta_1\\ \tilde{\beta}_1 & \epsilon\end{pmatrix}Y_0^{-1}$$

$$=\begin{pmatrix} MZ_2\tilde{M} & Mz_2(\tilde{\beta}_1 z_1+\epsilon z_2) \\ (z_2\epsilon+\tilde{z}_1\beta_1)z_2\tilde{M} & \text{etc.} \end{pmatrix}. \quad \text{(A26)}$$

Using these expressions in (A19) yields

$$R=\frac{1}{nG}+(0 \quad 1-1)MZ_2\tilde{M}\begin{pmatrix}1\\0\\0\end{pmatrix} \quad \text{(A27)}$$

with no first order correction.

The X_i have first order terms:

$$X_1=-(1 \quad 0 \quad 0\ldots)Z_2\tilde{M}\begin{pmatrix}1\\0\\0\end{pmatrix}$$

$$X_2=-(0 \quad 1 \quad 0\ldots)Z_2\tilde{M}\begin{pmatrix}1\\0\\0\end{pmatrix}$$

$$X_3=-(0 \quad 0 \quad 1 \quad 0\ldots)Z_2\tilde{M}\begin{pmatrix}1\\0\\0\end{pmatrix} \quad \text{(A28)}$$

etc.

These can be interpreted as the components of a vector, X:

$$X=-Z_2\tilde{M}\begin{pmatrix}1\\0\\0\end{pmatrix}. \quad \text{(A29)}$$

We can now write

$$R=\frac{1}{nG}-(0 \quad 1-1)MX \quad \text{(A30)}$$

as an alternate expression.

From (A12c) and (A24) we have

$$Z_2\tilde{M}=(\Gamma+\gamma_0)^{-1}\tilde{M} \quad \text{(A31)}$$

so that

$$R=\frac{1}{nG}+(0 \quad 1-1)M(\Gamma+\gamma_0)^{-1}\tilde{M}\begin{pmatrix}1\\0\\0\end{pmatrix}. \quad \text{(A32)}$$

Now

$$(0 \quad 1-1)M\equiv(0 \quad 1-1)Z_0\beta_1+(0 \quad 1-1)Z_1\epsilon$$

$$=\frac{1}{n}\left(\frac{1}{G},\frac{2}{B}+\frac{1}{G},-\frac{2}{C}\right)\beta_1$$

$$+\frac{1}{nG}(1 \quad 0 \quad 1 \quad 0\ldots)(\gamma_1+\gamma_2)$$

$$=\frac{1}{n}\left(\frac{g_1}{G}-\frac{2b_1}{B},-\frac{g_1+g_2}{G}+\frac{2c_2}{C},\right.$$

$$\left.\frac{g_2+g_3}{G}-\frac{2b_3}{B},\ldots\right). \quad \text{(A33)}$$

Neglecting g/G relative to b/B and c/C, we have

$$R\doteq\frac{1}{nG}+\frac{2}{n}\sum X_{2i+1}b_{2i+1}/B-\frac{2}{n}\sum X_{2i}c_{2i}/C \quad \text{(A34)}$$

for evaluation of error in terms of measured residuals.

To express R in terms of circuit element tolerances, we need to express X:

$$\tilde{X}=-(1 \quad 0 \quad 0)M(\Gamma+\gamma_0)^{-1}$$

$$=-(1 \quad 0 \quad 0)\{Z_0\beta_1+Z_1(\gamma_1+\gamma_2)\}(\Gamma+\gamma_0)^{-1}$$

which becomes

$$\tilde{X}=\frac{1}{n}\left(\frac{2a_1}{A}-\frac{g_1}{G},-\frac{2d_2}{D}+\frac{g_1+g_1}{G},\right.$$

$$\left.\frac{2a_3}{A}-\frac{g_2+g_3}{G},\ldots\right)(\Gamma+\gamma_0)^{-1}. \quad \text{(A35)}$$

We need $(\Gamma+\gamma_0)^{-1}$; we have

$$(\Gamma+\gamma_0)^{-1}\equiv(\Gamma+GS)^{-1}=\Gamma^{-1}-G\Gamma^{-1}S\Gamma^{-1}$$

$$+G^2\Gamma^{-1}S\Gamma^{-1}S\Gamma^{-1}-\ldots. \quad \text{(A36)}$$

Now

$$\Gamma^{-1}=\begin{pmatrix} 2E & 0 & 0 & \ldots & 0 \\ 0 & F & 0 & & . \\ 0 & 0 & E & & . \\ & & & & . \\ . & & & & \\ . & & & & \\ . & & & & \\ 0 & \ldots & & & 2E \end{pmatrix}$$

and the successive terms of (A36) diminish as powers of GE and GF, which are small compared to unity. Hence the first term of (A36) is sufficient for our purposes, for use in (A35):

$$X\doteq\frac{E}{n}\left(\frac{4a_1}{A}-\frac{2g_1}{G},0,\frac{2a_3}{A}-\frac{g_2+g_3}{G},0\ldots\right)$$

$$-\frac{F}{n}\left(0,\frac{2d_2}{D}-\frac{g_1+g_2}{G},0,\frac{2d_4}{D}-\frac{g_3+g_4}{G},0\ldots\right) \quad \text{(A37)}$$

and

$$R\doteq\frac{1}{nG}+\frac{E}{n^2}\left\{2\left(\frac{2a_1}{A}-\frac{g_1}{G}\right)\left(\frac{2b_1}{B}-\frac{g_1}{G}\right)\right.$$

$$\left.+\left(\frac{2a_3}{A}-\frac{g_2+g_3}{G}\right)\left(\frac{2b_3}{B}-\frac{g_2+g_3}{G}\right)+\ldots\right\}$$

$$+\frac{F}{n^2}\left\{\left(\frac{2c_2}{C}-\frac{g_1+g_2}{G}\right)\left(\frac{2d_2}{D}-\frac{g_1+g_2}{G}\right)\right.$$

$$\left.+\left(\frac{2c_4}{C}-\frac{g_3+g_4}{G}\right)\left(\frac{2d_4}{D}-\frac{g_3+g_4}{G}\right)+\ldots\right\}. \quad \text{(A38)}$$

Appendix B

A power series expansion yields

$$(\Gamma+\gamma_0)^{-1}\equiv(\Gamma+GS)^{-1}=\Gamma^{-1}(I+GS\Gamma^{-1})^{-1}$$
$$=\Gamma^{-1}(I-GS\Gamma^{-1}+G^2S\Gamma^{-1}S\Gamma^{-1}-\ldots)$$
$$=\Gamma^{-1}-G\Gamma^{-1}S\Gamma^{-1}+G^2\Gamma^{-1}S\Gamma^{-1}S\Gamma^{-1}-\ldots. \quad \text{(B1)}$$

The series converges if the norm of $S\Gamma^{-1}$ is less than $1/G$. A sufficient condition is

$$G<\min\left(\frac{\sqrt{2}}{4}(A+B),\frac{C+D}{2}\right). \quad \text{(B2)}$$

Premultiplication of the series by β_0 yields:

$$\beta_0(\Gamma+\gamma_0)^{-1}=\beta_0\Gamma^{-1}-G\beta_0\Gamma^{-1}(S\Gamma^{-1})$$
$$+G^2\beta_0\Gamma^{-1}(S\Gamma^{-1})^2-\ldots. \quad \text{(B3)}$$

For convenience, let

$$E\equiv\frac{1}{A+B},\ F\equiv\frac{1}{C+D} \quad \text{(B4)}$$

then

$$\Gamma^{-1}=\begin{pmatrix}2E & 0 & 0 & \ldots & 0\\ 0 & F & 0 & & \vdots\\ 0 & 0 & E & & \\ \vdots & & & & \\ 0 & \ldots & & & 2E\end{pmatrix} \quad \text{(B5)}$$

$$\beta_0\Gamma^{-1}=\begin{pmatrix}-AE & 0 & -AE & 0 & \ldots\\ -BE & 0 & -BE & 0 & \ldots\\ 0 & -CF & 0 & -CF & \ldots\end{pmatrix} \quad \text{(B6)}$$

$$S\Gamma^{-1}=\begin{pmatrix}2E & -F & 0 & 0 & \ldots & 0\\ -2E & 2F & -E & 0 & & \vdots\\ 0 & -F & 2E & -F & & \\ 0 & 0 & -E & 2F & & \\ \vdots & \vdots & & & & \\ 0 & \ldots & & & & 2E\end{pmatrix}. \quad \text{(B7)}$$

We compute

$$\beta_0\Gamma^{-1}(S\Gamma^{-1})=\begin{pmatrix}-2AE^2 & 2AEF & -2AE^2 & \ldots\\ -2BE^2 & 2BEF & -2BE^2 & \ldots\\ 2CEF & -2CF^2 & 2CEF & \ldots\end{pmatrix} \quad \text{(B8)}$$

and

$$\beta_0\Gamma^{-1}(S\Gamma^{-1})^2=\begin{pmatrix}-4AE^2(E+F) & 4AEF(E+F) & -4AE^2(E+F) & \ldots\\ -4BE^2(E+F) & 4BEF(E+F) & -4BE^2(E+F) & \ldots\\ 4CEF(E+F) & -4CF^2(E+F) & 4CEF(E+F) & \ldots\end{pmatrix}. \quad \text{(B9)}$$

Comparison of (B9) with (B8) shows that

$$\beta_0\Gamma^{-1}(S\Gamma^{-1})^2=2(E+F)\beta_0\Gamma^{-1}(S\Gamma^{-1}) \quad \text{(B10)}$$

so that

$$\beta_0\Gamma^{-1}(S\Gamma^{-1})^{k+1}=2^k(E+F)^k\beta_0\Gamma^{-1}S\Gamma^{-1} \quad \text{(B11)}$$

allowing (B3) to be evaluated as

$$\beta_0(\Gamma+\gamma_0)^{-1}=\beta_0\Gamma^{-1}-G\beta_0\Gamma^{-1}S\Gamma^{-1}$$
$$\{1-2G(E+F)+4G^2(E+F)^2-\ldots\}$$
$$=\beta_0\Gamma^{-1}-\frac{G}{1+2G(E+F)}\beta_0\Gamma^{-1}S\Gamma^{-1}. \quad \text{(B12)}$$

We note that the result (B12) is valid (by analytic continuation) without restriction on the size of G. Substituting (B6) and (B8) into (B12) yields

$$\beta_0(\Gamma+\gamma_0)^{-1}=-[1+2G(E+F)]^{-1}$$
$$\left\{2GEF\begin{pmatrix}A & A & A\ldots\\ B & B & B\ldots\\ C & C & C\ldots\end{pmatrix}\right.$$
$$\left.+\begin{pmatrix}AE & 0 & AE & 0 & \ldots\\ BE & 0 & BE & 0 & \ldots\\ 0 & CF & 0 & CF & \ldots\end{pmatrix}\right\}. \quad \text{(B13)}$$

(Paper 69C3-197)

JOURNAL OF RESEARCH of the National Bureau of Standards—C. Engineering and Instrumentation
Vol. 69C, No. 3, July–September 1965

Centerable Rotator for Measuring Properties of Crystals

Charles P. Saylor and Herbert B. Lowey

(February 23, 1965)

By allowing the unsupported portion of a spindle to be relatively long so as to extend from the rim of the microscope stage all the way to the axis, simple controls can be provided for centering a crystal with respect to a horizontal axis of rotation. In the device which is described, centration can be assured within about a micron. The angle of rotation with respect to a fixed position can be read with an error not greater than 0.05 degree.

1. Necessary Adjustments With the Single Axis Method

In the single axis of rotation method of measuring optical properties [1],[1] a crystal is held upon a spindle, it is rotated about an axis parallel to the stage of the microscope until one after another of the three characteristic vibration directions is made parallel to the stage, and each corresponding index of refraction of the crystal is then matched with that of an immersing liquid of known or subsequently determined refractivity. A crucial activity is the coordinated control of crystal orientation and polarizer vibration direction so as to achieve and recognize the three significant vibration directions. In this action, while the spindle is rotated slowly with one hand, the other hand, on the basis of information derived from changes in the interference figure, executes a controlled rotation of crossed polarizer and analyzer. The hand on the nicols sustains the condition by which an isogyre [2] will always cross the center of the interference figure.

Devices for rotating the spindles have been described by Wood and Ayliffe [2], Bernal and Carlyle [3], Wilcox [4], Hartshorne and Swift [5], Hartshorne [6], and others. Well planned as these rotators are for relatively large crystals, they imperfectly cover one condition, important with crystals which cover less than the full microscopical field. If the interference figure of a small crystal is to be sufficiently contrasty, its image must be isolated from other light which might pass to the observer. This is best accomplished with a field diaphragm placed above the Bertrand lens at the level where the image of the crystal itself is formed or, if a Klein magnifier is used, by a diaphragm in the image plane of the eyepiece. Under these conditions, if the crystal is uncentered with respect to the axis of rotation, it is necessary continuously to adjust the crystal vertically or horizontally as its image strays from the position of the field diaphragm. Both hands and the mind, however, are already occupied with the control of two rotations. While foot regulated motors might be installed, these would not overcome the problems that arise from division of attention. The effective solution is a rotator that permits centration of the crystal with respect to the axis of its rotation.

2. Design of a Centerable Rotator

In designing the apparatus which is described here, we found it expedient to depart from preceding practice to the extent of placing the entire rotator beyond the stage of the microscope. The actual support for the crystal, in the form of a small glass tube, thus extends unsupported across the radius of the stage. Because of the elasticity of glass and the smallness of the forces, this introduces no difficulty. Sensitive centering controls are easily achieved. In the device here described these operate at positions 90° from each other. The adjusting of one control does not upset the centering that has been achieved with the other.

The centerable rotator which we are now using is illustrated in figure 1. The stationary tube of the

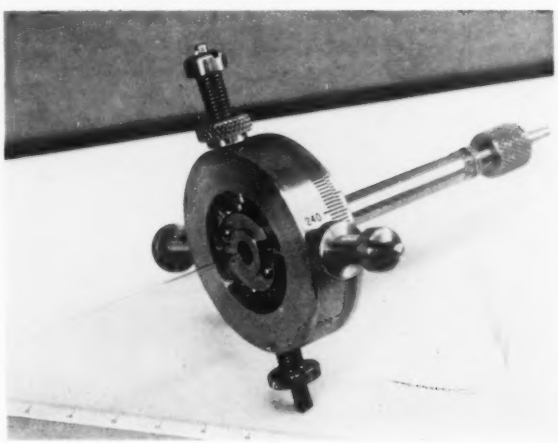

FIGURE 1. *The centerable rotator.*

The back and bottom nobs drive two jaws by reason of the difference between 28 and 32 thread screws. The others are spring loaded. The front and back jaws, cut away over half their diameters, lap over the top and bottom jaws.

[1] Figures in brackets indicate the literature references at the end of this paper.
[2] A locus of directions in a crystal (as seen in orthographic projection) for which the projected vibration directions, whether trivial or characteristic, are each parallel to the vibration directions of a polarizer or analyzer.

rotator, normally held in the chuck of a micromanipulator, is attached to an end plate with a 20-interval vernier extending across 38°. At the right end, a thumb screw compresses a 2 mm long annulus of "microchemical" rubber tubing, 1.5 mm in internal and 3.5 mm in external diameter. This serves as a flexible chuck to hold and center the end of the tube farthest from the crystal. The hollow shaft has an internal diameter of about 3 mm. Since the device was planned for use with 1.35 ± 0.15 mm glass tubing (a standard size), a total excursion of about 1½ mm at the controlled end is possible. The overhang of the tubing (the distance from the controlled end to the crystal) is not less than length of the rotator so that the range of adjustment at the crystal is about 3 mm. In the drum at the left are the controllers, those with jaws driven by differential screws at the back and bottom and those with jaws pushed by light springs at the front and top. The sets which are separated by 90° overlap like the parts of a lap joint.

Details of the centering controller are shown in figure 2. For movement of two jaws, a ¼-in.–28 machine screw is drilled along the center and tapped with a No. 8–32 thread. The actual jaws are cut into the central screws, one side of each of these being cut away for 11 mm. They thus glide in a channel outside the point where they overlap the other set. This keeps them from rotating. The other two jaws are spring loaded. The differential movement is such that the jaw advances a little more than 0.1 mm for each full turn of the larger screw. This corresponds to about 0.2 mm at the crystal, thus providing all necessary sensitivity. By comparison, one full turn of the fine adjustment of the standard microscope produces a movement of 0.1 mm.

In order to insert the glass tube into the rotator, it is convenient to have means of retracting both the screw driven and the spring loaded jaws. As we have chosen to manage this, the spring-loaded jaws are momentarily held back by a flat collar in the back of the jaws with two camlike wedges that can press the jaws outward.

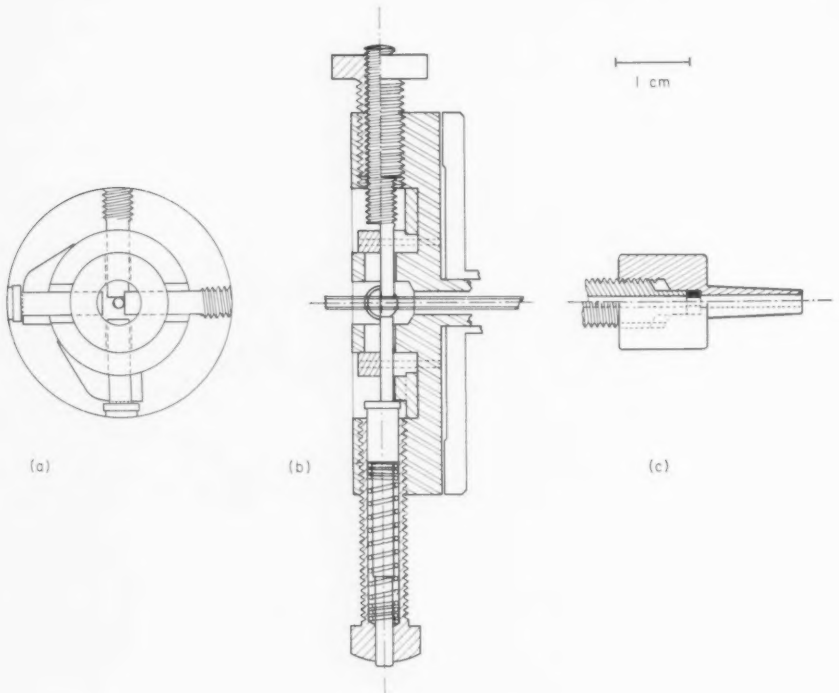

FIGURE 2. *Details of the rotator.*

(a) Overlap of centering jaws as seen from end. (b) Differential screw drive. (c) The clamp and aspirator.

The graduated drum provides an easy means for recording positions of the spindle. Since the drum is only 5 cm in diameter, markings at 1 deg intervals would be separated by less than 0.5 mm. This would be too close. When 2 deg marks are combined with the 20 interval vernier there is adequate accuracy. Thus the position of the drum as seen in figure 1 clearly lies between 213.5 and 213.6°, being closer to the former. Obviously the uncertainties are less than 0.05 deg. Since the accuracy of settings of the crystal is rarely better than 1 deg, this precision of measurement meets all requirements.

3. Supporting the Crystals

It is well to insert a word about the use that is made here of glass tubing for the spindle. Equipment is available for drawing tips on capillary glass tubing with practically perfect control. By having a sharply tapered end on such a tubular spindle, crystals can be held in either of two satisfactory ways. This can be by suction applied to the tubing by means of the nipple shown at the right, figure 1. Although some immersion fluid leaks between the crystal and the end of the tube, the steadily increasing diameter prevents viscosity losses from destroying the force at the attachment. Occasionally the leakage is so great that too much of the immersion compound will be lost.

The second technique, which is also limited to tubes, makes use of drying cements. If a tapered very fine rod is inserted into a cement and withdrawn, surface tension tends to remove the cement down to such thinness that the residue cannot provide adhesion. With a somewhat larger rod, the residual cement adheres to the sides, but not to the end. With a tapered tube, however, the outside is left nearly bare whereas the cement flowing into the canal forms a nearly plane surface across the end. When this plane end is touched to a crystal, the crystal is caught up by capillarity. As the cement dries in a circle of contact between the crystal and the tube, the attachment becomes very strong. Of the many different cements which can be used, one of the most satisfactory is ordinary corn syrup.

By either of these methods of attachment, a crystal will hold an unvarying position at the end of a tubular spindle. The attachment endures through the necessary reorientations of the crystal, changes in composition of the immersing fluid, and determinations of the refractive index of the fluid. Since the correctness of orientation of the crystals and their vibration directions can be found with adequate sensitivity, and since the accuracy of a refractive index measurement is limited only by the criterion of match and the patience of the observer, the rotator which is here described facilitates highly accurate determinations of the principal optical properties of crystals.

4. References

[1] C. P. Saylor, Chemical Society of Washington, Spring Meeting, May 11, 1944.
J. L. Rosenfeld, Am. Mineral. **35,** 902 (1950).
R. E. Wilcox, Am. Mineral. **44,** 1272 (1959).
[2] R. G. Wood and S. G. Ayliffe, J. Sci. Instr. **12,** 194 (1935).
[3] J. D. Bernal and C. H. Carlisle, J. Sci. Instr. **24,** 107 (1947).
[4] R. E. Wilcox, Am. Mineral. **44,** 1272 (1959).
[5] N. H. Hartshorne and P. M. Swift, J. Roy. Mic. Soc. **75,** 129 (1955).
[6] N. H. Hartshorne, Mineral. Mag. **33,** 693 (1963).

(Paper 69C3–198)

JOURNAL OF RESEARCH of the National Bureau of Standards—C. Engineering and Instrumentation
Vol. 69C, No. 3, July–September 1965

Equipment for Single-Crystal Growth From the Melt Suitable for Substances With a Low Melting Point

Avery T. Horton and Augustus R. Glasgow

(April 27, 1965)

Glass apparatus is described for the purification and growth of crystals with melting points up to about 130 °C by a modified Bridgman technique. The temperatures of the melt and the solid are maintained by two immiscible liquids at whose interface a sharp temperature drop exists. A sealed Pyrex tube containing the specimen is slowly lowered through the interface. The specimen is maintained under its own vapor pressure in contact only with the glass container. Provision is made for the removal of the last portions of the specimen to solidify from each of several successive recrystallizations.

The equipment has been found effective for the purification of *trans*-stilbene, dimethyl oxalate, benzoic acid, and benzene. It could also be used for careful studies of thermal and radiation stability of pure substances.

1. Introduction

The procedures for the growth of a single crystal from the melt commonly restrict growth to an isothermal growth surface held in a horizontal plane and perpendicular to the flow of heat from the melt [1].[1] The surface is not permitted to regress (remelt). In the Bridgman method the growth of a single crystal takes place at the boundary between two temperature zones, above and below the melting point of the substance. The temperature boundary is normally produced by arranging vertically two furnaces which are separated by a thin layer of heat-insulating material with an opening for passage of the container in which the material is held. Crystal growth proceeds by relative movement of container and furnaces.

Too often the temperature gradient at the boundary of the two zones is neither sharp nor well-defined. Convection currents of air in and between the zones cause nonuniform temperatures at the boundary and in the two zones. Consequently the uniform growth surface is not realized.

Following an observation on the remarkably low transfer of heat across the interface between two immiscible liquids, equipment [2] for the growth of single crystals from the melt has been developed to use the very sharp, uniform, easily controllable temperature gradient thus produced. This type of equipment is limited to temperature ranges in which liquids are thermally stable, do not react with containers, and in which liquid pairs remain immiscible. With each liquid heated independently at the wall of a container, thermal or mechanical stirring in each layer can be expected to maintain two uniform temperature zones above and below the melting point of the substance being crystallized. Good crystals are produced only when the lines of heat flow from the melt are substantially perpendicular to the growing crystal surface. This means that the growth process must be slow enough for most of the heat to be dissipated through the crystal rather than through the container walls near the interface. A convex solid surface is indicative of satisfactory heat flow and minimizes the effects of unwanted nucleation at the wall of the growth tube.

With all-glass construction, visibility is unimpaired to observe nucleation, "lone seed survival" in the early stages of growth, and the entire growth process. A specially designed growth tube provides for the introduction of material by distillation or sublimation in a vacuum, subsequent sealing, and the growth of single-crystal material in the presence of its own vapor only. Appended seal-off bulbs allow the isolation and removal of the last portion of melt (or the last portion of crystal to grow) in which impurities have been concentrated by continuous rejection into the molten phase at the crystal-melt interface.

2. Apparatus

2.1. Growth Tube

The growth tube, shown in figure 1, is used as follows: The material to be crystallized is introduced at A by vacuum distillation or sublimation, with subsequent sealing at S_1. The tube is attached by eyelets C and E to cables that control its movement through the immiscible liquid bath by means of a synchronous motor. Crystallization is initiated in the tip of the capillary portion D and allowed to progress through the length of the capillary with the object of promoting the selection of a single oriented crystal at its juncture with the main body

[1] Figures in brackets indicate the literature references at the end of this paper.

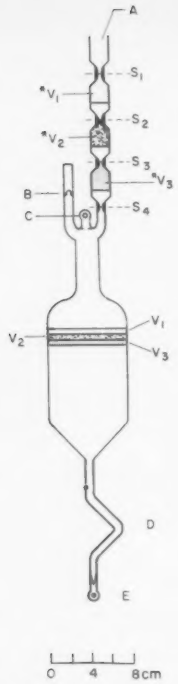

FIGURE 1. *Growth tube.*

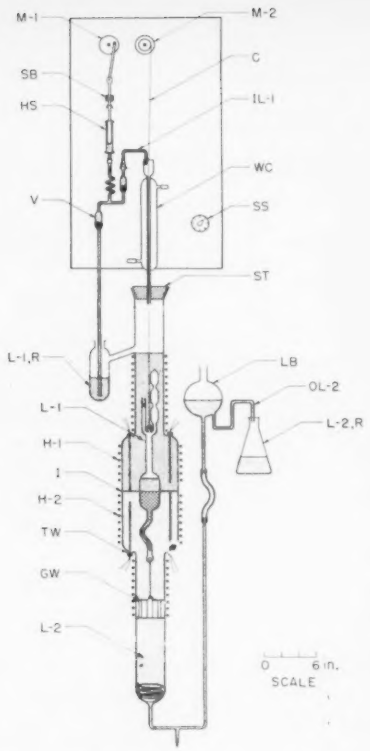

FIGURE 2. *Complete crystal-growth apparatus.*

of the tube; crystallization in the body of the tube progresses in the form of one or, at most, a few crystals as the tube passes continuously through the interface between the two liquids. The last (impure) portions V_1, V_2, V_3 of the crystal to form at each successive pass are remelted and transferred into the attached bulbs ($*V_1$, $*V_2$, $*V_3$) by inverting the entire growth tube and sealing off at S_2, S_3, or S_4. The purified material is transferred to evacuated containers through the break-tip at B. Typically the growth tube contains about 500 cm^3 of liquid substance, the attached bulbs $*V_1$ etc., have a volume of 10 cm^3 each. Growth tubes of a variety of sizes, but similarly proportioned, have been used. Various shapes of the capillary portion D have been tried with varying success for different substances.

2.2. Dithermal Jacket

Suitable immiscible liquid systems which have been studied include paraffinic oil (Marcol)-ethylene glycol, silicone oil-ethylene glycol, toluene-water, and water-carbon tetrachloride. Good boundary conditions were obtained between the two zones in all cases, provided that the temperature of the liquid in the lower layer was 20 to 30 °C below its boiling point. Silicone oil (Dow-Corning 500) and ethylene glycol had the widest range. After about 6 months as bath liquids at approximately 150 and 100 °C, respectively, the silicone oil remained colorless, but the ethylene glycol tended to become cloudy and was generally replaced.

A diagram of the complete apparatus is shown in figure 2. The immiscible liquids, L–1 and L–2, are heated in the glass column by resistance-wire heaters H–1 and H–2. Thermocouples for measuring temperatures near the interface, I, are connected to a selector switch SS. They are located in six re-entrant wells, TW, placed 0, 1, and 2 cm above and below the interface. Typical temperatures in the dithermal jacket, observed at these six positions during the growth of *trans*-stilbene, were in order of decreasing height 157.3, 155.5, 143.7, 112.7, 100.1, and 99.2°, respectively. Hence, the temperature difference across the interface was 31 °C. The growth tube and weight, GW, are centered and lowered in the column by the cable, C, from a drum which is driven by the hour shaft of a synchronous clock motor, M–2, which in turn is controlled by a current interrupter. Speeds down to ½ cm per day have been used. About 2 weeks are required to complete one crystallization cycle. The growth tube is placed in or removed from the column by detaching the inlet tube, IL–1, and the water condenser, WC, at the stopper, ST.

During crystal growth the upper liquid was generally held 25 °C above and the lower liquid 25 °C below the melting point of the sample. It is suspected that experimentation with smaller temperature differences will prove interesting; the lower thermodynamic driving force and the reduced thermal shock may tend to lead to the production of more perfect crystals.

Since the descending growth tube displaces first one, then the other, of the two immiscible liquids, provision is made to maintain the interface in fixed position. The decrease in volume in the upper liquid chamber is compensated by the addition of fresh liquid from the reservoir, L–1, R, through the pump, HS, and inlet tube IL–1; excess liquid overflows back to the reservoir. The pump is made from a hypodermic syringe, HS, and glass check valves, V, and is driven by a reciprocating device, M–1. The bearing, SB, serves to keep the piston rod centered. Liquid displaced from the lower layer by the descending tube overflows from the leveling bulb, LB, at OL–2 and collects in the flask, L–2, R, from which the bulb LB can be manually replenished at the end of a run.

3. Notes on Experimental Procedures

In experiments in which the aim is to preserve the single crystal intact, the entire sample is permitted to crystallize and the assembly is brought slowly to room temperature. Most crystals have a higher coefficient of expansion than glass and will therefore pull away from the container walls. The growth tube is parted by scoring with a glass cutter, and the crystal is removed intact.

In experiments in which the aim is to acheive a high degree of purification, crystallization can be stopped before the last, most impure portion has solidified. The crystallizer is quickly withdrawn from the bath, inverted, and the liquid collected in one of the small bulbs V (fig. 1) which, after solidification by cooling, is sealed off and rejected. The sample is not allowed to cool to room temperature whenever another crystallization cycle is planned. Otherwise on reheating there is danger of cracking the glass container. If reheating is necessary after cooling, the best procedure is to heat the glass rapidly to permit melting of the surface regions of the solid. The liquid so formed will yield during subsequent expansion of the remaining sample.

Another procedure which has been employed is to allow the entire sample to crystallize. The tube is now removed and the temperatures of the two immiscible liquids are reversed, the upper liquid is lowered to about 25° C below the melting point of the crystal, and the lower liquid is raised to about 25 °C above the melting point of the sample. The growth tube is now reinserted in an inverted position and the guide weight and support cable attached to opposite eyelets. The crystal is placed in the upper bath, allowed to come to temperature, then lowered to a position in the interface determined by the amount of material to be rejected. This portion is melted and drained into one of the bulbs V (fig. 1), and the tube and contents are removed from the column. The liquid in V_1 is frozen, cooled to low temperature, and the bulb is sealed off at S_2.

The growth cycle is repeated until purity assays of small portions last to crystallize are of a satisfactory level of purity. The purified substance may then be transferred to other vessels through the break-tip, B.

For a given sample some indication of the impurity is obtained by observing the growth process, particularly the shape of the solid-liquid interface. When the contamination is considerable the solid tends to be polycrystalline especially in a typically conical core at the top of the solidified portion. Several crystallization cycles lead to better single-crystal growth. In the final growth of a very-high-purity sample, the solid-liquid interface tends to have a convex shape.

4. Substances Purified by Single-Crystal Growth

4.1. *trans*-Stilbene

Commercial *trans*-stilbene (scintillation-grade, about 99.9 mole percent, mp 124 °C) was melted, filtered, vacuum-sublimed twice, and a 200 cm^3 portion transferred to the growth tube. The tube was lowered through the interface between upper and lower bath liquids at 155 and 100 °C, respectively. Four passes, with removal of 5 cm^3 last portions after the first and second pass, were required to produce a single crystal which was optically clear.

The contour of the crystal surface changed as impurities were removed in successive recrystallizations. The first pass resulted in a shallow V-shaped surface containing colored material which remained liquid in the bath at 100 °C and was shown to have a melting point 24° below that of *trans*-stilbene. A marked improvement in the surface was noted during the second cycle. The third growth produced a specimen which was still not optically clear, but the fourth run resulted in a clear single crystal. An analysis of the purity of the final product was not made.

4.2. Dimethyl Oxalate

Commercial dimethyl oxalate (93.7 mole percent) was purified by two vacuum sublimations to a purity of 99.6 mole percent measured cryoscopically [3]. During sublimation methyl alcohol was removed in a volatile fraction, while methyl hydrogen oxalate and oxalic acid remained in the residue.

Two samples of the sublimed dimethyl oxalate (mp 54 °C) were grown as single crystals by lowering the growth tube through the interface between an upper liquid at 80 °C and a lower liquid at 30 °C. The first sample (about 250 cm^3), crystallized twice with one intermittent removal of a small last portion, gave a single crystal which was perfectly clear. The second sample (about 400 cm^3) was crystallized three times

773–721—65——3

with two impure last portions removed. The final surface to crystallize was flat and the crystal was clear. An analysis of the purity of the final product was not made.

4.3. Benzoic Acid

The starting material was benzoic acid of purity 99.997 mole percent (mp 122.37 °C) as determined by comparison with a thermometric cell of benzoic acid of known purity. The sample was degassed in a vacuum to remove water vapor and air, then vacuum distilled into the growth tube at 150 °C. The tube was lowered through the interface between liquids at 150 and 100 °C, 15 cm^3 of the last portion to crystallize was removed, and the crystal was melted and regrown. The final specimen was not a single crystal; half of the material appeared to be a single crystal, while the other portion appeared to contain two crystals.

The specimen was taken from the tube and cut with a jeweler's saw to isolate the single-crystal portion. All imperfect portions were removed by cleaving. The specimen was sealed in a platinum envelope, gold-soldered to prevent contamination, and was used as an acidimetric standard of high purity in comparison studies by Bates and Wichers [4].

In the latter study an intercomparison by precise differential titrimetry corroborated the above purity of the starting material (determined independently by calorimetric analysis), and showed the single crystal benzoic acid and single crystal potassium acid phthalate (grown from aqueous solution) to be not less than 99.9998 mole percent pure.

4.4. Benzene

Benzene (fp 5.5 °C, purity 99.8±0.2 percent) was purified by single crystal growth from the melt with the upper liquid at room temperature, the lower liquid cooled to about −28 °C by immersion of the lower half of the column in a circulating bath of refrigerant. The purified benzene, used in comparative tests of methods for the determination of purity [5], contained impurity believed to be less than could be disclosed by thermal analysis ($<10^{-4}$ mole percent). Actual cryometric and calorimetric assays showed a purity of 99.995 mole percent, but contamination by water adsorbed on the inner surfaces of the measuring apparatus was believed to have contributed to this value.

5. Further Potential Applications

The immiscible liquid-pair system may operate at much higher temperatures than have been employed in the present work. Thermal stability and immiscibility of liquids are major requirements. Molten salts, metals, and metal alloys could conceivably be used, although alterations in heating methods, insulation, vessel and column construction, etc., would be involved. Such developments have not been pursued, since present programs have dealt with substances melting below 200 °C.

The usefulness of the equipment here described could be extended to the study of stability of pure substances under controlled conditions of, say, temperature or radiation. The purified sample while sealed in the tube could be subjected to the relevant experimental conditions and the decomposition products could be concentrated and isolated in a subsequent recrystallization cycle.

The authors thank C. P. Saylor for his initiation of and interest in this project. The type of pump used (HS fig. 2) was the idea of G. Ross. The benzoic acid starting material was prepared by D. Enagonio.

6. References

[1] J. J. Gilman, The Art and Science of Growing Crystals (John Wiley & Sons, Inc., New York, N.Y., 1963).
[2] A. T. Horton, U.S. Patent No. 2,754,180 (July 10, 1956).
[3] A. R. Glasgow and M. Tenenbaum, Anal. Chem. **28,** 1907 (1956).
[4] R. G. Bates and E. Wichers, J. Res. NBS **59,** 9 (1957) RP2769.
[5] A. R. Glasgow, G. S. Ross, A. T. Horton, D. Enagonio, H. D. Dixon, C. P. Saylor, G. T. Furukawa, M. I. Reilly and J. M. Henning, Anal. Chim. Acta. **17,** 54 (1957).

(Paper 69C3–199)

JOURNAL OF RESEARCH of the National Bureau of Standards—C. Engineering and Instrumentation
Vol. 69C, No. 3, July–September 1965

Phase and Amplitude Contrast Microscopy in Partially Coherent Light

M. De and P. K. Mondal

Department of Applied Physics, University College of Technology, 92 Acharya Prafulla Chandra Road, Calcutta 9, India

(March 10, 1965)

This paper describes the effects obtained in phase contrast imagery with partially coherent illumination of phase objects. The objects chosen for study include simple Zernike type of periodic phase gratings of the form (i) $A(u)=1+i\cdot\Delta\cdot\cos\omega u$ and (ii) $A(u)=1+i\cdot\sum_{n=1}^{\infty}\Delta_n\cdot\cos n\omega u$, with axial or oblique partially coherent illumination. The concept of "effective source" has been utilized, and the nonlinearity in the intensity transmission due to partial coherence has been analyzed in terms of "fundamental contrast" and "remnant."

1. Introduction

It is known that ordinary methods of observation are not suitable for obtaining information about phase objects. Special techniques have to be used to render phase variations visible, namely, the dark-ground method of observation in which the direct beam illuminating the object is stopped. There is the other method, the Schlieren method, which differs from the above in that not only the direct light but also a part of the diffracted beam is also stopped from entering the ultimate detector. However, the most powerful method in this respect is due to Zernike [1934, 1942] which makes use of a phase modulation of the central or zero order of the diffraction produced by the object. In fact, it was shown by Zernike that with this method, which he termed as "phase-contrast" method, phase variations in the object are practically linearly transformed into changes in intensity and thus made observable. Later, Hopkins [1952] pointed out that because of the finite size of the aperture, some details of phase structures could be seen in ordinary microscopes as well.

The Zernike theory of the phase contrast method basically makes use of the Abbé theory of microscopic imagery in coherent light. We shall then refer to this as the Abbé-Zernike theory. A simple and obvious extension may be made to the theory to include the effect of amplitude modulation of the diffraction spectra, thus including the dark-ground and Schlieren methods of observation as well. In the original elementary theory of Zernike there were certain implicit assumptions which were later treated by Picht [1936] and Kahn [1955]. Osterberg [1944] has also made a thorough study of the phase-contrast method as a problem in diffraction, in which he showed that the phase-plate characteristics could simply be treated as a "coating function" modifying the pupil function of the microscope objective. His basic diffraction integral, which he terms as "generalized transport integral" includes the effect of not fully coherent illumination, though in the final analysis he restricts himself to a narrow cone, or effectively coherent illumination of the object.

In the meantime, the concept of partial coherence has been utilized by Hopkins [1953] in formulating what he describes as the generalized Abbé theory, the generalization being due to his inclusion of the effect of partially coherent illumination of the object. Steel [1958] also gave a generalized treatment of image formation in partially coherent light. We followed up the obvious next step in generalizing the Abbé-Zernike theory of "phase and amplitude contrast microscopy in partially coherent light." As a first step in this direction De and Som [1963] extended the study of Hopkins [1952] to show that phase structures could be observed in ordinary microscopes even in partially coherent light, the extent of observation depending on the magnitude of phase variations and the degree of partial coherence.

In this paper, we now discuss the effect of phase and amplitude contrast technique on the images of simple Zernike-type objects represented by $A(u)=1+i\ \Delta(u)$, in which the magnitude of Δ is small enough to justify the presumption that the object shows no variable intensity transmission. In our treatment, we have utilized the theorem of effective source as postulated by Hopkins [1953, 1957], and the observation of Osterberg that the phase and amplitude contrast plate characteristics may be simply associated with the pupil function of the objective. This treatment may be further extended to cover a general type of phase grating represented by $A(u)=\exp\ [i\ \Delta(u)]$, of which the Zernike-type object is just a special case. We may further assert that our method is perfectly amenable to the consideration of even nonperiodic objects in a rather straightforward manner, and also of the effects of small residual aberrations in the objectives. Slansky [1962] also studied a similar problem, though his treatment is restricted to the case of Zernike-type objects only.

2. General Solution

In deriving the general solution of the problems of diffraction in phase and amplitude contrast microscopy in partially coherent light, we shall make use of the formulation by Hopkins [1953]. In his so-called generalized Abbé theory in partially coherent light, Hopkins showed that, in all practical cases, the illumination of the object may be considered as due to a self-luminous source placed at the condenser exit pupil. This is termed the "effective source," and insofar as the degree of partial coherence on the object plane is concerned, there seems to be no difference of practical significance between the two types of illuminating systems—viz, the Kohler and the critical illumination. This and the further consideration of the progress of mutual intensity between a pair of points through the object to the objective aperture shows that this "effective source" may be orthoscopically projected on to the objective aperture through the object point.

Earlier Osterberg and Wilkins [1949] showed that with objectives satisfying Abbé's sine condition, the diffraction plate characteristics may be simply treated as modifying the pupil function of the objective. Thus, the overall pupil function of the phase- and amplitude-contrast objective may be taken as

$$\bar{f}(x, y)=f(x, y)p(x, y)$$

where $p(x, y)$ is the complex amplitude transmission of the diffraction plate. That this is possible is seen from the fact that (x, y) denotes not only the coordinates of the point on the pupil but also the angles a ray makes with the axis as it comes from the object point on the axis to the point on the pupil. Thus, this also refers to a corresponding point on the back focal plane on which the diffraction plate is situated.

Based on these two premises, the final intensity distribution in the image plane is given by

$$B'(u', v')=\iint \gamma(x_0, y_0)|\phi(x_0, y_0; u', v')|^2 dx_0 dy_0 \tag{1}$$

where

$$u'=\frac{2\pi}{\lambda}\cdot n'\cdot \sin\alpha'\cdot \xi',$$

$$v'=\frac{2\pi}{\lambda}\cdot n'\cdot \sin\alpha'\cdot \eta',$$

$$x_0=\frac{a_0}{h},\ y_0=\frac{b_0}{h},$$

and where

$u'\ v'$—reduced coordinates of a point on the image plane,
$\xi',\ \eta'$—coordinates of a point on the image plane,

x_0, y_0—fractional coordinates of a point on the pupil,
$\sin \alpha'$—semiangular aperture of the objective referred to the object point,
a_0, b_0—coordinates of a point on the pupil or on the effective source,
h—radius of the pupil,
n'—refractive index of the medium between the object and the objective,
$\gamma(x_0, y_0)$—is the effective source function described in terms of the pupil coordinates,
$|\phi(x_0, y_0; u', v')|^2$—partial intensity at the point (u', v') of the image plane due to an element $dx_0 dy_0$ of the effective source.

The physical significance of the above integral is obvious. To obtain the partial intensity, $|\phi|^2$, we may proceed as follows:

Let $A(u, v)$ = complex amplitude transmission of the object, which may be Fourier analyzed into

$$a(x, y) = \iint_{-\infty}^{+\infty} A(u, v) e^{-i(ux+vy)} du dv \tag{2}$$

giving the components of the spectrum of $A(u, v)$.

If we consider the object to be illuminated by an element $dx_0 dy_0$ of the effective source at x_0, y_0, the spectrum would be shifted by a corresponding amount. Thus, the amplitude distribution of the spectrum would be given by $a(x-x_0, y-y_0)$, which, after passing through the objective and the diffraction plate, will be modified to $a(x-x_0, y-y_0)\bar{f}(x, y)$. The partial intensity, then, is given by the squared modulus of the inverse transform of the above. In other words,

$$\phi(x_0, y_0; u', v') = \iint a(x-x_0, y-y_0)\, \bar{f}\,(x, y) e^{i(u'x+v'y)} dx dy \tag{3}$$

gives the complex amplitude distribution in the image plane due to an element of the source at x_0, y_0. It may also be interpreted as the complex amplitude distribution in the image plane when the object is illuminated by a plane wave front proceeding in the direction making an angle x_0, y_0 with the axis.

It now remains to evaluate explicitly the function ϕ pertaining to a specific object, which is possible if the composite pupil function is known.

3. Solutions of Cases of Periodic Grating Objects of the Zernike Type

We are now in a position to obtain solutions of specific cases. First, we shall consider those types of diffraction (or Zernike) plates which have a phase and amplitude contrast coating over an area which has the same relative size as the effective source. The complex amplitude transmission of this area, which we shall call the "conjugate area," is, say, given by $he^{i\psi}$, while that of the remaining area, the so-called "complementary area," is unity. h in the above implies amplitude contrast and ψ, phase contrast.

Let us first consider the simple Zernike-type object:

$$A(u) = 1 + i \cdot \Delta(u) \tag{4}$$

in which Δ is so small that Δ^2 is neglected. In other words, the intensity transmission of the above object is constant while the phase varies as $\Delta(u)$. Assuming $\Delta(u)$ to be periodic, we have

$$\Delta(u) = \sum \Delta_n \cdot \exp[-in\omega u] \tag{5}$$

where

$$\Delta_n = \frac{1}{2u_0} \int_{-u_0}^{+u_0} \Delta(u) \exp[in\omega u] du$$

$2u_0$ is the length of the fundamental period. $\omega = (\pi/u_0)$.

The Fourier-spectrum of the object function (4) is thus given by

$$a(x, y)=\delta(x, y)+i\sum_{-\infty}^{+\infty}\Delta_n\cdot\delta(x+n\omega, y) \tag{6}$$

where $\delta(x, y)$ is the Dirac delta function.

Thus, we have for ϕ as defined in eq (3)

$$\phi(x_0, y_0; u', v')=\iint\left[\delta(x-x_0, y-y_0)+i\sum_{n=-\infty}^{+\infty}\Delta_n\cdot\delta(x-x_0+n\omega, y-y_0)\right]\bar{f}(x, y)\exp\{i(u'x+v'y)\}dxdy$$

$$=[\bar{f}(x_0, y_0)+i\sum\Delta_n\cdot\bar{f}(x_0-n\omega, y_0)\exp\{-in\omega u'\}]\exp\{i(u'x_0+v'y_0)\}$$

or

$$|\phi|^2=|\bar{f}(x_0, y_0)|^2+2\cdot\mathrm{Im}\{\bar{f}(x_0, y_0)\sum\Delta_n^*\bar{f}^*(x_0-n\omega, y_0)\exp(in\omega u')\} \tag{7}$$

in which the asterisk denotes the complex conjugate, and Im $\{------\}$ indicates that the imaginary part is to be taken. Terms involving Δ^2 have been neglected. The final intensity would then be obtained by an integration of $|\phi|^2$ over the effective source $\gamma(x_0, y_0)$ as indicated in eq (1) above. The integration involved is of the form

$$C(0, n)=\iint\gamma(x_0, y_0)\bar{f}(x_0, y_0)\bar{f}^*(x_0-n\omega, y_0)dx_0dy_0 \tag{8}$$

which is the generalized partially coherent response as described by Hopkins.

Since we shall be concerned with pupils or Zernike plates which are symmetrical about the y_0-axis, $\bar{f}(x_0+u\omega, y_0)=\bar{f}(x_0-u\omega, y_0)$ and if, further, we restrict ourselves to cases where Δ_n is real, then eq (7) reduces to the following simple form:

$$|\phi|^2=|f(x_0, y_0)|^2+2\sum_{n=1}^{\infty}\mathrm{Im}\{\bar{f}(x_0, y_0)\bar{f}^*(x_0-n\omega, y_0)(2\Delta_n)\cos n\omega u'. \tag{7a}$$

The final intensity is thus given by

$$B'(u')=1+2\sum_{n=1}^{N}(2\Delta_n)\frac{\mathrm{Im}\{C(0, n)\}}{C(0, 0)}\cos n\omega u' \tag{9}$$

in which a normalization is effected by the constant term $C(0, 0)$. The C's in the above equation are as defined in eq (8). The summation has been shown to extend from 1 to N, where $N\omega\leq 1+\rho$ since $C(0, n)$ shall be 0 for larger values of n.

The problem now reduces simply to an evaluation of the C's with given Zernike plate and effective source characteristics.

4. Evaluation of $C(0, n)$

In this section we shall describe the mode of evaluation of $C(0, n)$. We shall consider first axial illumination of the object with a circular disk-shaped effective source. The radius of this source projected on the aperture of the objective is, say, ρ. The actual radius of the condenser aperture may be obtained from the following [viz: Som, 1963]:

$$n_c\cdot\sin\alpha_c=n_0\cdot\sin\alpha_0=n_0\cdot\rho\cdot\sin\alpha$$

where n_C and n_0 are the refractive indices of the media between the condenser and the object, and between the object and the objective respectively, α_C is the semiangular aperture of the condenser from the object point, α_0 is the corresponding semiangular aperture of the effective source projected on the objective, and α is the semiangular aperture of the objective. In what follows we shall consider only cases in which $\rho<1$.

Second we shall consider annular illumination, i.e., cases of an annular condenser aperture with radii 1 and $\rho_a < 1$. The objective shall be assumed to be free from aberrations. Further, the conjugate area of the Zernike plate shall have the same size and shape as that of the "effective source."

(i) Axial illumination:

Let us recall the expression for $C(0, n)$ in eq (8)

$$C(0, n) = \iint \gamma(x_0, y_0) \bar{f}(x_0, y_0) \bar{f}^*(x_0 - n\omega, y_0) dx_0 dy_0.$$

As indicated above, we may write

$$\begin{aligned} \gamma(x_0, y_0) &= 1 \text{ within a circle} \\ &= 0 \text{ outside.} \\ \bar{f}(x_0, y_0) &= f(x_0, y_0)\ p(x_0, y_0) \\ f(x_0, y_0) &= 1 \text{ within a circle} \\ &= 0 \text{ outside} \\ p(x_0, y_0) &= h e^{i\psi} \text{ within a circle} \\ &= 1 \text{ outside.} \end{aligned} \tag{10}$$

Figure 1 shows the geometrical implication of the integral (8). Evidently the region of integration is complicated by the various limits imposed on the functions that appear in the integrand. The values of $C(0, n)$ have been obtained by subdividing the area of integration into different areas of overlap of two circles of same or different radii. These latter areas could be easily determined analytically, and with the values of the function within these different subdivided areas, one would obtain the final values of $C(0, n)$ in terms of h, ψ, n, ω, ρ. They are given as follows:

$$\text{Im}\ \{C(0, n)\} = \left\{1 - D_0\left(\frac{n\omega}{\rho}\right)\right\} h \sin\psi \cdot \pi\rho^2 \qquad \text{for } \omega \leq 1-\rho$$

$$= \left\{1 - D_0\left(\frac{n\omega}{\rho}\right) - \frac{1}{2} D_0\left(\frac{2x_2}{\rho}\right) + \frac{1}{2\rho^2} D_0(2 \cdot \overline{n\omega + x_2})\right\} h \sin\psi \cdot \pi\rho^2$$

$$\text{for } 1-\rho \leq \omega \leq \sqrt{1-\rho^2}$$

$$= \left\{-D_0\left(\frac{n\omega}{\rho}\right) + \frac{1}{2} D_0\left(\frac{2x_2}{\rho}\right) + \frac{1}{2\rho^2} D_0(2 \cdot \overline{n\omega + x_2})\right\} h \sin\psi \cdot \pi\rho^2,$$

where

$$x_2 = \frac{1 - \rho^2 - \pi^2\omega^2}{2n\omega},\ n\omega + x_2 = \frac{(1-\rho^2) + n^2\omega^2}{2n\omega} \qquad \text{for } n\omega \geq 1-\rho^2,$$

$$C(0, 0) = \pi\rho^2 \cdot h^2 \tag{11}$$

and

$$D_0(x) = \frac{1}{\pi}\left[2 \cdot \cos^{-1}\frac{x}{2} - \sin \cdot \left(2 \cos^{-1}\frac{x}{2}\right)\right]. \tag{12}$$

It should be noted that $D_0(x)$ gives the response of a perfect lens system imaging a self-luminous object. These values are already tabulated, and hence the formulas for $C(0, n)$ given as above permit a straightforward evaluation, and also may be analyzed for aberrational effects with relative convenience.

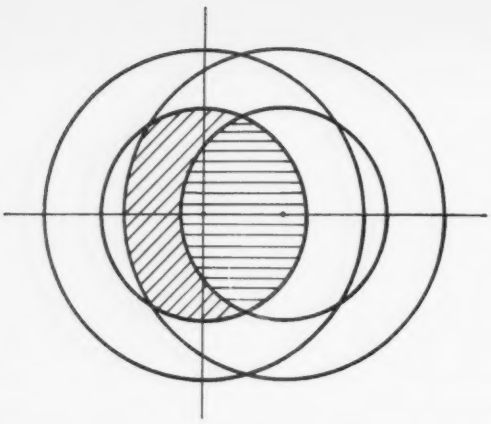

FIGURE 1. *Evaluation of* C(O,n); *axial illumination.*

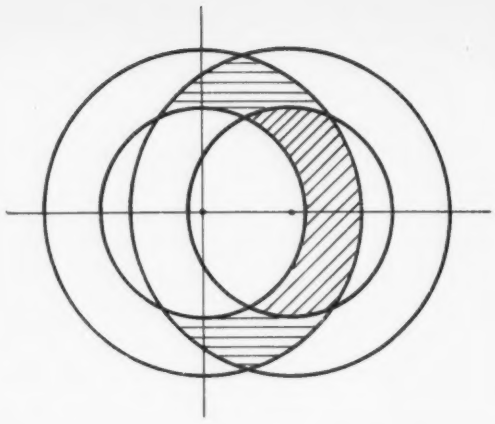

FIGURE 2. *Evaluation of* C(O,n); *annular illumination.*

(ii) Annular illumination: In this case, we have

$$\gamma(x_0, y_0) = 1 \text{ within an annulus bounded by circles } x_0^2+y_0^2=1 \text{ and } x_0^2+y_0^2=\rho_a^2$$
$$= 0 \text{ outside}$$
$$f(x_0, y_0) = 1 \text{ within a circle } x_0^2+y_0^2=1$$
$$= 0 \text{ outside}$$
$$p(x_0, y_0) = he^{i\psi} \text{ within an annulus bounded by circles } x_0^2+y_0^2=1 \text{ and } x_0^2+y_0^2=\rho_a^2$$
$$= 1 \text{ outside.}$$

Figure 2 shows a typical geometrical representation of the area of integration in this case. The values of $C(0, n)$ are as follows:

$$\text{Im}\{C(0,n)\} = \pi\rho_a^2\left[1-D_0\left(\frac{n\omega}{\rho_a}\right)\right]h\sin\psi \qquad \text{for } n\omega \leq 1-\rho_a$$

$$= \pi\rho_a^2\left[1-D_0\left(\frac{n\omega}{\rho_a}\right)-\frac{1}{2}D_0\left(\frac{1-\rho_a^2-\pi^2\omega^2}{n\omega\rho_a}\right)+\frac{1}{2\rho_a^2}D_0\left(\frac{1-\rho_a^2+n^2\omega^2}{n\omega}\right)\right]h\sin\psi$$

$$\text{for } 1-\rho_a \leq n\omega \leq \sqrt{1-\rho_a^2}$$

$$= \pi\rho_a^2\left[-D_0\left(\frac{n\omega}{\rho_a}\right)+\frac{1}{2}D_0\left(\frac{1-\rho_a^2-n^2\omega^2}{n\omega\rho_a}\right)+\frac{1}{2\rho_a^2}D_0\left(\frac{1-\rho_a^2+\pi^2\omega^2}{n\omega}\right)\right]h\sin\psi$$

$$\text{for } n\omega \geq \sqrt{1-\rho_a^2}.$$

$$C(0,0) = \pi(1-\rho_a^2)h^2. \tag{13}$$

5. Some Results

(i) Axial illumination:
(a) Singly periodic grating:

We shall first consider the results for a singly periodic phase-grating. Such a grating is represented by

$$A(u) = 1+i\cdot\Delta\cdot\cos\omega u$$
$$= 1+i\cdot\Delta\cdot\{\tfrac{1}{2}\cdot e^{i\omega u}+\tfrac{1}{2}\cdot e^{-i\omega u}\}.$$

Hence, from (9), we have

$$B'(u')=1+2a_1\cdot\Delta\cdot\cos\omega u' \tag{14}$$

where

$$a_1=\frac{\mathrm{Im}\,[C(0,1)]}{C(0,0)}. \tag{15}$$

With coherent illumination, i.e., in the limit of the effective source $\gamma(x_0, y_0)$ tends towards the Dirac delta function at the origin, a_1 tends towards $(\sin\psi/h)$ for all values of $\omega\leq 1$, so that the intensity distribution is given by

$$B'_c(u')=1+2\cdot\frac{\sin\psi}{h}\cdot\Delta\cdot\cos\omega u'. \tag{16}$$

Then the contrast in the image with partially coherent phase and amplitude contrast relative to that with a limitingly narrow-cone axial illumination is given by $a=\dfrac{a_1 h}{\sin\psi}$. Further, with narrow-cone axial illumination, the contrast will be zero for $\omega\geq 1$, while in the partially coherent case, this limit is $\omega\geq 1+\rho$ when a becomes zero. Thus, there is at least a possibility that there would be a gain in resolving power of the phase-contrast objective with a finite width of the illuminating beam. However, this is obtainable at the cost of contrast.

The values of a have been calculated for various values of ω and ρ. Figure 3 shows the results graphically. The following summarizes some of the pertinent observations in respect of the above.

(1) So long as $2\rho\leq\omega\leq 1-\rho$, the imagery in partially coherent light is indistinguishable from that with narrow-cone illumination in so far as the contrast is concerned. Hence, if one can have a prior knowledge of the range of frequencies in the object, it might be possible to choose

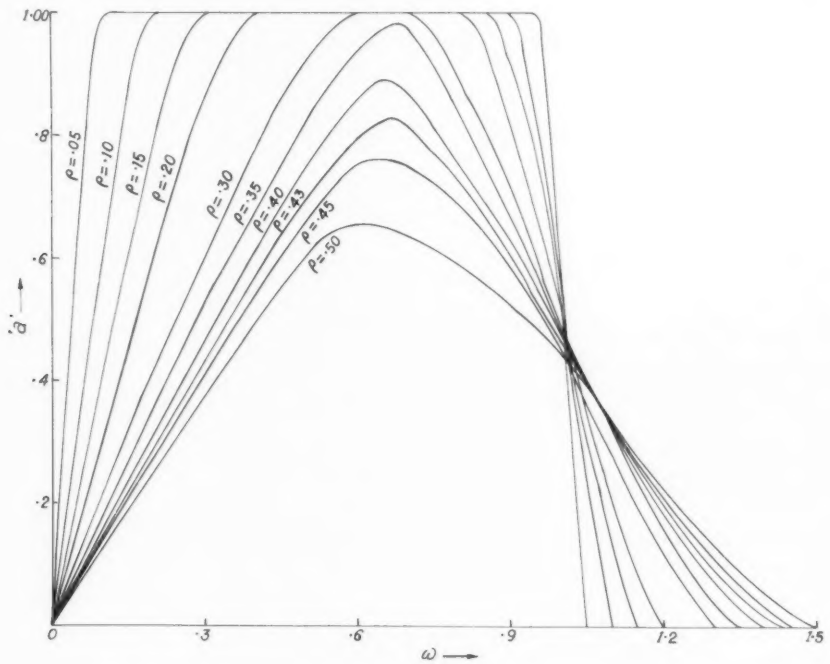

FIGURE 3. *Contrast in the images of phase gratings; axial illumination.*

a finite size of ρ to obtain a better photometric efficiency of the setup. Figure 4a shows the formation of the spectra under these conditions. All the spectra are wholly within the pupil and completely separated. That is why the ultimate image shows no difference in contrast from what is obtainable with coherent illumination.

(2) If $\omega<2\rho\leq 1-\rho$, the spectra are still wholly within the pupil, but they mutually overlap to a certain extent. Thus, not only the entire zero-order spectrum, but also parts of the first-order spectra are affected by the phase plate. This latter neutralizes the phase modulation, and hence contributes to a general loss in contrast. Figure 4b represents the state of affairs under these conditions.

(3) If $1+\rho>\omega>1-\rho$, parts of the first-order spectra fall outside the pupil and hence do not contribute to the image formation. The result is a further decrease in contrast. Figure 4c represents these conditions.

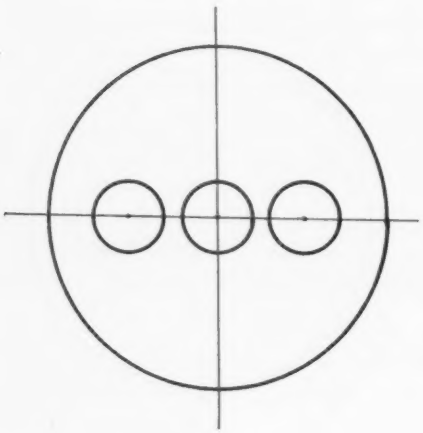

FIGURE 4a. *Formation of the spectra:* $2\rho\leqq\omega\leqq 1-\rho$.

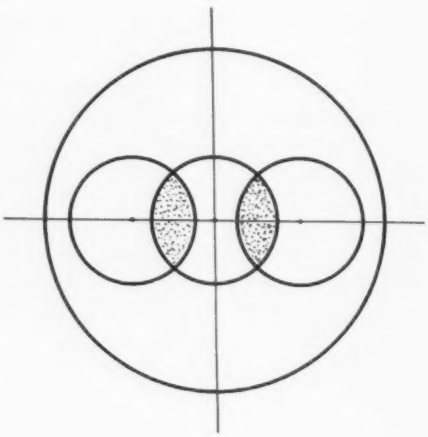

FIGURE 4b. *Formation of the spectra;* $\omega<2\rho\leqq 1-\rho$.

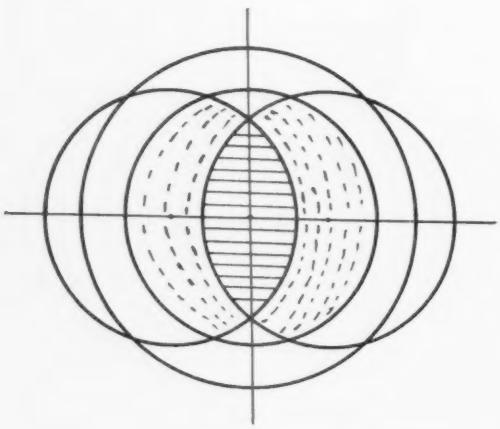

FIGURE 4c. *Formation of the spectra;* $1+\rho>\omega>1-\rho$.

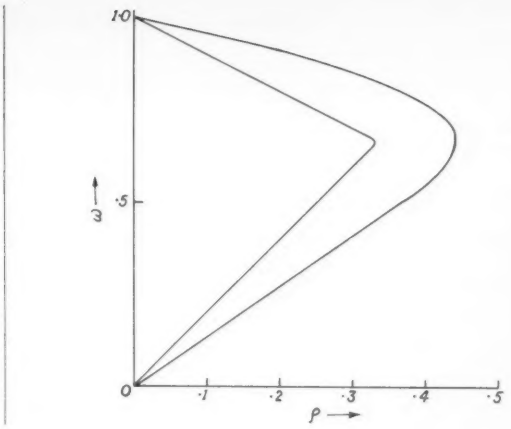

FIGURE 5. *Useful frequency-range for partially coherent phase-contrast images.*

The values of a as shown in figure 3 may now be analyzed in the light of the above observations. Figure 5 shows (i) the range of frequencies which shall have a contrast same as in the coherent case for different values of ρ, and (ii) the range of frequencies for which the relative contrast is equal to 0.8. This gives one an idea of the permissible maximum size of source that can be used for a satisfactory phase contrast image.

The curves in figures 3 and 5 have been drawn for cases when $h=1$, that is, when no amplitude modulation is used. Further sin ψ has been taken as unity as well. This implies that the phase of the zero-order spectrum is advanced or retarded by $\pi/2$. Noting that a_1 is proportional to sin ψ, the maximum phase contrast efficiency is obtained at this value. However, a_1 is seen to be inversely proportional to h, meaning thereby that the contrast may be enhanced by using a slight amplitude contrast as well. This, of course, is possible at the cost of the mean level of illumination of the final image.

(b) Square-topped phase-grating:

This is the case of a simple periodic structure where troughs and crests represent differences in optical path only.

Let

$$A(u)=1+i\Delta(u) \tag{17}$$

where $\Delta(u)$ is periodic in u with a fundamental length of period $2u_0$. Let, over one such fundamental interval,

$$\Delta(u)=0 \qquad \alpha u_0 \leq |u| \leq u_0$$

$$=\Delta \qquad |u| \leq \alpha u_0.$$

The Fourier spectrum is given by

$$\Delta_n=\Delta_{-n}=\frac{\sin \alpha n\pi}{n\pi}\,\Delta. \tag{18}$$

α in the above gives the ratio between the line width to line separations. Hence, from eq (9), we have

$$B'(u')=1+2\Delta\cdot\sum_{n=1}^{N} 2\cdot\frac{\sin\cdot\alpha\cdot n\pi}{n\pi}\cdot\left[\frac{\mathrm{Im}\,\{C(0,n)\}}{C(0,0)}\right]\cos n\omega u' \tag{19}$$

where $N\omega \leq 1+\rho$.

In the limit of a point source, the expression for intensity will be

$$B'(u')=1+2\Delta\sum_{n=1}^{N}\left(2\cdot\frac{\sin\cdot\alpha n\pi}{n\pi}\right)\left(\frac{\sin\psi}{h}\right)\cos\cdot n\omega u' \tag{20}$$

where $N\omega\leq 1$ since Im $[C(0, n)]$ in the coherent limit will be $h \sin \psi$ for all values of $n\omega\leq 1$.

Figures 6a to d show the image of such gratings ($\Delta=0\cdot 5$) for four different frequencies, and for various effective source sizes at each frequency. The dotted curves represent an ideal case of linear unitary transformation of phase variation into amplitude variation.

The expression for $B'(u')$ in eq (19) or for $B'_c(u')$ in eq (20) shows that the final image is given by a truncated Fourier series, and hence one would expect to observe the so-called Gibbs' phenomenon of large oscillations in the region of the edges of the square-topped grating. In the presence of harmonics in the image intensity distributions it is indeed a bit difficult to define a unique contrast for such cases. The presence of these harmonics is in fact an indication of the effect of nonlinearity in the intensity transmission in partially coherent light, and as yet no unique specification has been suggested for a proper measure of such nonlinear effects. One suggestion is to express the contrast in terms of the fundamental frequency distribution, and lump together the effects of higher harmonics in a so-called "remnant" [Ingelstam, 1964]. This "remnant" may be described as the square root of the sum of the squares of all coefficients other than the constant and that of the fundamental frequency component. Figure 7 gives a plot of this fundamental contrast and the remnant against source sizes for different frequencies.

It is of interest to note that the remnant always decreases with increasing frequency, falling gradually down to zero. In fact, if $N<2$, there are no harmonics in the image intensity distribution. Thus, for a frequency up to 0.5, harmonic distortion would be present for all source sizes, though its magnitude as reflected in the value of the "remnant" may be negligibly small. For values of ω lying between 0.5 and 1, the "remnant" would be zero only if ρ is less than a certain value given by $\rho<2\omega-1$.

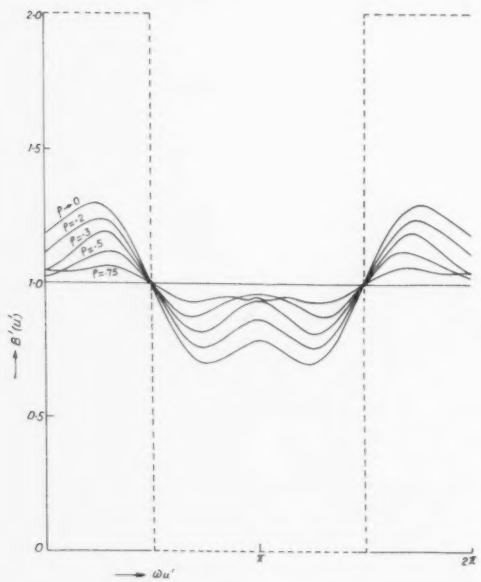

FIGURE 6a. *Images of square-topped phase gratings; axial illumination; $\omega=0.25$.*

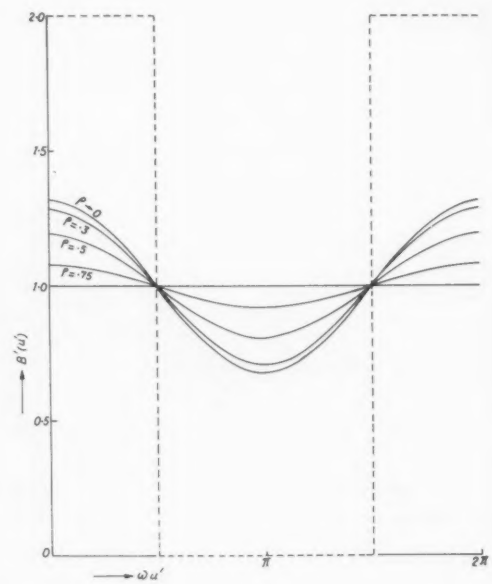

FIGURE 6b. *Images of square-topped phase gratings; axial illumination; $\omega=0.50$.*

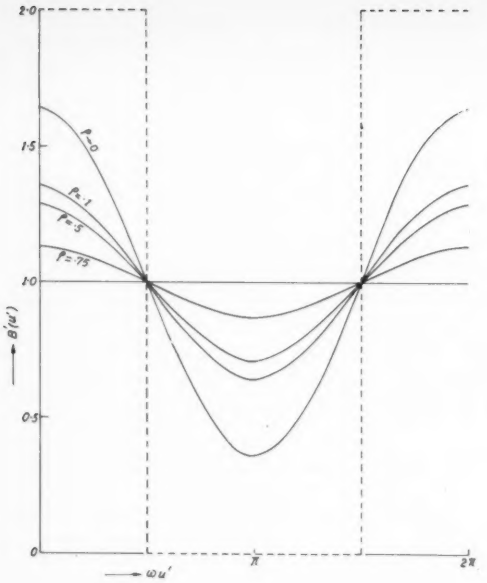

FIGURE 6c. *Images of square-topped phase gratings; axial illumination; $\omega = 1.0$.*

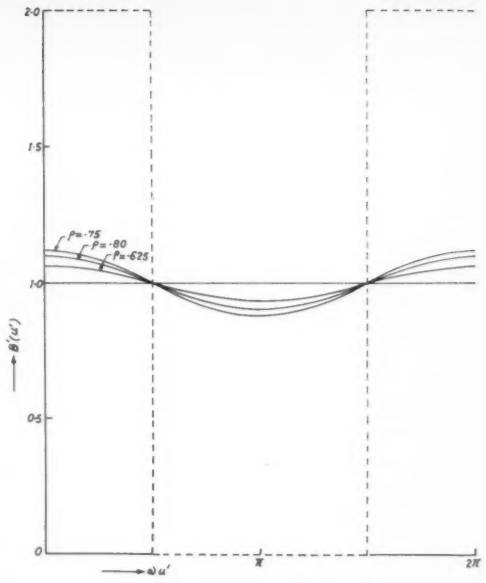

FIGURE 6d. *Images of square-topped phase gratings; axial illumination; $\omega = 1.5$.*

FIGURE 7. *"Fundamental contrast" and "remnants" in the images of square-topped phase gratings; axial illumination.*

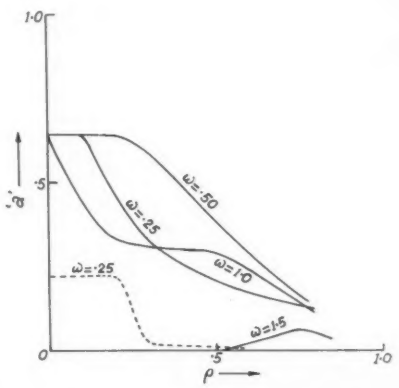

In the cases for which computation has been done, α has been chosen as equal to 1/2, implying equal widths for the troughs and crests of the phase grating. In these cases, the spectra consist of only the odd harmonic components and hence the "remnant" would be zero if $N<3$; i.e., if $\rho<3\omega-1$, $\omega>0.33$. This expresses the range of validity of using the criterion of "fundamental contrast" for the study of the efficiency of phase-contrast devices in partially coherent light.

(ii) Annular illumination:

(a) Singly periodic grating.

The expression for intensity is the same as in the previous case, except that the values of Im $[C(0, n)]$ to be used are as given in (13).

If the width of the annular source tends towards an infinitesimally small value, the area integral for $C(0, n)$ will tend towards a line integral, and we shall have

$$\lim_{\rho_a \to 1} \text{Im}\,[C(0, n)] = 2 \cdot \cos^{-1} \cdot \left(\frac{n\omega}{2}\right) h \sin\psi$$

$$\lim_{\rho_a \to 1} [C(0, 0)] = 2\pi h^2. \tag{21}$$

Thus, unlike the case of axial illumination discussed above, we have in this case a contrast varying with frequency even with a source of infinitesimally narrow width; we have, in this limiting case,

$$B_c' = 1 + 2\Delta \cdot \left(\frac{\cos^{-1} \cdot \frac{n\omega}{2}}{\pi}\right)\left(\frac{\sin\psi}{h}\right)\cos\,\omega u'. \tag{22}$$

The difference with the corresponding expression (16) for the axial case is to be noted with interest.

Evidently in this case the limiting resolvable frequency is $n\omega \leq 2$. This is just a theoretical limit, as the contrast also tends towards zero at the limit.

If we now consider the case of the annular source with a finite width, we shall find that Im $[C(0, n)]$ becomes zero for $n\omega > 1 + \rho_a$ which implies that we lose on the count of ultimate resolving power. Figure 8 shows graphically the values of $a_n = \text{Im}\,[C(0, n)]/C(0, 0)$ as a function of frequency ω for various values of ρ_a. The dashed curve in figure 8 indicates the range of frequencies which are so imaged that the relative contrast is nowhere less than 0.8.

(b) Square-topped grating:

As in the case of axial illumination, we have, in the limit of a line source coinciding with the margin of the pupil,

$$B_c'(u') = 1 + 2\Delta \sum_{n=1}^{N} \left(\frac{\sin \cdot \alpha \cdot n\pi}{n\pi}\right)\left(\frac{2\beta_n}{\pi}\right)\left(\frac{\sin\psi}{h}\right)\cos \cdot n\omega u' \tag{23}$$

where

$$\beta_n = \cos^{-1} \cdot \frac{n\omega}{2} \text{ and } N \leq (1 + \rho_a)/\omega.$$

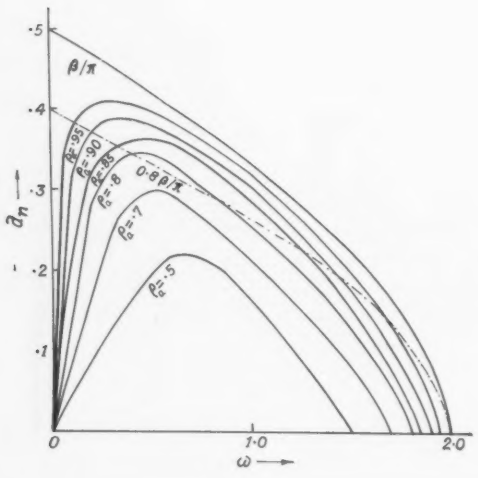

FIGURE 8. *Contrast in the images of phase gratings; annular illumination.*

With a finite width of the source, we have an expression similar to (20) above. Figures 9a to d show the images of such gratings ($\Delta=0.5$) of a number of frequencies $\omega=\frac{\pi}{u_0}$, where $2u_0$ is the length of the period, and $\alpha=\frac{1}{2}$ implies equal widths for the troughs and crests of path-differences

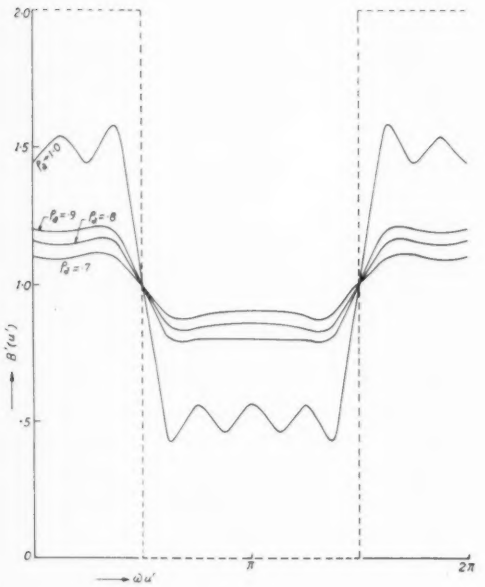

FIGURE 9a. *Images of square-topped phase gratings; annular illumination; $\omega=0.25$.*

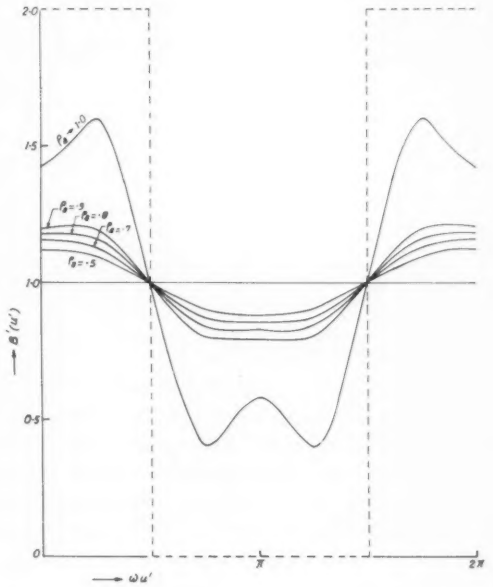

FIGURE 9b. *Images of square-topped phase gratings; annular illumination; $\omega=0.50$.*

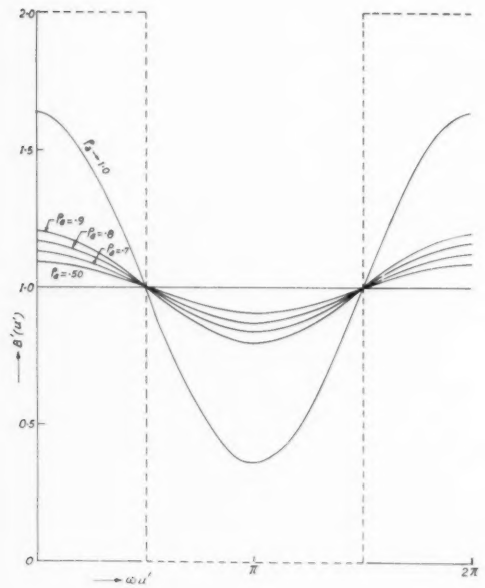

FIGURE 9c. *Images of square-topped phase gratings; annular illumination; $\omega=1.0$.*

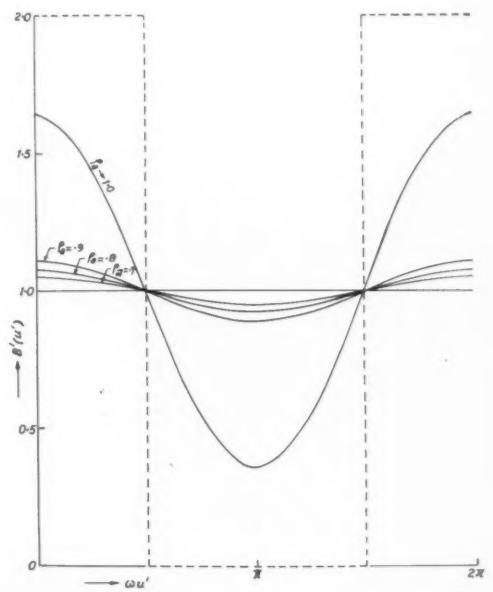

FIGURE 9d. *Images of square-topped phase gratings; annular illumination; $\omega=1.5$.*

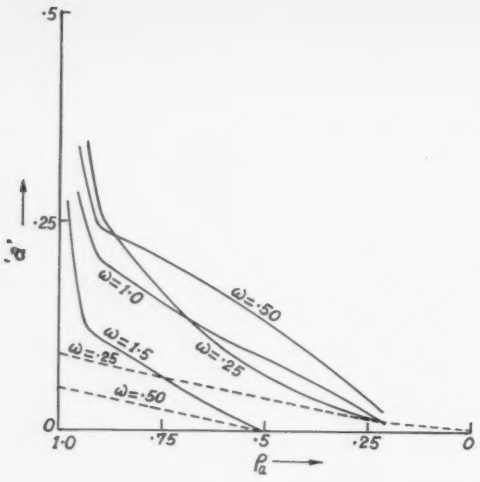

FIGURE 10. *"Fundamental contrast" and "remnants" in the images of square-topped phase gratings; annular illumination.*

in the grating. The dotted curves represent an ideal case of linear unitary transformation of phase variation into amplitude variation. Here also we may make the same remarks as done in the case of axial illumination of square-topped gratings. Figure 10 describes the situation, and the conclusions are also similar. Remembering that the coherent limit of resolution in this case is 2, we find that practically the upper half of the range of resolvable frequencies is still assessable in terms of the "fundamental contrast" only.

This study has been undertaken under the sponsorship of the National Bureau of Standards. The authors are deeply indebted to the stimulating discussion with S. C. Som on the various aspects of this study.

References

De, M. and Som, S.C. (1963), J. Opt. Soc. Am. **53**, 779.
Hopkins, H.H. (1952), Rev. Opt. (Paris), 142.
Hopkins, H.H. (1953), Proc. Roy. Soc. **A217,** 408.
Hopkins, H.H. (1957), J. Opt. Soc. Am. **47,** 508.
Ingelstam, E., "Attempts to treat non-linear imaging devices" an abridged version of an invited paper given at the ICO Conference on Photographic and Spectroscopic Optics in Tokyo and Kyoto, September, 1964.
Kahn, F.D. (1955), Proc. Phys. Soc. **B68,** 1073.
Osterberg, H. (1944), J. Opt. Soc. Am. **34,** 773.
Osterberg, H. and Wilkins, J. (1949), J. Opt. Soc. Am. **39,** 553.
Picht, J. (1936), Z. Instrumentenk. **56,** 481.
Slansky, S. (1962), Opt. Acta. **9,** 277.
Steel, W.H. (1958), Proc. Roy. Soc. **A249,** 574.
Zernike, F. (1934), Physica **1,** 689.
Zernike, F. (1942), Physica **9,** 686, 974.

(Paper 69C3–200)

JOURNAL OF RESEARCH of the National Bureau of Standards—C. Engineering and Instrumentation
Vol. 69C, No. 3, July–September 1965

Exposure Time Relations for Kossel Microdiffraction Photographs

H. Yakowitz and D. L. Vieth

(April 23, 1965)

The exposure time for a Kossel photograph may vary from a few seconds to a few hours. Therefore, it is desirable to be able to estimate the exposure time for various experimental conditions. Hence, semiempirical relations for the exposure time of a Kossel microdiffraction pattern have been developed. Equations are presented for both transmission and back reflection Kossel photographs. These equations are tested for validity using two different commercially available x-ray films. It is shown that the agreement of actual exposure times with predicted exposure times is valid within 10 to 15 percent.

It has long been known that the exposure time of a Kossel photograph has a well-defined optimum [1].[1] However, useful analytical expressions enabling one to calculate the exposure time have not been presented. Therefore, the purpose of this paper is to propose expressions for the exposure time in both the transmission and the back reflection Kossel regions.

In the transmission mode, the Kossel conics usually appear light on a darker background and the contrast is, at best, not good [2, 3]. In the back reflection region, the conics appear darker than the background, and the contrast may be somewhat better than in transmission [2]. The only practical source for Kossel patterns is a finely focused electron beam which is allowed to strike either the sample or a source foil in close proximity to the sample. The latter case will be discussed as it is the more general and more useful. It will be assumed that the film is in a vacuum and that once the x rays leave the sample, having undergone the usual exponential reduction in intensity, they travel unimpeded to the film. If an x-ray window and airpath intervene, the reduction in intensity of the x rays emergent from the sample can also be accounted for by the usual exponential retardation law which simply appears as a multiplier.

Using a focused beam of electrons, one may vary the specimen current, i.e., the number of electrons flowing to ground per unit time from specimen or foil, and the accelerating potential of the electrons. A knowledge of the number of photons per electron which strike the film and of the film area is necessary. Some provision for the fact that the exposure is not constant over the expanse of a flat film is also necessary. Bearing each of these requirements in mind, we may write for the exposure:

$$E=(60t)\frac{(i_s)}{(1-r)}(G)\left(\frac{\Omega_s}{A_F}\right)\left[\frac{(n_K)_f}{4\pi}\right]6.25\times10^{12}\,[\exp\,[-(\bar{\mu}_f x_f+\bar{\mu}_s x_s)]], \quad (1)$$

where

E is the exposure in photons/cm^2.
i_s is the specimen current in microamperes.
G is a factor accounting for variation of exposure with position on the flat film.
Ω_s is the solid angle subtended by the spherical segment containing the film.
A_F is the exposed film area in cm^2.
$(n_K)_f/4\pi$ is the total number of K photons produced per unit solid angle by the foil per incident electron.
6.25×10^{12} is the number of electrons per microcoulomb of charge.
r is the electron backscatter coefficient of the foil [4].
$\bar{\mu}_f$ and $\bar{\mu}_s$ are the equivalent linear absorption coefficients for the total spectrum produced in the foil and the sample respectively in cm^{-1} [1].
x_f and x_s are the thicknesses in cm of the foil and sample respectively.
t is the exposure time in minutes.

Values of $n_0\equiv[(n_K)_f/4\pi]$ as a function of atomic number and the accelerating potential of the electrons are available in the literature [5, 6, 7]. The area of the film can be found by reference to figure 1 as:

$$A_F=\pi D^2\tan^2\eta, \quad (2)$$

where

D is the source to film distance in cm;
η is the half-cone angle subtended by the film.

[1] Figures in brackets indicate the literature references at the end of this paper.

The values of D and η are usually well known.

The inclusion of G arises from the fact that the exposure will be greatest at the film center and least at the edge. This is a combination of two effects, the first of which is an increasing absorption path within the sample with increasing angle of emergence. The other effect is that of the geometry, i.e., a unit of solid angle subtends a larger area on the film at the edge than at the center. It has been observed that the net effect is a slowly decreasing function of the angle η. This can be suitably approximated by defining G as:

$$G \equiv \left[\frac{1+\cos\eta}{2}\right]. \tag{3}$$

Over the usual range of η values, i.e., $20° \leq \eta \leq 36°$, the inclusion of this form of G increases the exposure time 3 to 10 percent. It is interesting to note that the important central film area in figure 1 defined by the angle $\eta/2$ and the ray, Q, will be nearly uniformly blackened.

The factor $\frac{i_s}{1-r}$ is

the beam current, i.e., the incident electron current. It is for this current that n_0 values have been derived. The simple value "r" can be used since the effect on the specimen current, i_s, due to secondary electrons which may be generated is quite small.

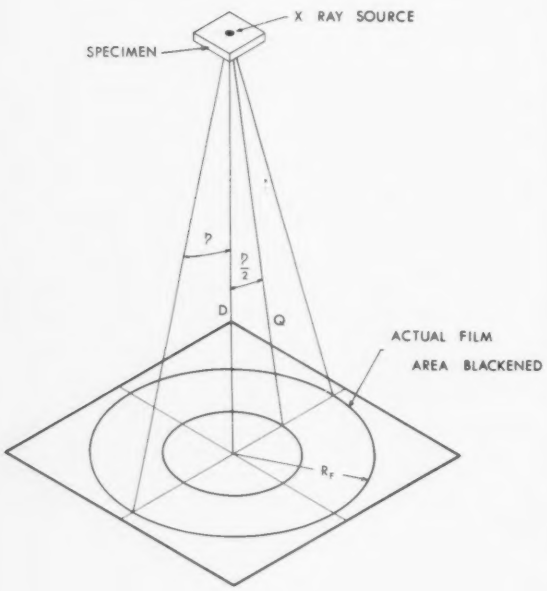

FIGURE 1. *Geometrical relations between the x-ray source and the film.*

The solid angle subtended by the spherical segment containing the film is given by [8]:

$$\Omega_s = 2\pi(1-\cos\eta). \tag{4}$$

Thus, $(n_0\Omega_s)$ is a measure of the number of photons per incident electron which would actually fall on the film if there were no exponential absorption.

The value $\bar{\mu}$ can be approximated by the relation $\bar{\mu} \approx \frac{4}{3}\mu$, μ being the linear absorption coefficient for K_α or L_α, for excitation over-voltage ratios of 3 to 4 [3] and for most μ values used in Kossel analysis. The value of x_f should be kept as small as practical. The value of x_s should be the approximate optimum thickness for the transmission case [3]. In back reflection, an effective depth can be taken as an approximation to x_s. This point will be discussed later.

Equation (1) may now be rewritten as:

$$E = (t)\,\frac{(i_s)}{(1-r)}\,\frac{1+\cos\eta}{2}\,2\pi\,\frac{(1-\cos\eta)n_0}{\pi D^2\tan^2\eta}\,(3.75\times10^{14})\,\{\exp-[\tfrac{2}{3}(\mu_f x_f+\mu_s x_s)]\}. \tag{5}$$

Solving for t we obtain:

$$t\ (\text{min}) = \frac{2.67\times10^{-15}E\ (\sec^2\eta)D^2}{n_0 i_s}\,(1-r)\,\{\exp-[\tfrac{2}{3}(\mu_f x_f+\mu_s x_s)]\}. \tag{6}$$

It is necessary to obtain a value for E empirically for each type of film to be used. This E value, henceforth called E_0, is that exposure density yielding the maximum contrast between the Kossel conics and background for a given film at a given distance, D. It is emphasized that the E_0 value in eq (6) represents a compromise between the exposure at the extreme edges of the film and the exposure at the film center. It is to be expected that the exposure density E_0 will be essentially constant for a given film type, independent of other camera parameters.

Equation (6) as written is strictly speaking only applicable to transmission Kossel photographs. In the back reflection region, precisely the same relation holds true except that x_s is undefined. However, a reasonably good approximation to x_s can be made.

Such an approximation can be made following Il'in's treatment [9]. Il'in proposes an effective thickness, d_f, of the absorbing layer chosen such that the function $\exp-(\mu d_f)$ would give total attenuation of an analytic line such as $K\alpha_1$ or $L\alpha_1$, in the working volume of the specimen, i.e., at $\eta = 90°$. It is presumed that

$$\rho d_f = H \tag{7}$$

in which ρ is the density of the specimen and H is a constant for a given η value. As support for eq (7) the fact that d_f is related to the total thickness of the emitting portion of the target is invoked [9].

According to the Whiddington law, this thickness is determined for a given accelerating potential by the density of the emitter.

By rearranging Il'in's relations [10] and invoking electron probe microanalyzer results presented in the literature [11–14], it is possible to plot an H versus η curve. This plot is shown in figure 2.

Noting that x_s is to be replaced by d_f in eq (6) for back reflection cases, one obtains:

$$\mu_s x_s = \mu_s d_f = H(\mu/\rho)_s. \tag{8}$$

Hence for back reflection, eq (6) becomes

$$t\ (\text{min}) = \frac{2.67\times10^{-15} E\ (\sec^2\eta) D^2}{(n_0)(i_s)} (1-r) \{\exp -\tfrac{2}{3}[\mu_s x_s + H(\mu/\rho)_s]\} \tag{9}$$

In order to test the validity of eqs (6) and (9), the value of E was calculated for two different film types commonly used in the preparation of Kossel microdiffraction photographs. One of these was moderately coarse-grained duplitized film [2] while the other was a moderately fine-grained single emulsion film.[3] These shall be designated I and II respectively.

Using type I film for about 200 Fe-K radiation exposures of Fe-3 w/o Si alloy, it was found that the value of E_{I} was 1.6×10^8 photons/cm^2 for high contrast, high resolution transmission photographs [15].

For type II film, the exposure time versus iron thickness curve given by Morris and Ogilvie [16] was used to calculate E_{II}. The value obtained was 1.4×10^9 photons/cm^2. Inserting the values of E_{I} and E_{II} into eq (6) we obtain:

$$t_{\text{I}}\ (\text{min}) = \frac{4.1\times10^{-7} D^2\ (\sec^2\eta)}{(i_s)(n_0)} (1-r) \{\exp -[\tfrac{2}{3}(\mu_f x_f + \mu_s x_s)]\}. \tag{10a}$$

$$t_{\text{II}}\ (\text{min}) = \frac{4.0\times10^{-6} D^2\ (\sec^2\eta)}{(i_s)(n_0)} (1-r) \{\exp -[\tfrac{2}{3}(\mu_f x_f + \mu_s x_s)]\}. \tag{10b}$$

It remained to check eqs (10) with independent data. For type I film, Gielen's exposure of germanium with Cu-K radiation was used [17]. The required parameters were:

$D=6$ cm
$\eta=20.3°$
$i_s=0.11\mu$A
$n_0=2.2\times10^{-4}$ photons/electron/unit solid angle at 30 keV [7]
$x_f=17.8\times10^{-4}$ cm
$\mu_f=455$ cm^{-1}
$x_s=1.52\times10^{-2}$ cm
$\mu_s=385$ cm^{-1}
$r_{\text{Cu}}=0.29$.

[2] Kodak AA film.
[3] Kodak M film.

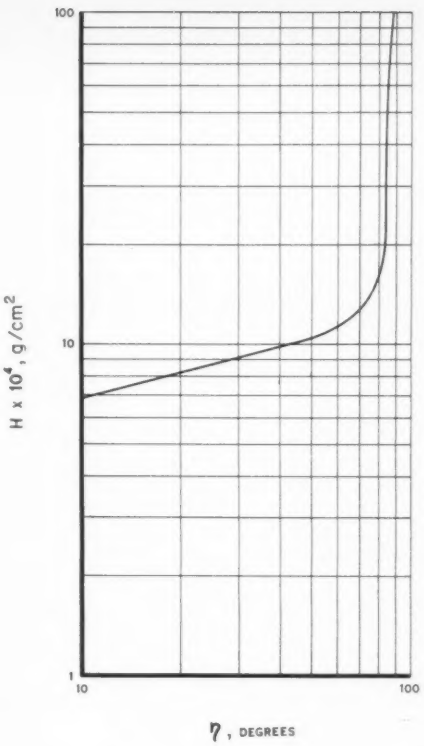

FIGURE 2. *The value of* H *as a function of the half-angle of the film,* η.

Gielen used a camera with an aluminum foil light-tight cap. The (μx) value of the foil was 0.20. The camera operated in vacuum. Using these data, eq (12a) predicted an exposure time of 49 min. The actual exposure time for a high-contrast photograph was 50 min [18].

In order to check both eqs (9) and (10b), a back reflection photograph of iron using Fe-K radiation taken on type II film was used as a model [19]. The required parameters were

$D=12.4$ cm
$\eta=26°$
$i_s=2.0\mu$A
$n_0=6\times10^{-4}$ photons/electron/unit solid angle at 40 keV [6]

$x_f=0$

$(\mu/\rho)^{F_e}_{F_e}=71.4$

$H=8.5\times10^{-4}$ at $\eta=26°$

$r_{Fe}=0.27$.

Using these data, the predicted exposure time is 0.47 min or 28 sec. The actual time was 25 sec [19].

It is perhaps of interest to comment that for a given set of conditions a simple equation results. For example, using the equipment parameters given for the iron exposure in back reflection, one obtains:

$$t_{\mathrm{I}}=\frac{7.8\times10^{-5}}{(n_0)(i_s)}\,(1-r)\,\exp\,[5.7\times10^{-4}(\mu/\rho)_s+0.67\mu_f x_f] \tag{11a}$$

$$t_{\mathrm{II}}=\frac{7.4\times10^{-4}}{(n_0)(i_s)}\,(1-r)\,\exp\,[5.7\times10^{-4}(\mu/\rho)_s+0.67\mu_f x_f]. \tag{11b}$$

It has been shown that eqs (6) and (9) represent the correct form of exposure time relations for Kossel photography. Because of the approximations made, e.g., for $\bar{\mu}$ and d_f, the uncertainties in absorption coefficients themselves, and possible inherent sample limitations [1], the value of an empirical E_0 is probably good to only 10 or 15 percent. Hence, agreement with eqs (10) and (11) to only about 10 to 15 percent is to be expected. Nevertheless, this is a significant improvement over a pure trial and error method. Furthermore, as more exposures are taken E_0 values can be refined.

In the transmission method, there appears to be a definite upper limit on $(\mu_s x_s)$ in order to obtain any pattern [3]. This limit is about $\mu_s x_s=10$. It is therefore recommended that eq (6) not be employed with values of $\mu_s x_s>10$.

The photographs used to determine the E_{I} values were prepared while one of the authors (HY) was a guest of the Massachusetts Institute Technology assigned to the laboratory of Prof. R. E. Ogilvie.

References

[1] K. Lonsdale, Divergent-beam x-Ray photography of crystals, Phil Trans Roy. Soc. (London) **A-240,** 219 (1947).
[2] T. Imura, Study of the deformation of single crystals by divergent x-ray beams, Bull. Naniwa Univ. **A-2,** 51 (1954).
[3] H. Yakowitz, Approximate optimum sample thickness for transmission Kossel photographs, to be published.
[4] D. M. Poole and P. M. Thomas, Quantitative electron-probe microanalysis, U.K. Atomic Energy Auth. Rept. AERE–R–3815, 16 pp. (1961).
[5] D. B. Brown and R. E. Ogilvie, Efficiency of production of characteristic x-radiation from pure elements bombarded by electrons, J. Appl. Phys. **35,** 309 (1964).
[6] M. Green and V. E. Cosslett, The efficiency of production of characteristic x-radiation in thick targets of a pure element, Proc. Phys. Soc. (London) **78,** 1206 (1961).
[7] M. Green, The efficiency of characteristic x-radiation, Thesis to Cambridge University, 246 pp. (1962).
[8] Standard Mathematical Tables, ed. C. D. Hodgman, 10th ed., Chemical Rubber Publishing Company, Cleveland, Ohio (1954), p. 340.
[9] N. P. Il'in, On the possibility of quantitative analysis by means of x-ray spectra without the use of standards, Izvest. Akad. Nauk S.S.S.R. Ser. Fiz. **25,** No. 8, 929 (1961). Translated in Bull. Acad. Sci. U.S.S.R. Phys. Ser. **25,** No. 8, 940 (1962).
[10] H. Yakowitz and J. R. Cuthill, A survey of correction procedures for electron probe microanalysis data, unpublished.
[11] L. S. Birks, Calculation of x-ray intensities from electron probe specimens, J. Appl. Phys. **32,** 387 (1961).
[12] R. Castaing, Electron probe microanalysis, Adv. Electron and Electron Phys. **13,** 317 (1960).
[13] M. Devin Quoted by J. Philbert in The Castaing "microsonde" in metallurgical and mineralogical research, J. Inst. Metals **90,** 241 (1962).
[14] D. B. Wittry, Notes from a special course on electron probe microanalysis, Univ. Southern Calif. 1962.
[15] H. Yakowitz, Work performed at MIT on Fe–3 w/o Si alloys. See ref. [18] for actual photographs.
[16] W. G. Morris and R. E. Ogilvie, Kossel studies of iron whiskers, Air Force Materials Laboratory Rept. RTD–TDR–63–4198, 27 pp. (1964).
[17] P. Gielen, Kossel line studies in cubic crystals, S.M. Thesis to MIT, 48 pp. (1964).
[18] P. Gielen, Private communication, 1964. See P. Gielen, H. Yakowitz, D. Ganow and R. E. Ogilvie, Evaluation of Kossel microdiffraction procedures: The cubic case, J. Appl. Phys. **36,** 773 (1965) for actual photograph.
[19] Applied Research Laboratories, The 40350 Kossel Line Camera, Special Announcement (1964).

(Paper 69C3–201)

JOURNAL OF RESEARCH of the National Bureau of Standards—C. Engineering and Instrumentation
Vol. 69C, No. 3, July–September 1965

Cartesian Diver as a Density Comparator

Horace A. Bowman and Randall M. Schoonover

(March 25, 1965)

A hydrostatic weighing system is described that provides independent values of apparent mass with a standard deviation of about 0.2 microgram. The definition of "independent" used here includes the requirement that the sample under observation be removed from the water, dried, and recleaned between measurements. This precision is between one and two orders better than existing hydrostatic balances, and permits high-quality density measurements without recourse to large sample sizes. The system is used as a comparator, hence the absolute accuracy of results can be no better than that of the standards used. Data are presented which were taken during experiments on two 2-gram pieces of single crystal silicon, and the standard deviation in density of a single determination was computed to be 4.4×10^{-7} g/cm³ (0.22 ppm).

The system is particularly well suited to detection of slight density changes in small size samples. In this service, it is not subject to the requirement for high accuracy standards. Data are reported on density changes of about 50 ppm that occurred in a 250 milligram ceramic crystal. Two independent determinations on this change differed by only 7 percent.

1. Introduction

The density of an irregularly shaped object is usually determined by a combination of air and water weighing in which the apparent mass of the object is determined in both media. The apparent mass in air, A, is determined on a balance in the usual manner. The apparent mass in water, B, is determined by suspending the object from one pan of the balance by a fine wire into a body of water. The mass, M, and volume, V (the ratio of which is density), result immediately from a simultaneous solution of

$$A=M-\rho_A V \text{ (air weighing)}$$

$$B=M-\rho_W V \text{ (water weighing)}$$

where ρ_A is the density of the air displaced by the object during the air weighing, and ρ_W the density of the water displaced by the object during the hydrostatic weighing.

The main limitation in the above scheme occurs in the determination of B. There are two reasons for this:

(1) Although we know the density of a particular sample of water to almost two orders better than we know the density of a particular sample of air, water density is about three orders greater than that of air. Hence, the uncertainty in $\rho_W V$ is greater than that of $\rho_A V$.

(2) In water weighing, the variability of nonbuoyant forces is of much greater magnitude than those occurring in air weighing. *First*, there are variable momentum forces associated with turbulence and convective currents in water which act on the object being weighed. Such forces also exist in air weighing but to a much smaller extent. *Second*, there is variability in surface tension forces associated with the meniscus surrounding the point where the support wire penetrates the water surface. Under nonideal conditions, these forces may vary by 10 μg or more.

Thus, the accuracy in a measured value of B is limited by our knowledge of ρ_W, and the reproducibility of the measured value is limited by the variability of the nonbuoyant forces mentioned above.

For a given hydrostatic weighing system the absolute value of the variability (due to nonbuoyant forces) is largely independent of load. Hence, to achieve improved values of percentage reproducibility in B, we must use samples of very large sizes.

Unfortunately, objects for which density determinations have the maximum scientific value are rarely available in samples of unlimited sizes. It is seldom that samples above 2 g are obtainable, and they are usually of fractional-gram size. Such items as uniformly irradiated crystals, samples of maximum purity substances, and balance sensitivity weights, usually weigh 250 mg or less. For a 250-mg object, a variability of 10 μg in the nonbuoyant forces would result in a variability in B of about $40:10^6$—a highly unsatisfactory measurement for many technical purposes.

In the Cartesian diver system to be described, it is possible to determine B of a 250-mg object to a reproducibility (standard deviation) of about $1:10^6$. The reason for this is that the two major sources of variability in ordinary hydrostatic weighing do not exist in the diver system or are minimized:

(A) No portion of the diver structure penetrates a water surface, so uncertainties caused by surface tension do not exist.

(B) The diver system is operated at a nominal temperature of 4 °C; hence, nonideal thermostating does not result in variability of water density. In the absence of density gradients (other than those

caused by gravity) convection currents cannot become established, and turbulence damps out quickly. Thus momentum forces are minimized. It is generally considered impractical to perform ordinary hydrostatic weighing at 4 °C.

2. Description of the System

The Cartesian diver is not a new device. A review of prior art is given by Chiarulli and Chilton [1].[1] Recent work by Haller and Calcamuggio [2] and Spaepen [3] has raised the state of the art greatly.

Basically the diver, figure 1, is a hollow, compressible body with a closed surface to which are attached various hooks, guides, and reticles to facilitate loading, manipulation, and observation. When such a body is immersed in water and the pressure in the water is increased, the positive buoyancy of the body will decrease or increase respectively, depending upon whether the compressibility of the diver is greater than or less than that of water. If diver compressibility is equal to that of water, buoyancy is independent of pressure.

[1] Figures in brackets indicate the literature references at the end of this paper.

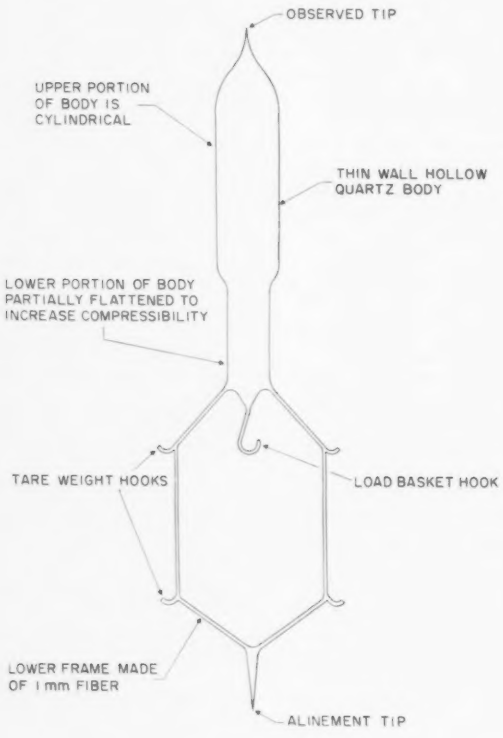
OBSERVED TIP
UPPER PORTION OF BODY IS CYLINDRICAL
THIN WALL HOLLOW QUARTZ BODY
LOWER PORTION OF BODY PARTIALLY FLATTENED TO INCREASE COMPRESSIBILITY
TARE WEIGHT HOOKS
LOAD BASKET HOOK
LOWER FRAME MADE OF 1 mm FIBER
ALINEMENT TIP

FIGURE 1.

Our most useful diver is made of fused quartz (vitrified silica) and weighs about 5 g. It displaces about 10 cm^3; hence in water it has a positive buoyancy of about 5 g. It has a very thin wall so it is quite compressible. In practice it is loaded by the object to be measured and enough tare weight to cause it to sink slowly in water at 4 °C. The pressure system, figure 2, is then closed and the water pressure reduced slightly. This causes the diver volume to expand, thereby increasing diver buoyancy. This causes the loaded diver to stop falling and begin to rise.

There is a pressure gradient in the water, due to the gravity field, so that as the diver rises, it moves into a region of lower pressure. This causes additional expansion and an increase in buoyance, so the diver is accelerated upward. Conversely, when the water pressure is increased, the diver body is compressed which results in smaller buoyance. The diver will then sink. As it sinks into a region of higher pressure, additional buoyancy is lost and the diver is accelerated downward. Thus, the gravity pressure gradient in the fluid always accelerates diver motion, and as a result, there is no position of stable equilibrium.

On the other hand, had the diver compressibility been less than that of water, the reverse set of circumstances would have held. Under such conditions, the pressure gradient in the water would always impede the diver motion and a position of stable equilibrium would exist. It is possible to operate a diver system under either condition, but practical considerations such as load range and sensitivity led to our choice of a diver more compressible than water.

Diver motion is observed through a rigidly mounted microscope and a system of windows and mirrors. The optical center of this system is carefully adjusted horizontally, and the horizontal plane within the diver chamber containing the optical center is called the reference plane. Although (as explained above) there is no level of stable equilibrium for the diver in the system, there is a pressure which will result in the loaded diver having a density precisely equal to the density of the water it displaces when the observed upper tip of the diver is in the reference plane. This pressure is called the equilibrium pressure, P_E, and it can be determined by averaging the two pressures which cause the diver to move upward and downward across a vertical range defined by an eyepiece reticle and extending about 0.013 cm above and below the reference plane in equal intervals of time (usually about 30 sec).

When the pressure is very close to P_E, we are justified in assuming that the average velocity, y, of the diver, during its transit of the range, is nearly linear with pressure. Thus, when the average rising velocity, y_R, does not precisely equal the average falling velocity, y_F, an acceptable value of P_E can be calculated from the formula

$$\frac{P_E - P_R}{P_F - P_R} = \frac{-y_R}{y_F - y_R}.$$

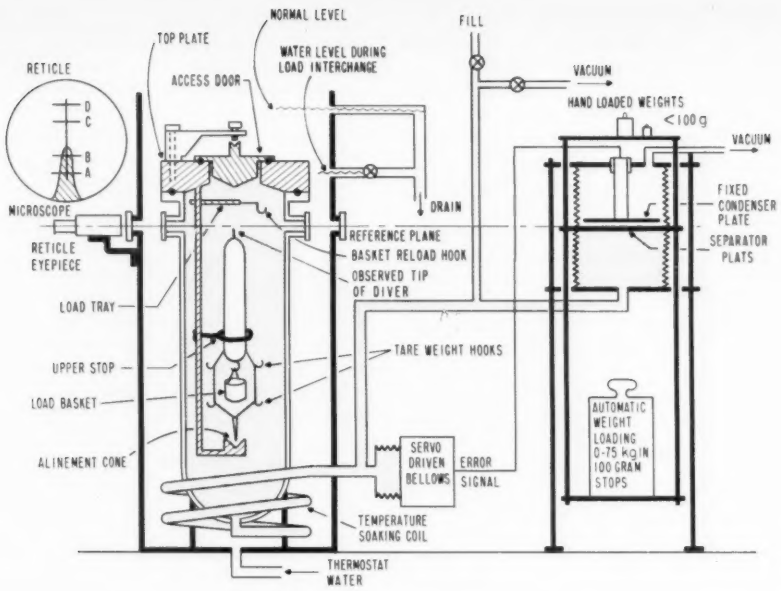

FIGURE 2.

Alternatively, there is a quick graphic solution, which we used, illustrated in figure 3.

3. Pressure System

Our pressure regulator system is a modification of the two-bellows barostat developed by D.P. Johnson [4] for use in the NBS barometer calibration service. It consists of two stainless steel bellows mounted one above the other. The upper bellows is evacuated, and the lower is water-filled and connected to the diver chamber. The upper end of the upper bellows and the lower end of the lower bellows are rigidly attached to the frame. The two bellows are connected mechanically together by a freely floating separator plate. Under such circumstances, the pressure developed in the water in the lower chamber is directly proportional to the deadweight loading of the separator plate. The effective areas of the bellows are such that a 76 kg deadweight load on the separator plate results in about 1-atm pressure being developed in the lower chamber. The loading of the separator plate is conveniently changed in increments of about 100 g, from a minimum of 2 kg (the tare load) to 85 kg, by a semiautomatic loading machine developed by David Sklar, Design Development Laboratories, for the purpose. A small tray on top of the assembly is used to receive additional small hand-loaded weights of between 1 and 100 g (see fig. 2).

The separator plate is electrically connected as the moving plate of a two-plate variable capacitor. The fixed plate is rigidly attached inside of the

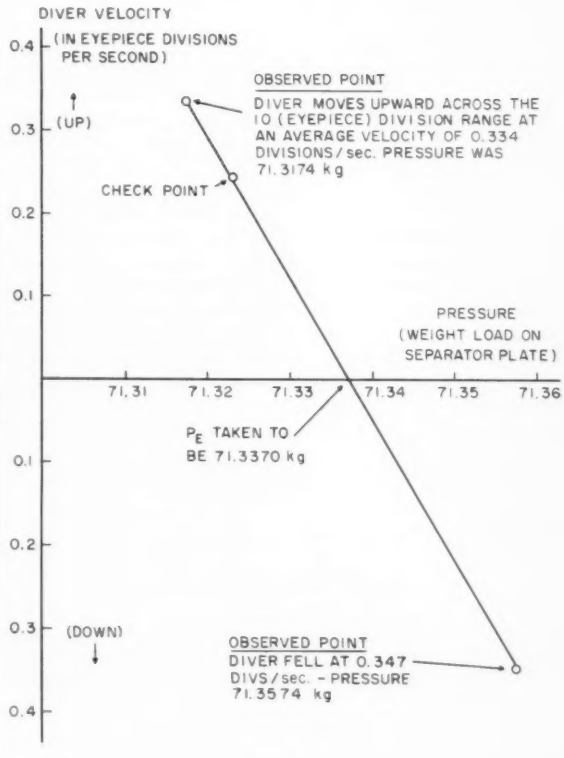

FIGURE 3.

evacuated bellows, about 0.013 cm above the midpoint of the 0.025 cm free travel allowed the separator plate by its stops. The capacitance between the fixed and moving plates is fed into a Wien bridge oscillator and discriminator, which provides servo power to drive a motor-driven bellows connected in the hydraulic system, in such a direction that the separator plate is maintained at the midpoint of its allowed travel, regardless of loading.

With this arrangement the two-bellows assembly is used as an error signal generator and actual pressure changes are made by the servobellows. Inasmuch as the separator plate remains at the same vertical level, regardless of pressure, the effects of the elastic properties of the stainless steel bellows are largely eliminated.

The elastic properties of one of the divers are such that the diver buoyancy changes by 1 μg when the separator plate load is changed by 12 g. Inasmuch as diver buoyancy on differences is constant to about 2/10 μg, it can be inferred that the short term stability of drift of the pressure regulator is about 2×10^{-5} atm/hr. This is consistent with other estimates of stability of similar devices [5].

As use of the diver system does not require absolute knowledge of pressure, no effort has been made to calibrate the system in absolute terms. In use, pressures developed are stated in terms of the kilogram load on the separator plate, which is acceptably linear with water pressure.

4. Use of the Diver—Density Measurements

If G_1 is the mass of water displaced by the Cartesian diver body at some pressure, then

$$G_1=\rho_1 v_1$$

where ρ_1 is the density of water at that pressure, and v_1 the associated diver volume. Both ρ_1 and v_1 are functions of pressure, and G will increase or decrease with increasing pressure depending upon whether the compressibility of water is greater than or less than that of the diver body. ΔG is not a perfectly linear function of ΔP. We have carefully measured the nonlinear term and found

$$\frac{\Delta' G}{\Delta P'}=8\times10^{-8}\text{ g/cm Hg/cm Hg.}^{2}$$

Integrating twice gives us

$$G=(4\times10^{-8})P^2+C_1P+C_2$$

where C_1 and C_2 are the constants of integration introduced thereby. This term adequately represents the mass of water displaced by the diver as a function of pressure.

[2] Although, as previously stated, the pressure system has not been calibrated in absolute terms, within 1 percent, a load change of 1 kg on the separator plate results in a pressure change of 1 cm Hg.

The experiment consists of loading the diver, first with two standards, S1 and S2, and noting the equilibrium pressures, P_{S1} and P_{S2} associated with each. Following this, the unknown object, X, is placed on the diver and P_x observed. The masses, M_{S1} and M_{S2}, and the volumes, V_{S1} and V_{S2}, of the two standards are assumed known. The equilibrium equation of the diver is

$$M_D-G+M_L-\rho_W V_L=0$$

where M_D is the diver mass, M_L and V_L the mass and volume, respectively, of the load and ρ_W the density of water at the equilibrium pressure. As pointed out in the introduction $M_L-\rho_W V_L$ is the apparent mass of the load in water, B_L. For each of the three loads placed on the diver during the experiment, we may write an equilibrium equation

$$\text{(A)}\qquad M_D-(4\times10^{-8})P_{S1}^2-C_1P_{S1}-C_2+B_{S1}=0$$

$$\text{(B)}\qquad M_D-(4\times10^{-8})P_{S2}^2-C_1P_{S2}-C_2+B_{S2}=0$$

$$\text{(C)}\qquad M_D-(4\times10^{-8})P_X^2-C_1P_X-C_2+B_X=0$$

subtracting the second equilibrium equation from the first, and then the third from the first gives us two difference equations

$$-(4\times10^{-8})(P_{S1}^2-P_{S2}^2)-C_1(P_{S1}-P_{S2})+(B_{S1}-B_{S2})=0$$

$$-(4\times10^{-8})(P_{S1}^2-P_X^2)-C_1(P_{S1}-P_X)+(B_{S1}-B_X)=0.$$

The first difference equation may be immediately solved for a numerical value of C_1

$$C_1=\frac{(B_{S1}-B_{S2})-4\times10^{-8}(P_{S1}^2-P_{S2}^2)}{(P_{S1}-P_{S2})}$$

and with this value of C_1 inserted in the second difference equation, we may solve for the apparent mass of the unknown in water, B_X.

$$B_X=B_{S1}-4\times10^{-8}(P_{S1}^2-P_X^2)-C_1(P_{S1}-P_X).$$

This experiment demands a minimum of three observations—P_{S1}, P_{S2}, and P_X. Our system has drift associated with electronic drift, drift in ambient conditions and (probably) other sources. In order to minimize the effect of this drift we use one of our loads as a drift monitor. This load is observed every second observation. For an experiment with only one unknown the observation format would contain five observations taken at uniform intervals, thus: P_{S1}—P_{S2}—P_{S1}—P_X—P_{S1}. The value of $(P_{S1}-P_{S2})$, required in the calculations shown above is obtained by subtracting the observed value of P_{S2} from the average of the first two P_{S1}'s. $(P_{S1}-P_X)$ is obtained in a similar manner. The three observed values of P_{S1} are averaged to give the effective value of P_{S1} during the experiment. Effective values of P_{S2} and P_X used in calculations of C_1 and B_{X1} are obtained by applying the difference terms to this effective value.

The values of water density used in the calculation of apparent mass in water of the standards (from assigned values of mass and volume) are based upon an assumed density of 0.999973 g/cm³ at 4 °C and at 1 atm, and corrected for departure from 1 atm of the effective values of observed pressure. Errors in the assumed value of water density exert only a second-order effect on the calculated density of the unknown, because our density knowledge is primarily obtained from the density standards used in the experiments. The water is merely the comparison medium.

The diver system is currently being used in several density studies not pertinent to this report. To illustrate typical diver operation, some data from these studies will be presented here. Table 1 shows the observed raw data taken during measurements on two imperfect silicon crystals, X1 and X2. The standards used in this experiment were two perfect silicon crystals, S1 and S2, whose assigned density value was 2.3290040 g/cm³. The observed values of P_E and the pressure differences were calculated from values of rising and falling pressures and velocities as previously explained. This table shows data taken during four independent experiments performed during January 1965, and the average value of a group of nonindependent similar experiments performed on the same crystals during the previous November. Between each experiment all crystals were removed from the hydrostatic system and dried and recleaned.

TABLE 1

	Falling		Rising		Observed P_E	$P_{S1}-P_{X1}$	$P_{S1}-P_{X2}$	$P_{S1}-P_{S2}$
	Pressure	Velocity	Pressure	Velocity				
S1	66.8010	0.2183	66.7310	0.1529	66.7600			
X1	64.2264	.1779	64.1564	.1975	64.1932	+2.5699		
S1	66.8010	.1922	66.7310	.1902	66.7662			
X2	65.0809	.1678	65.0109	.2092	65.0495		+1.7221	
S1	66.8110	.1833	66.7410	.1952	66.7770			
S2	64.1246	.1772	64.0546	.1803	64.0923			+2.6829
S1	66.8110	.2024	66.7410	.1729	66.7735			
S1	66.8210	.1799	66.7510	.1960	66.7874			
X1	64.2459	.1492	64.1859	.1723	64.2177	2.5673		
S1	66.8210	.2024	66.7510	.1678	66.7825			
X2	65.1009	.1766	65.0309	.1909	65.0675		1.7213	
S1	66.8303	.1872	66.7600	.1882	66.7950			
S2	64.1464	.1818	64.0764	.1973	64.1114			2.6771
S1	66.8210	.2155	66.7410	.2222	66.7820			
S1	66.9500	.2059	66.8700	.2198	66.9110			
X1	64.3851	.1792	64.3151	.1981	64.3522	2.5554		
S1	66.9400	.1912	66.8700	.1816	66.9042			
X2	65.2201	.1728	65.1501	.2015	65.1882		1.7176	
S1	66.9500	.2183	66.8700	.1922	66.9075			
S2	64.2859	.2309	64.2159	.1165	64.2395			2.6717
S1	66.9500	.1930	66.8800	.1938	66.9150			
S1	66.9792	.1961	66.9092	.1732	66.9425			
S2	64.3159	.1880	64.2459	.2020	64.2825			2.6588
S1	66.9792	.2079	66.8992	.2160	66.9401			
X2	65.2797	.2326	65.2097	.1437	65.2365		1.7065	
S1	66.9792	.1859	66.9092	.2000	66.9458			
X1	64.4259	.1552	64.3559	.2174	64.3970	2.5456		
S1	66.9792	.2150	66.8992	.2104	66.9395			
Average of points taken in November (second silicon)						2.5745	1.7258	2.6858

Table 2 shows the calculated values of effective P_E and the assumed ρ_W associated with these values. The apparent masses in water of the standards is based upon assigned true mass values of $M_{S1}=2.0000912$ g and $M_{S2}=2.0004884$ g. The effective values of C_1 were obtained as previously described and they led to the values of apparent masses in water of the unknown cyrstals.

TABLE 2

		Crystal S1	Crystal S2	Crystal X1	Cyrstal X2
Effective P_E	1	66.7692	64.0863	64.1993	65.0471
	2	66.7868	64.1097	64.2195	65.0655
	3	66.9094	64.2377	64.3540	65.1918
	4	66.9420	64.2832	64.3964	65.2355
	5	67.7366	65.0508	65.1621	66.0108
Assumed ρ_W	1	0.999678	0.9999660	0.999661	0.9999667
	2	678	660	661	667
	3	679	661	662	668
	4	679	662	663	668
	5	684	667	668	673
B of standards	1	1.1413435	1.1415717		
	2	1.1413435	1.1415717		
	3	3435	5716		
	4	3434	5716		
	5	3430	5711		
C_1	1	−0.00009028			
	2	9047			
	3	9062	Same values apply to all four columns.		
	4	9109			
	5	9025			
B of unknowns	1			1.1415619	1.1414900
	2			5623	4902
	3			5617	4901
	4			5620	4900
	5			5616	4896

As pointed out in the introduction, we may obtain values of M_X and V_X from a simultaneous solution of the air weighing and the water weighing equations. Alternatively we may enter the water weighing equation with the value of B_X obtained with the diver and a previously determined M_X and solve for the density of the unknown, ρ_X.

$$\rho_X=\frac{\rho_W}{B_X/M_X-1}$$

where ρ_W is the assumed water density at pressure P_X. Very careful analysis of this point will show that the two methods are nearly identical. The values of ρ_X calculated from the B_X's determined with the diver and $M_{X1}=2.0004774$ g and $M_{X2}=2.0003478$ g were:

	Crystal X1	Crystal X2
6 January	2.3289950	2.3290012
7 January	2.3289958	2.3290018
8 January	2.3289944	2.3290017
9 January	2.3289950	2.3290015
Nov. Avg	2.3289956	2.3290019
Average	2.3289951	2.3290016

Pooled standard deviation $=4.4\times10^{-7}\sim0.22$ ppm.

5. Use of the Diver System—Density Changes

There is widespread scientific interest in the measurement of slight density changes and density differences as well as in the measurement of absolute density itself. The Cartesian diver system is particularly well-suited to determination of changes and differences because of its ability to provide high precision data on samples of small size. In problems such as determination of density differences between nominally identical materials but having slightly different physical properties (such as between hard drawn and annealed wire), or determination of small density changes when a material is exposed to a density-modifying process (such as UV irradiation), homogeneity of the sample is usually of prime importance. Homogeneity can frequently be verified or inhomogeneity evaluated in samples of a few hundred milligrams, but it is frequently impractical or impossible to do so in samples of several grams. Some density modifying processes can provide homogeneous density changes only in small samples, as, for example, processes depending upon x-ray beams that have limited diameters or penetrating powers.

In measuring density changes in an object subjected to a density modifying process, the diver system is largely free of the requirements for high accuracy standards. If the two standards are cut from the same piece of parent material from which the object of interest is cut, and to about the same geometry, then we are justified in assuming that the handbook value of the density of the material applies to the standards absolutely.

The diver was recently called upon to measure the change in density of a single crystal sample of rutile weighing less than 260 mg, when the stoichiometry was altered by thermal reduction. The standards used were cut from adjacent positions in the same boule from which the object of interest was cut. All three crystals were carefully weighed and two independent measurements on the apparent mass in water of the unknown, B_X, were made based on the assumption that the density of the standards was 4.249 g/cm^3.

The crystal of interest was partially reduced as called for in the experimental plan and was then reweighed. Two additional observations were made upon B_X. The data of interest is shown below:

	Before modification		After modification	
Weight of crystal of interest	0.2586061 g		0.2585972 g	
Two measured values of B_X	0.1977429	0.197426	0.1977389	0.1977388
Two calculated values of ρ_X	4.248973	4.248952	4.249169	4.249162
Average ρ_X	4.248962		4.249166	

Change of ρ_X during modification +0.000204

The above data show the agreement in B_x to be about 0.3 μg, which is somewhat poorer than average diver operation. Nevertheless, although the change in density associated with the process under examination amounted to only 5:10^5, the system reported this change to agreement of about 7½ percent.

This experiment was performed upon a crystal of only 250 mg. With larger samples, the reproducibility of B_X would remain about constant, hence the reproducibility of values of density would be much improved.

6. General Comments

Although our work was not primarily directed to evaluation of diver performance as a function of diver characteristics, the following comments may be of interest:

(A) We were never successful in working with Pyrex divers. Although the ones we tried out were always thoroughly annealed after fabrication, we never were able to achieve stability of much better than ± 10 μg.

(B) The sensitivity of the sytem may be crudely defined as $(-)\Delta B/\Delta P_E$, that is the indicated change in apparent mass per unit change in equilibrium pressure. Defined thus, the sensitivity of the diver reported on was about $\frac{1}{12}$ μg/g change in P_E. We experimented upon highly compressible forms in which sensitivity was 10 μg/g, and also upon structures with compressibilities so small that sensitivity approached 0.003 μg/g. We found that the reproducibility decreased as the divers had extremely small or extremely large values of sensitivity. For the extremely sensitive structures we experienced difficulty in obtaining hydrostatic balance, and for the relatively insensitive structures, zero drift was most annoying.

(C) The system is quite sensitive to vibration and the mechanical shock associated with closing doors, etc. Spaepen also reported this vibration sensitivity and described his efforts to minimize it. Our experi-

ment was conducted on a massive pier which had previously been used to support a high sensitivity balance used in the NBS mass calibration program. A vibration survey conducted prior to the experiment indicated that at 30 Hz, the vibrations were about 6×10^{-4}g, decreasing somewhat at night. Our best work was done at night and on weekends.

(D) Many experimenters working with other buoyant devices have reported difficulty in achieving smooth "lift-off" of the buoyant structure from an alining cone at the bottom. We found that a blunt tip at the bottom of the quartz diver moved nicely out of a chromium-plated brass cone whose radius was somewhat greater than the quartz. We experimented with cones of both Pyrex and sapphire with poor results.

(E) In a private communication Spaepen informed us that a newly fabricated diver is rarely stable—that a one or two months aging period is called for. This has also been our experience. We believe that annealing the quartz diver would probably reduce this aging period.

(F) A major uncertainty in all hydrostatic weighing is caused by the adherence of gas to the surfaces of the load. An air bubble large enough to displace 1 μg of water is easily detected visually and easily removed. An equal amount of gas dispersed among several hundred (or thousand?) bubbles would be impossible to detect (without *a priori* knowledge of the density of the material being hydrostatically weighed). This could lead to serious systematic errors in the values of density calculated from observed data. In order to randomize the surface trapped air, we always remove all loads (both standards and unknowns) between each hydrostatic experiment and thoroughly dry and reclean them. A stable volume of gas adhering to the surfaces of the diver body is less annoying, since its chief effect is to change the values of C_1 and G which are determined in each experiment.

(G) In changing diver loads the portion of the tools used which come into contact with the loads are kept continuously immersed in water, never allowing them to come into contact with air. In this way we minimize the likelihood of transferring air from the tools to the loads.

(H) Generally, a perfectly cylindrical diver body will be insufficiently compressible for practical diver operation. Our method of achieving the desired compressibility is to measure $\Delta G/\Delta P$ on a newly constructed diver in its initial cylindrical form. We then partially flatten the cylindrical walls by flame treatment in small increments, measuring $\Delta G/\Delta P$ after each operation. This process is continued until the desired sensitivity is attained. Figure 1 shows this partially flattened section.

The authors take pleasure in acknowledging the generous assistance provided by numerous members of the NBS staff.

Paul Pontius, H. S. Peiser, A. G. McNish, and W. A. Wildhack have provided encouragement, guidance, and support during the entire effort. J. M. Frankland, Dan P. Johnson, J. L. Cross, Harry Matheson, Malcolm Morse, John Pararas, and R. D. Deslattes gave us expert consultation in their special fields.

Enrico Deleonibus devised many special glass-blowing techniques required in the fabrication of the quartz divers. Richard Smith and F. Ferensic performed the intricate machine work required and provided many ideas embodied into the system.

W. S. Brower of the NBS Crystal Chemistry group provided the rutile crystals and E. L. Warrick of the Dow Corning Company furnished the silicon crystals.

The work was performed with partial support of the Advanced Research Projects Agency.

7. References

[1] Chairulli, P. and F. M. Chilton, Investigations on the Cartesian diver balance, (private communication, 1956).

[2] Haller, W. K., and G. L. Calcamuggio, Apparatus for the measurement of extremely small weight, volume, and density changes, Rev. Sci. Instr. **26,** No. 11, p. 1064 (1955).

[3] Spaepen, J., Application of the float method for precision measurement of the density of water and for small samples of solids, Mededel. Koninkl. Vlaam. Akad. Wetenschap. Belg. **19,** No. 5 (1957).

[4] Johnson, D. P., D. Steele, and M. DeNovens, Measurement of drift and recovery in aircraft altimeters, (private communication, 1953).

[5] Brombacher, W. G., D. P. Johnson, and J. L. Cross, Mercury barometers and manometers, NBS Mono. 8 (1960).

(Paper 69C3–202)

JOURNAL OF RESEARCH of the National Bureau of Standards—C. Engineering and Instrumentation
Vol. 69C, No. 3, July–September 1965

Cryogenic Behavior of Selected Magnetic Materials

J. J. Gniewek and E. Ploge*

Institute for Materials Research, National Bureau of Standards, Boulder, Colo.

(April 22, 1965)

Measurements of a-c core loss and d-c magnetic properties including coercive force, residual induction, and hysteresis loss are reported at temperatures of 273, 195, 76, and 4 °K for a variety of commercial magnetic Fe-Si and Fe-48 percent Ni alloys. Of the materials tested the high silicon content (3 to 4.45 percent Si) Fe-Si alloys were found to be the least temperature sensitive. Hysteresis loss increases between 273 and 4 °K of up to 100 percent were measured for the iron-nickel materials.

1. Introduction

An increasing use of electric motors, transformers, and other electrical equipment operating at cryogenic temperatures has created the need for engineering data on the low-temperature magnetic properties of ferromagnetic materials. To fill this need, a-c and d-c magnetic properties were measured at 4, 76, 195, and 273 °K for a variety of commercial Fe-Si and Fe-Ni alloys.

*Present address: Colorado Earth Science Laboratories, Inc., Boulder, Colo.

2. Materials Tested

Tables 1 and 2 list the various Fe-Si and Fe-Ni samples tested together with related pertinent information concerning sheet thickness, type of core, and chemical composition. The identification numbers given will be referred to throughout the text. Materials 110 through 118 were kindly supplied by United States Steel Corporation and materials 100 through 102 and 200 through 213 by Armco Steel Corporation. Materials 100 through 102 are identified by the trade name, "Oriented T," 200 through 203 by "48 Orthonik," and 210 through 213 by "48 Ni."

TABLE 1. *Iron-silicon alloys tested at cryogenic temperatures*

Material AISI Number	Type product	Composition, percent (balance primarily iron)			Grain orientation	Thickness	Type of core	Identification Number
		Si	C	Mn				
						Inches		
Thin grain-oriented nominally 3 percent Fe-Si alloy.		2.78	0.03	0.08	Oriented	0.001	Tape-wound, B*	100
					Oriented	.002	Tape-wound, B	101
					Oriented	.004	Tape-wound, B	102
M-43	HR	1.01	.03	.23	Unoriented	.0250	Laminated—U**	110
M-43	HR	0.85	.05	.35	Unoriented	.0185	Laminated—U, B	111
M-36	CR	1.90	.04	.31	Unoriented	.0250	Laminated—U, B	112
M-27	CR	2.93	.04	.25	Unoriented	.0250	Laminated—U	113
M-27	HR	3.01	.017	.10	Unoriented	.0185	Laminated—U, B	114
M-27	HR	2.93	.04	.37	Unoriented	.0250	Laminated—U	115
M-22	HR	3.13	.03	.11	Unorieuted	.0140	Laminated—U	116
M-19	HR	3.57	.021	.11	Unoriented	.0140	Laminated—U, B	117
M-15	HR	4.45	.043	.14	Unoriented	.0185	Laminated—B	118

*=boxed. **U=unboxed. HR=hot rolled. CR=cold rolled.

TABLE 2. *Iron-nickel alloys tested at cryogenic temperatures*

Nominally 48 percent Ni content.

Material	Grain orientation	Thickness	Type of core	Identification number
		Inches		
FeNi	Oriented	0.002	Tape-wound, B	200
FeNi	Oriented	.004	Tape-wound, B	201
FeNi	Oriented	.006	Tape-wound, B	202
FeNi	Oriented	.006	Laminated, B	203
FeNi	Unoriented	.002	Tape-wound, B	210
FeNi	Unoriented	.004	Tape-wound, B	211
FeNi	Unoriented	.006	Laminated, B	212
FeNi	Unoriented	.014	Laminated, B	213

3. Measuring Technique

3.1. Equipment

A standard voltmeter-wattmeter method [1][1] was used to determine a-c core loss values. The magnetic induction in the core is determined by measuring the secondary voltage with an a-c differential voltmeter calibrated to 0.5 percent accuracy. Induction levels

[1] Figures in brackets indicate the literature references at the end of this paper.

were limited to values below that which resulted in 3 percent or greater 3rd harmonic distortion as determined by a wave analyzer across the secondary windings. A high input impedence electronic wattmeter was employed thereby making instrumental loss corrections negligible. Direct current hysteresis loops were plotted semiautomatically on an x-y chart recorder. The magnetic induction was recorded using an integrating d-c amplifier. The magnetizing force was calculated from the voltage drop produced by the magnetizing current flowing through a standard resistor.

3.2. Samples

The samples used for cryogenic testing weigh approximately ⅛ lb and are considerably smaller than that specified by the ASTM standards [2]. This was necessary to prevent excessive liquid evaporation and the use of inconveniently large Dewars. All samples are in the shape of toroids. The tape-wound and laminated samples vary slightly in size. In all cases, however, the ratio of mean diameter to radial width is 8 to 1 or greater. This ensures a reasonably uniform flux distribution throughout the cross-sectional area of the sample. The mean diameter of the cores is approximately 2 in. For most materials two samples of each were tested.

The oriented iron-silicon material and all iron-nickel samples were placed in either anodized aluminum or bakelite boxes prior to winding the secondary and primary coils. These loose-fitting boxes prevent coil winding stresses from affecting the magnetic properties. Since the unoriented grades of Fe-Si are seldom boxed in normal use, these samples were prepared by wrapping the laminated toroid with 0.004-in. Teflon tape to provide electrical insulation between windings and core material. The primary and secondary windings were then placed directly atop the Teflon tape. To determine the effect of winding stresses on the magnetic properties, four materials, 111, 112, 114, and 117, were also tested in boxed form. The large increase in core loss for the unboxed cores compared to the boxed cores at low temperature can be attributed to the detrimental stress effects produced by the differential contraction between the iron-core material and the copper windings. Because of the wide use of the unoriented grade Fe-Si in components where little or no emphasis is given to eliminating winding or clamping stresses, core loss data for the unboxed as well as selected boxed materials are shown in table 3.

TABLE 3. *Total core loss at 273 °K and the ratio of core loss measured at temperature T to that measured at T=273 °K*

(Core loss value at 273 °K is given in units of watts/pound)

Material	Frequency	Temperature	Peak induction kG								
			2	4	8	10	13	15	16	17	18
	c/s	°K									
100	60	273	0.031	0.12$_9$	0.46	0.73	1.4$_0$				
		195	1.03	1.02	1.02	1.01	1.00				
		76	1.10	1.05	1.04	1.01	1.00				
		4	1.13	1.08	1.07	1.03	1.00				
100	400	273	0.23$_0$	0.91	3.1	5.0	9.4	15.$_1$			
		195	1.02	1.02	1.03	1.02	1.02	1.01			
		76	1.07	1.05	1.06	1.06	1.04	1.02			
		4	1.09	1.08	1.10	1.08	1.06	1.03			
100	1000	273	0.60	2.40	8.7	13.$_3$					
		195	1.03	1.03	1.01	1.02					
		76	1.10	1.08	1.06	1.05					
		4	1.13	1.12	1.08	1.07					
101	60	273	0.017$_8$	0.070	0.23$_9$	0.36	0.64	1.0$_3$			
		195	1.03	1.03	1.04	1.03	1.03	1.03			
		76	1.07	1.06	1.07	1.06	1.06	1.05			
		4	1.09	1.09	1.08	1.06	1.06	1.05			
101	400	273	0.13$_7$	0.54	1.8$_1$	2.9$_1$	5.0	7.8		14.0	
		195	1.06	1.06	1.07	1.03	1.02	1.03		1.00	
		76	1.13	1.13	1.13	1.10	1.06	1.06		1.00	
		4	1.15	1.15	1.15	1.10	1.08	1.09		1.00	
101	1000	273	0.40	1.5$_7$	5.7	8.7					
		195	1.08	1.06	1.07	1.07					
		76	1.15	1.12	1.12	1.11					
		4	1.18	1.13	1.12	1.13					
102	60	273	0.012$_7$	0.046	0.15$_1$	0.22$_0$	0.37	0.53	0.73		
		195	1.02	1.02	1.04	1.04	1.03	1.02	1.01		
		76	1.06	1.04	1.07	1.08	1.08	1.06	1.01		
		4	1.08	1.07	1.09	1.10	1.08	1.08	1.03		
102	400	273	0.12$_8$	0.46	1.6$_1$	2.3$_8$	3.9	5.5	7.1		13.$_7$
		195	1.09	1.09	1.07	1.08	1.08	1.05	1.03		1.01
		76	1.17	1.17	1.16	1.16	1.18	1.09	1.06		1.06
		4	1.20	1.22	1.17	1.18	1.21	1.11	1.08		1.09
102	1000	273	0.46	1.7$_4$	6.2	9.4					
		195	1.07	1.07	1.06	1.06					
		76	1.17	1.16	1.16	1.16					
		4	1.20	1.18	1.19	1.19					

Material	Frequency	Temperature	Peak induction kG						
			2	4	6	8	10	12	14
	c/s	°K							
110 U	60	273	0.099	0.31	0.67	1.1$_0$	1.7$_1$	2.4	3.3
		195	1.34	1.39	1.36	1.35	1.35	1.29	1.27
		76	2.02	2.19	2.13	2.18	2.16	2.13	2.06
		4	2.42	2.65	2.60	2.73	2.63	2.67	2.55
111 U	60	273	0.089	0.28	0.54	0.89	1.4$_0$	1.9$_5$	
		195	1.27	1.25	1.30	1.27	1.24	1.23	
		76	2.10	2.21	2.31	2.25	2.21	2.21	
		4	2.25	2.61	2.78	2.89	2.79	2.82	
111 B	60	273	0.078	0.25	0.50	0.80	1.1$_8$	1.6$_9$	
		195	1.08	1.12	1.10	1.15	1.16	1.15	
		76	1.46	1.64	1.70	1.80	1.78	1.79	
		4	2.18	2.32	2.48	2.63	2.71	2.80	
112 U	60	273	0.083	0.27	0.50	0.84	1.3$_1$	1.8$_1$	
		195	1.22	1.26	1.28	1.21	1.23	1.20	
		76	1.47	1.48	1.56	1.51	1.51	1.48	
		4	1.69	1.67	1.78	1.81	1.76	1.80	
113 U	60	273	0.083	0.25	0.50	0.82	1.27	1.80	
		195	1.17	1.20	1.16	1.16	1.14	1.17	
		76	1.36	1.40	1.36	1.33	1.31	1.28	
		4	1.41	1.44	1.38	1.39	1.39	1.39	
114 U	60	273	0.064	0.21	0.39	0.66	1.03	1.50	
		195	1.16	1.19	1.26	1.18	1.15	1.13	
		76	1.30	1.33	1.38	1.32	1.27	1.23	
		4	1.36	1.38	1.44	1.36	1.29	1.26	
114 B	60	273	0.056	0.195	0.39	0.64	0.96		
		195	1.04	1.03	1.03	1.03	1.03		
		76	1.11	1.08	1.08	1.08	1.08		
		4	1.11	1.08	1.10	1.09	1.08		
114 B	400	273	0.69	2.5	5.3	9.2	14.$_0$	20.$_0$	
		195	1.04	1.04	1.04	1.02	1.03	1.05	
		76	1.14	1.12	1.13	1.12	1.16	1.15	
		4	1.16	1.16	1.15	1.13	1.16	1.19	
115 U	60	273	0.072	0.24	0.47	0.77	1.1$_7$	1.6$_9$	
		195	1.15	1.17	1.17	1.14	1.14	1.13	
		76	1.40	1.42	1.43	1.38	1.38	1.36	
		4	1.53	1.50	1.49	1.51	1.49	1.42	
116 U	60	273	0.053	0.17$_5$	0.34	0.55	0.83	1.1$_8$	
		195	1.26	1.26	1.29	1.27	1.23	1.19	
		76	1.43	1.37	1.41	1.36	1.27	1.30	
		4	1.45	1.43	1.41	1.36	1.27	1.30	
117 U	60	273	0.048	0.15$_2$	0.30	0.48	0.74	1.0$_3$	
		195	1.23	1.21	1.23	1.21	1.19	1.17	
		76	1.31	1.32	1.33	1.33	1.31	1.30	
117 B	60	273	0.036	0.12$_0$	0.23	0.38	0.56	0.80	
		195	1.06	1.03	1.04	1.03	1.04	1.04	
		76	1.14	1.10	1.13	1.08	1.09	1.08	
		4	1.17	1.13	1.13	1.08	1.11	1.09	
117 B	400	273	0.42	1.4$_3$	2.8	4.7	7.3	10.$_6$	
		195	1.05	1.05	1.07	1.04	1.04	1.04	
		76	1.12	1.10	1.14	1.11	1.10	1.10	
		4	1.14	1.13	1.14	1.13	1.12	1.11	
118 B (As processed; not annealed).	60	273	0.039	0.15$_2$	0.31	0.51	0.76	1.0$_1$	
		195	.97	.99	.97	.98	.99	1.01	
		76	.95	.97	.97	.96	.97	1.02	
		4	.95	.96	.97	.96	.96	1.03	
118 B (As processed; not annealed).	400	273	0.48	1.8$_0$	3.9	6.0	11.$_0$	16.$_3$	25.$_0$
		195	1.00	1.00	1.00	1.00	1.00	1.01	1.04
		76	1.00	1.00	1.00	1.00	1.00	1.02	1.04
		4	1.00	1.00	1.00	1.00	1.00	1.03	1.08
118 B (Annealed).	60	273	0.035	0.11$_6$	0.22$_9$	0.35	0.52	0.75	
		195	1.00	1.00	1.00	1.00	1.00	1.00	
		76	1.00	1.00	1.00	1.00	1.00	1.00	
		4	1.00	1.00	1.00	1.00	1.00	1.00	
118 B (Annealed).	400	273	0.49	1.8$_0$	3.8	5.8	10.$_1$	14.$_3$	20.$_7$
		195	1.00	1.00	1.00	1.00	1.00	1.03	1.04
		76	1.00	1.00	1.00	1.00	1.00	1.06	1.09
212	60	273	0.0072	0.025		0.084	0.13$_5$	0.21$_5$	
		195	1.39	1.36		1.33	1.29	1.27	
		76	1.83	1.88		1.80	1.71	1.63	
		4	1.86	1.92		1.92	1.84	1.67	
212	400	273	0.11$_2$	0.39		1.3$_8$	2.0$_7$	3.1	4.6
		195	1.29	1.28		1.26	1.30	1.26	1.24
		76	1.70	1.72		1.67	1.69	1.61	1.59
		4	1.85	1.87		1.83	1.84	1.81	1.74
213	60	273	0.010$_8$	0.038		0.13$_8$	0.22$_4$	0.33	
		195	1.28	1.21		1.22	1.21	1.30	
		76	1.69	1.74		1.70	1.70	1.76	
		4	1.93	1.95		1.96	1.88	1.91	
213	400	273	0.21$_1$	0.78		3.5	6.2	9.2	12.$_3$
		195	1.23	1.21		1.20	1.24	1.29	1.38
		76	1.75	1.69		1.71	1.66	1.76	1.91
		4	1.94	1.90		1.91	1.85	1.99	2.11

With the exception of sample 118 all materials were stress-relief annealed by the fabricators following their normal annealing procedures. Sample 118 was tested in both unannealed, as fabricated, and annealed conditions. Both unannealed and annealed samples were boxed to prevent the extraneous effects of winding stresses. The temperature behavior of these two samples will be discussed later in relation to theories of coercive force.

Internal heating was, in some instances, great enough to raise the sample temperature above that of the environmental bath. The temperature rise was determined using a Au-Co versus copper thermocouple. Core loss values presented in table 3 have been interpolated where necessary to give loss values at the bath temperatures listed.

4. Alternating Current Loss Data

Alternating current core loss for each sample was measured at 4, 76, 195, and 273 °K for various peak inductions from 2 to 18 kg.[2] All materials were tested at 60 c/s (hertz). Where the type of material warranted it, measurements were also made at 400 and 1000 c/s. At 60 c/s the upper induction level is limited by waveform distortion. At 1000 c/s it is limited by the breakdown voltage of the magnet wire insulation. In the interest of saving space, only four graphs (figs. 1–4) showing core loss versus temperature are presented. The bulk of the data are presented in table 3.

From the data given in figures 1 to 4 and table 3 it is noted that the high silicon content (3 to 4.45% Si) Fe-Si alloys are the least sensitive to temperature variations. This is primarily a result of these alloys having a lesser temperature dependence of electrical resistivity resulting in a smaller increase in eddy current loss. Although there has been some criticism in the past of separating total core loss into hysteresis loss and eddy current loss components, we find that it is helpful, at least qualitatively, to speak in terms of a separate hysteresis and eddy current loss.

[2] The following relationships may be used to obtain equivalent values in the MKSA system of units.

1 kilogauss = 0.1 tesla
1 oersted = 79.58 ampere turns/meter
1 watt/pound = 2.204 watt/kilogram
1 inch = 0.02540 meter

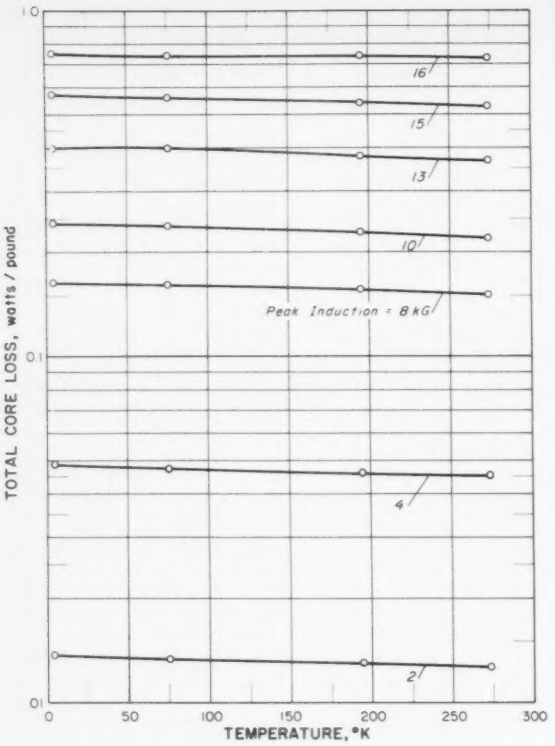

FIGURE 1. *Total core loss at 60 c/s for various peak inductions: Material 102.*

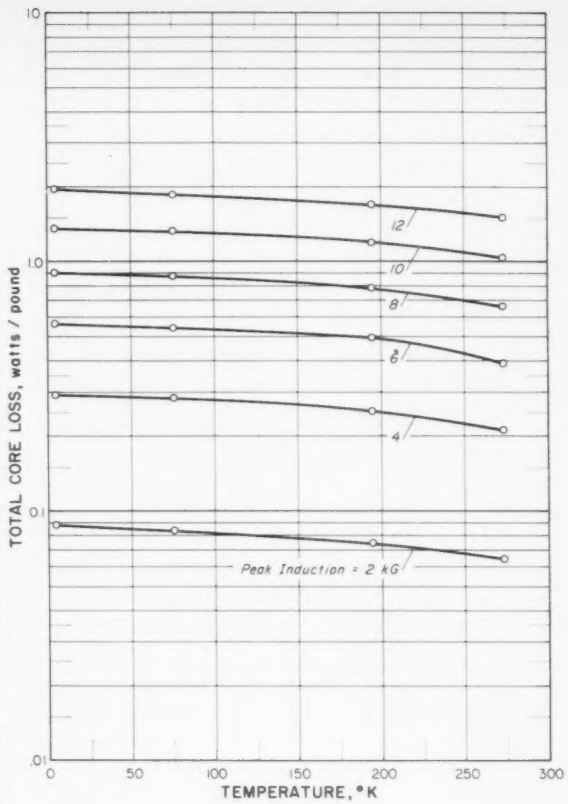

FIGURE 2. *Total core loss at 60 c/s for various peak inductions: Material 114 unboxed.*

For instance, upon examining the data for material 102 in table 3, it is noted that at 60 c/s and for low peak inductions there is a loss increase of approximately 8 percent upon cooling from 273 to 4 °K. At 400 c/s and 1000 c/s however, the corresponding loss increase is approximately 20 percent. This difference may be explained by assuming the greater part of the total loss at 60 c/s to be due to a hysteresis loss while at 400 and 1000 c/s an increasing percentage of the total loss is due to eddy current losses which, to a first approximation, may be expected to vary inversely as the material resistivity. From the resistance data given in figure 5 it is seen that for material 102, $R_4/R_{273}=0.82$. This gives an expected eddy current loss increase of approximately 22 percent which is in good agreement with the total core loss data at 1000 c/s. By similar arguments involving separate hysteresis and eddy current loss components a satisfactory comparison of the temperature dependence of core loss can be made among materials 100, 101, and 102 which are similar except for tape thickness.

As a result of this study it may be said that, in general, a-c core loss will increase upon cooling from 273 to 4 °K. The amount of increase varies greatly from one material to another, the range being from nearly no increase to almost 200 percent for the materials tested. The one exception to the above statement is material 118. As seen in table 3 this sample, in the unannealed condition, showed a loss decrease of approximately 4 percent at 60 c/s. This decrease with decreasing temperatures is also evident in the d-c hysteresis loss measurements and will be discussed further in the section on d-c properties.

5. Direct Current Properties

Direct current hysteresis loops at peak inductions of 5, 10, and 15 kG were measured for the same samples used for a-c measurements. Values of the coercive force, H_c, and the ratio of residual induction to peak induction, B_r/B_m, were measured directly from the loops and should be accurate to within approximately 1 percent. The d-c hysteresis loss, P_h, was determined from planimeter measurements of the loop area and should be accurate to about 1 to 2 percent except for induction levels which required a change of scale in the

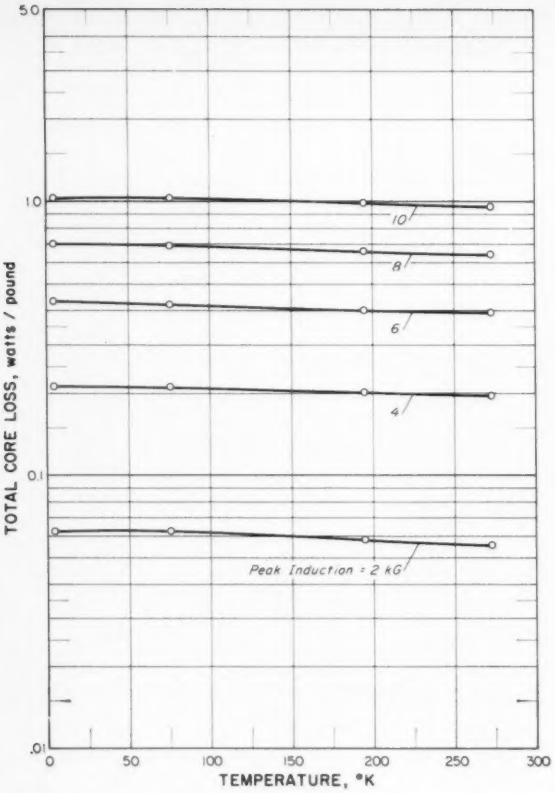

FIGURE 3. *Total core loss at 60 c/s for various peak inductions: Material 114 boxed.*

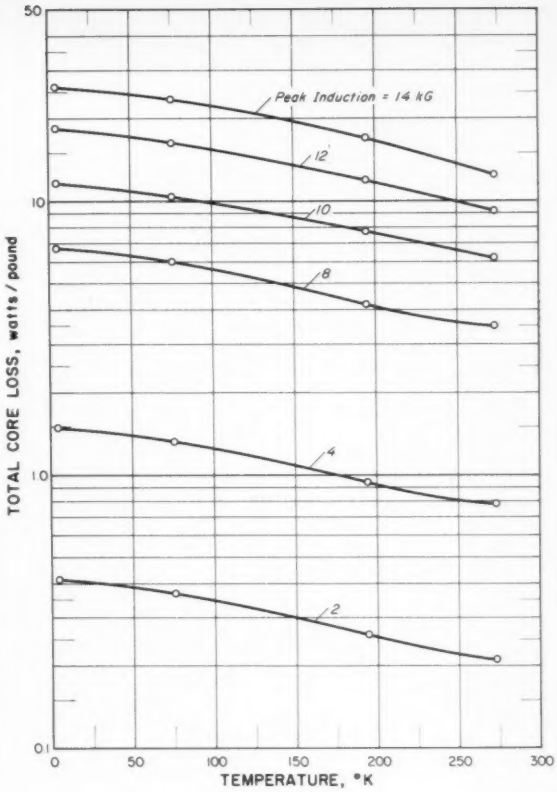

FIGURE 4. *Total core loss at 400 c/s for various peak inductions: Material 213.*

H-axis. In the latter cases the loss values may be in error up to approximately 5 percent.

Inasmuch as the winding stresses are known to influence the hysteresis loss temperature dependence, only the boxed samples will be considered here. The effects observed are therefore of purely magnetic origin. The results for the Fe-Si and Fe-Ni alloys are presented separately.

5.1. Fe-Si Alloys

The temperature dependence of the coercive force, residual induction, and hysteresis loss is shown graphically in figures 6 through 10 with the results normalized to 1.00 at 273 °K. For comparison purposes the absolute values of H_c, B_r/B_m, and P_h at 273 °K are tabulated in table 4.

TABLE 4. *Coercive force* (H_c), *ratio of residual induction to peak induction* (B_r/B_m), *and hysteresis loss* (P_h) *at 273 °K*

Sample	5 kG			10 kG			15 kG		
	H_c	B_r/B_m	P_h	H_c	B_r/B_m	P_h	H_c	B_r/B_m	P_h
	Oe		*erg/cm³/cycle*	*Oe*		*erg/cm³/cycle*	*Oe*		*erg/cm³/cycle*
100	0.442	0.652	537	0.670	0.843	1956	0.952	0.880	5871
101	.241	.660	290	.345	.844	981	.470	.909	2534
102	.136	.634	163	.187	.810	507	.234	.958	1148
111	.482	.820	661	.610	.892	1937	.719	.885	5991
112	.388	.811	541	.485	.865	1603	.582	.838	4161
114	.471	.743	621	.630	.822	2053	.735	.744	6716
117	.279	.783	386	.368	.872	1163	.426	.802	3284
118 unannealed	.423	.624	517	.563	.672	1664	.632	.564	4517
118 annealed	.231	.512	281	.303	.396	821	.325	.291	----

773-721—65——5

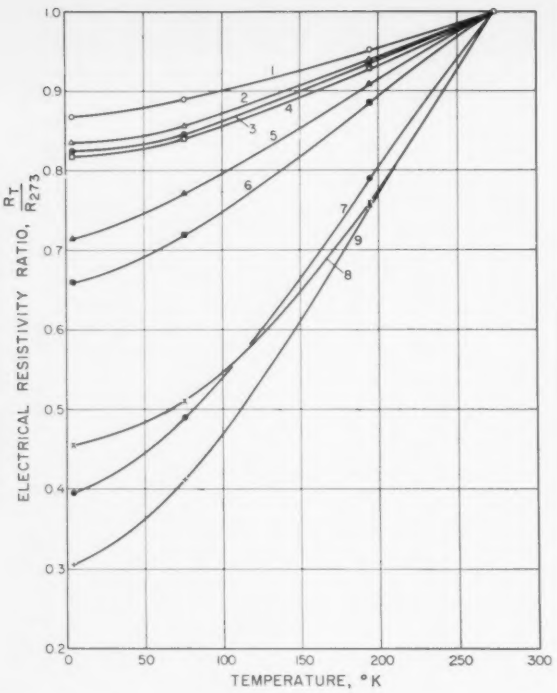

FIGURE 5. *Electrical resistances, ratios of low temperature to ice-point values.*

The numbered curves are for the following materials listed in tables 1 and 2: (1) 118; (2) 117; (3) 116; (4) 113 and 109, 101, 102; (5) 114; (6) 112; (7) 110; (8) 200 series; (9) 111.

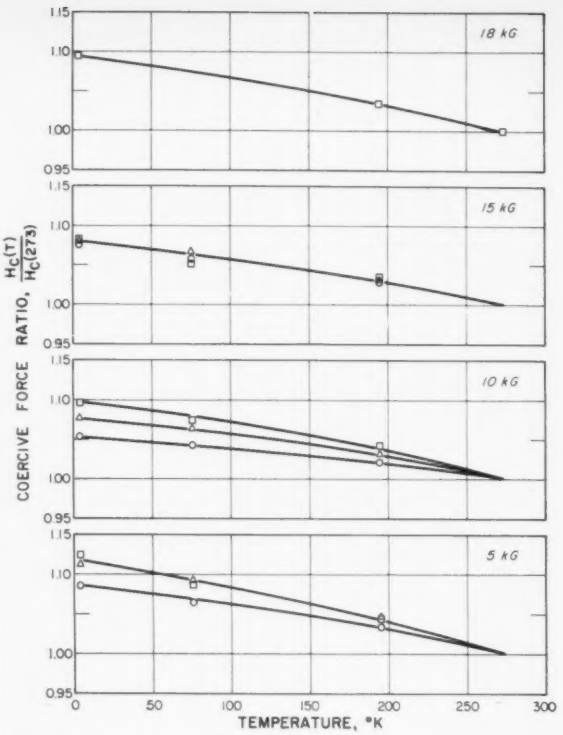

FIGURE 6. *Coercive force, ratio of low temperature to ice-point values.*

Grain-oriented material: ○ 100; △ 101; □ 102. Materials identified in table 1.

a. Hysteresis Loss

The magnetization process in ferromagnets is commonly described in terms of domain wall motion and domain rotation processes. By measuring the d-c hysteresis loops at peak inductions of 5, 10, and 15 kG it was intended to proceed from an induction level (5 kG) where comparatively simple domain wall motion processes predominate to an induction level (15 kG) where domain rotations and the more complex closure domains [3] become increasingly important. It is of course realized that this somewhat arbitrary choice of peak induction levels will distinguish between the different magnetization processes to varying degrees for the various materials tested. To illustrate this it would be well to consider materials 100 and 102. The hysteresis loops at a peak induction of 15 kG are shown for these two materials in figures 11 and 12, respectively. It is evident from the loops that the magnetization of material 102 has proceeded primarily by simple domain wall motion. On the other hand, the curve for material 100 suggests that the magnetization process is well into the region of domain rotations and the associated closure domain wall movements. This influence of magnetization process on the temperature dependence of the hysteresis loss is shown in figure 7. Here it is noted that at 15 kG, material 100 exhibits a temperature independent hysteresis loss. This corresponds to Chen's statement [3] that at the higher temperatures the decrease in energy loss associated with irreversible domain wall movement may be completely compensated by an increase in closure domain loss. At 15 kG material 102 still shows an increased hysteresis loss at 4 °K. The increase, however, is only about 5 percent compared to 10 percent at 10 kG and approximately 13 percent at 5 kG. Thus it indicates that the magnetization of material 102 is just starting to enter the region of domain rotation at 15 kG. It would be expected that at some higher peak induction material 102 would exhibit a temperature behavior comparable to the behavior of material 100 at 15 kG. This in fact is the case at 18 kG where the hysteresis loss for material 102 was measured to be approximately 2 percent lower at 4 °K compared to the 273 °K value. Ignoring material 118 for the moment it is found that a similar situation exists for the unoriented alloys as shown in figure 9. While there is a hysteresis loss increase of approximately 4 percent at 76 °K for both 5 and 10 kG the hysteresis loss decreases by approximately 2 percent for a peak induction of 15 kG.

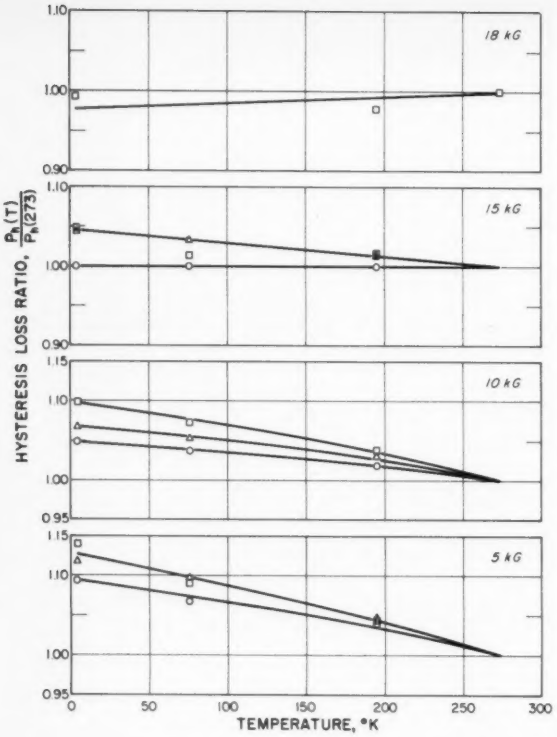

FIGURE 7. *Hysteresis loss, ratio of low temperature to ice-point values.*

Grain-oriented material: ○ 100; △ 101; □ 102. Materials identified in table 1.

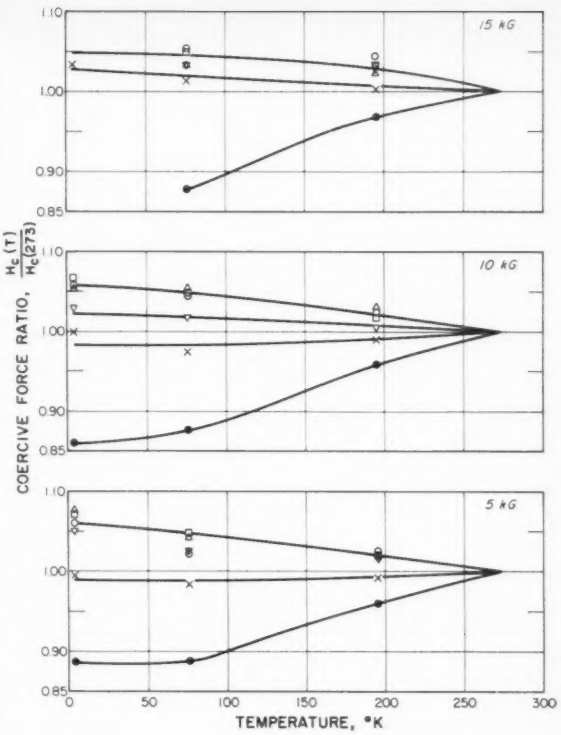

FIGURE 8. *Coercive force, ratio of low temperature to ice-point values.*

Boxed unoriented material: ○ 111; △ 112; □ 114; ▽ 117, ● 118, unannealed: × 118 annealed. Materials identified in table 1.

b. Coercive Force

Upon comparison of the curves for the temperature dependence of coercive force and hysteresis loss it is found for materials 100–102 that for peak inductions of 5 and 10 kG the temperature behavior is nearly identical. Thus the hysteresis loss behavior is determined almost entirely by the temperature dependence of the coercive force. At 15 kG (18 kG for material 102), there is no such correspondence. This is due to the effect of closure domain loss as discussed previously. It should be observed, however, that the increase in coercive force at 4 °K is very nearly the same for both the 10 and 15 kG levels of induction.

c. Residual Induction

As discussed by Chen the residual induction may be expected to increase with decreasing temperature. The primary reason for this is the temperature dependence of the magnetocrystalline anisotropy, K, in the expression for the wall energy. Inasmuch as this model is concerned with the nucleation of new reverse domains, the expression for wall energy would be expected to give an indication of the temperature dependence of the residual induction only at induction levels approaching saturation where all the original domain walls have been eliminated. Indeed, for the samples shown in figure 10, with the exception of 118, the residual induction is essentially temperature independent at the lower peak inductions of 5 and 10 kG.

d. Material 118

As can be seen from the curves for H_c, B_r, and P_h, material 118 exhibits a behavior different from the other iron-silicon alloys tested. For this reason it is presented separately. We have no complete explanation for the temperature behavior of this material but feel it is probably associated with the vanishing magnetostriction constant at low temperatures for a silicon content of 4.45 percent [4].

As discussed by Chen the current theories indicate the coercive force to be a function of λ_s/I_s or K/I_s or both, where λ_s is the magnetostriction constant, I_s is the saturation magnetization, and K is the magnetocrystalline anisotropy. Whereas Chen considered the energy term associated with magnetostriction to be negligible compared to the crystal anisotropy term, this is not the case for 4.45 percent silicon iron. In the case of the unannealed, "as processed" sample, the material is undoubtedly severely stressed.

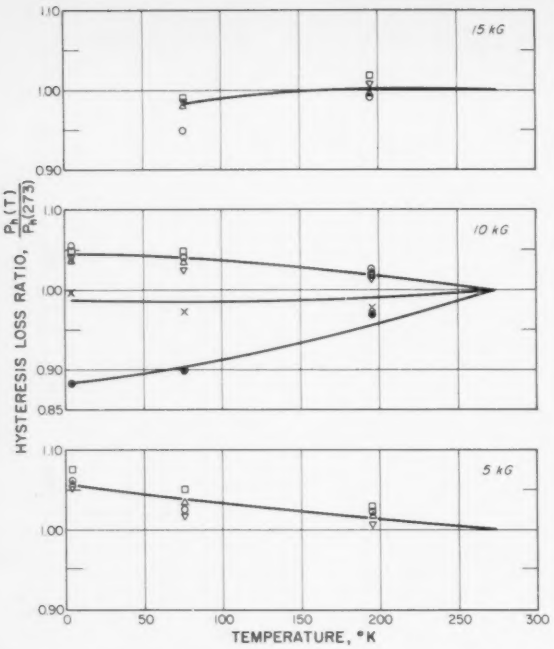

FIGURE 9. *Hysteresis loss, ratio of low temperature to ice-point values.*

Boxed unoriented material: ○ 111: △ 112: □ 114: ▽ 117: ● 118 unannealed; × 118 annealed. Materials identified in table 1.

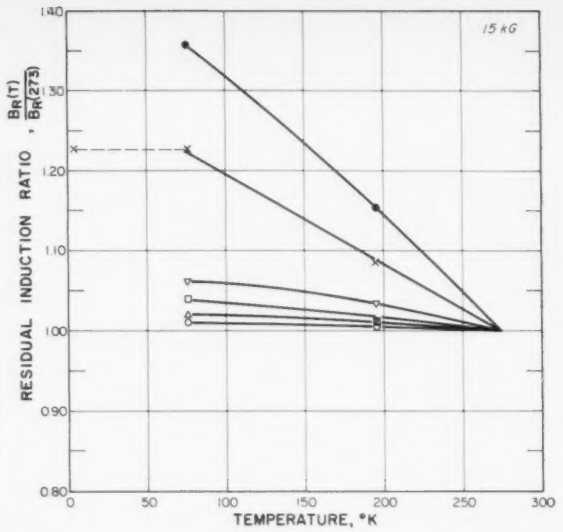

FIGURE 10. *Residual induction, ratio of low temperature to ice-point value.*

Boxed unoriented material: ○ 111; △ 112; □ 114; ▽ 117; ● 118 unannealed; × 118 annealed. Materials identified in table 1.

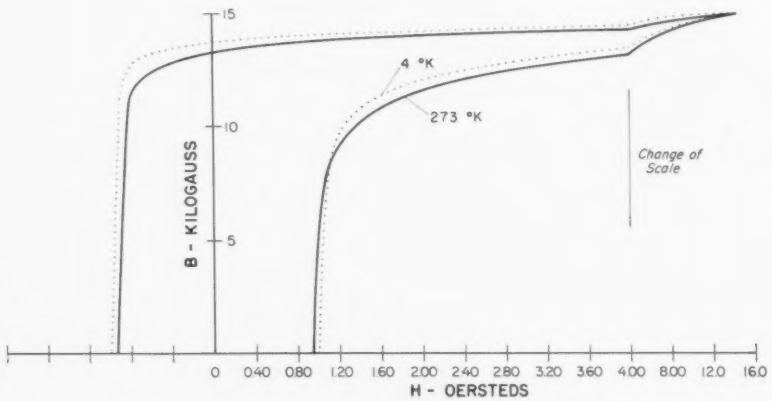

FIGURE 11. *Hysteresis loop at a peak induction of 15 kG.*

Material 100.

Taking the internal stress to be of the order of the yield stress (4.9×10^9 dyn/cm^2) and $\lambda_{100}=2.0\times10^{-5}$, the energy associated with magnetostriction is 9.8×10^4 ergs/cm^3 compared to a crystal anisotropy energy of 30×10^4 ergs/cm^3 at room temperature. Clearly the magnetostriction energy is not negligible. The decrease in H_c shown in figure 8 is thus attributed to the decrease in the magnetostriction constant upon cooling below 273 °K.

If this interpretation is correct the removal of internal stresses by annealing would be expected to result in a temperature dependence of coercive force

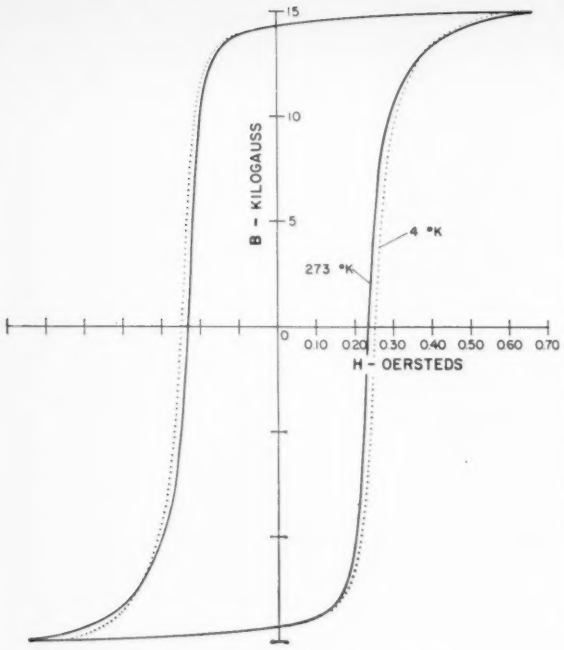

FIGURE 12. *Hysteresis loop at a peak induction of 15 kG.*
Material 102.

determined by the crystal anisotropy energy only. As shown for the annealed sample this result was partially realized; the coercive force at 15 kG increased slightly with decreasing temperature. It should be noted that the coercive force at 5 kG and 10 kG still shows a small decrease at the lower temperatures. The decrease is, however, much less than for the unannealed sample. It is possible that annealing the material at 1425 °F for 24 hr does not completely remove the internal stresses, thus leaving a small dependence on the magnetostriction energy. Annealing at higher temperatures was not attempted since it was feared that recrystallization might occur thereby introducing a new variable of crystal orientation [5].

The behavior of the residual induction for both the unannealed and annealed material is shown in figure 10. The unannealed sample shows a greater temperature dependence than the annealed material. For a material whose magnetostriction decreases with decreasing temperature this would not be expected to occur on the basis of the wall energy equation mentioned previously. Barring the possibility of recrystallization occurring during the annealing treatment one must conclude that it is an oversimplification to treat the residual induction in terms of the wall nucleation process only.

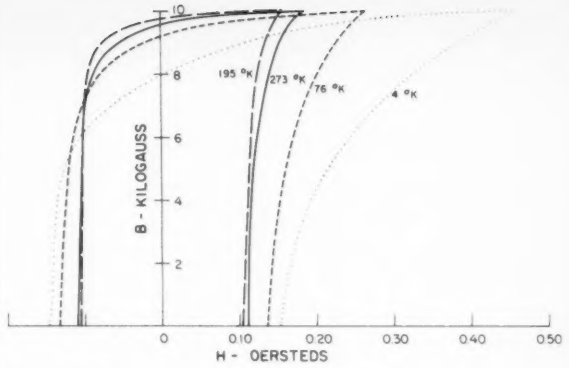

FIGURE 13. *Hysteresis loops.*
Material 200.

5.2. Fe-Ni Alloys

The iron-nickel alloys tested are less well-behaved than the iron-silicon alloys discussed in the previous section. Their behavior is not completely understood at present. In view of their potential use at cryogenic temperatures however, and the large changes in the magnetic properties which were found to occur, some results are presented here without explanation. The curves are intended primarily for design and application use.

Hysteresis loops for a variety of materials are presented in figures 13 through 20. The curves shown in figure 17 are for a material commercially supplied as 0.002 in. 48 Ni. However, metallurgical investigation indicated a very small grain size which is not considered to be typical for this material. The curves are presented in view of the strange behavior evident at 76 °K. It is not known whether such a temperature behavior would be the rule or the exception for commercially supplied material of this type. A laboratory prepared sample, of 0.002 in. 48 Ni, supplied by Armco Steel, was also tested. The results are shown in figure 18 where it is seen that the kinked loop behavior is absent.

6. Summary

The a-c and d-c magnetic properties of selected Fe-Si and Fe-Ni alloys have been measured at cryogenic temperatures. The results are presented in tables and graphs to provide engineering design data. Of the Fe-Si alloys, the thin grain-oriented material would be best suited for cryogenic use. In addition to its superior room temperature properties, it exhibits a considerably lower loss increase at cryogenic temperatures than do the thicker laminated, low silicon content alloys. The Fe-Ni alloys are in

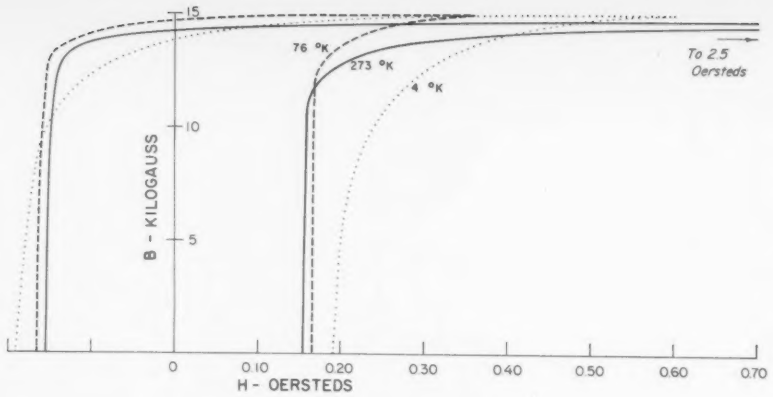

FIGURE 14. *Hysteresis loops.*
Material 201.

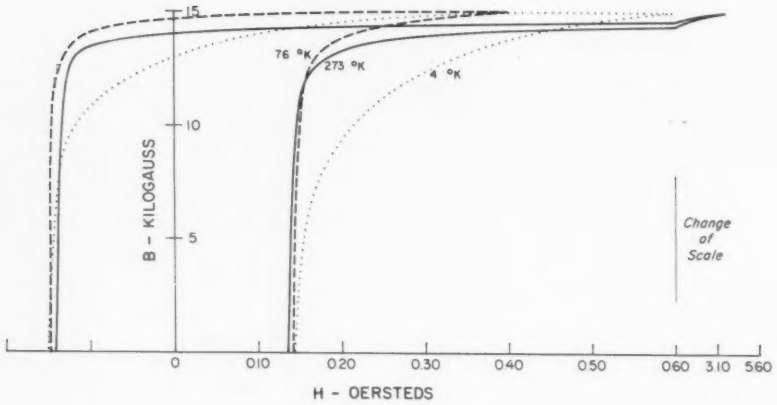

FIGURE 15. *Hysteresis loops.*
Material 202.

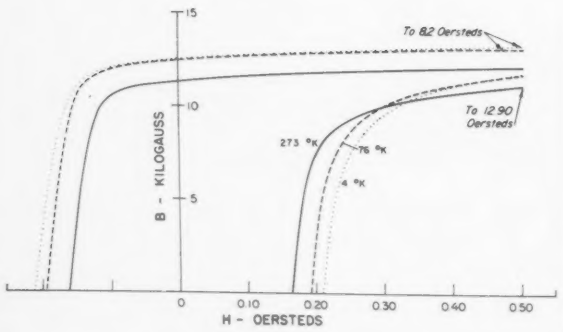

FIGURE 16. *Hysteresis loops.*
Material 203.

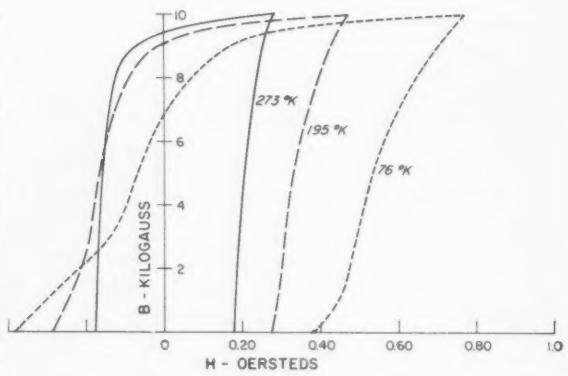

FIGURE 17. *Hysteresis loops.*
Material 210; commercial preparation.

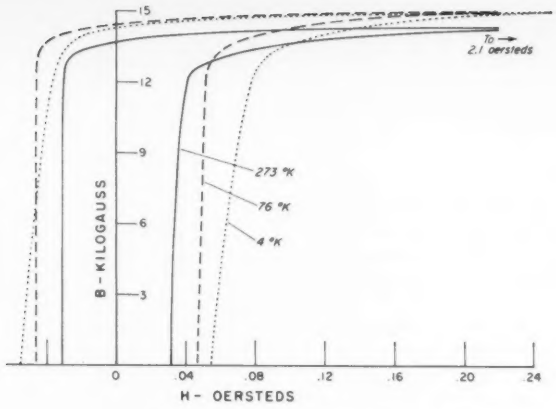

FIGURE 18. *Hysteresis loops.*
Material 210; laboratory preparation.

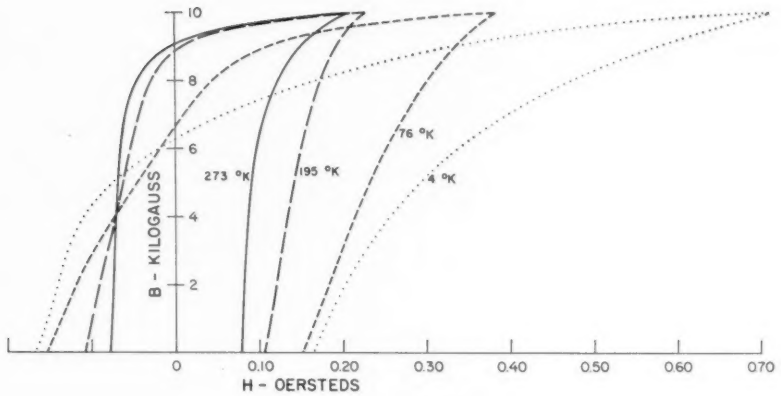

FIGURE 19. *Hysteresis loops.*
Material 211.

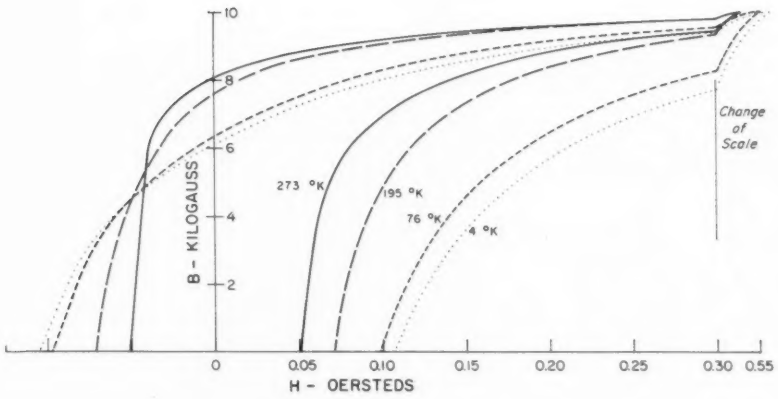

FIGURE 20. *Hysteresis loops.*
Material 213.

general more temperature sensitive than the Fe-Si alloys. Hysteresis loss increases on the order of 100 percent have been measured for some materials at 4 °K. The large decrease in residual induction at low temperatures may make this material less desirable for certain applications.

The authors gratefully acknowledge the assistance of the following people during the course of this project: W. M. Lightner of United States Steel Corporation and D. C. Dieterly of Armco Steel Corporation for supplying the material, D. O. Schwennesen of Magnetic Metals Company and C. E. Herr of Westinghouse Electric Corporation for fabrication of the samples, R. L. Powell and D. MacDonald for initiating much of the early project planning, J. C. Moulder for taking some of the experimental measurements, G. H. Wallace for equipment preparation, and N. V. Frederick and R. D. Harrington for use of the B-H loop tracer.

7. References

[1] R. L. Sanford and I. L. Cooter, Basic magnetic quantities and the measurement of the magnetic properties of materials, National Bureau of Standards Monograph **47,** (1962).

[2] ASTM Standards 1964, Part 8, A 343–60T, Alternating current magnetic properties of materials using Epstein specimens, ASTM, Philadelphia (1964).

[3] C. W. Chen, Temperature dependence of magnetic properties of silicon-iron, J. Appl. Phys. **29,** 1337 (1958).

[4] E. Tatsumoto and T. Okamoto, Temperature dependence of the magnetostriction constants in iron and silicon iron, J. Phys. Soc. Japan **14,** 1588–94 (1959).

[5] K. B. Vlasov and Ya. S. Shur, Temperature dependence of the coercive force in monocrystals of transformer steel, in Russian, J. Tech. Phys., USSR **21,** 39–50 (1951).

(Paper 69C3–203)

JOURNAL OF RESEARCH of the National Bureau of Standards—C. Engineering and Instrumentation

Vol. 69C, No. 3, July–September 1965

Publications of the National Bureau of Standards*

Selected Abstracts

Observations of dislocations and surface features in corundum crystals by electron transmission microscopy, D. J. Barber and Nancy J. Tighe, *J. Res. NBS* **69A** (*Phys. and Chem.*), *No. 3 (May–June 1965), 70 cents.*

Crystals of corundum, grown by the flame-fusion method, have been chemically thinned and examined by electron transmission microscopy. Some specimens were etch-pitted after thinning, and the relationship between etch pits and dislocations was investigated. Within subgrains there is a close agreement between dislocation and etch pit densities; this agreement breaks down along many boundaries. The etching behavior of crystals containing Cr_2O_3, TiO_2 and other impurities has been examined. Etch-tunnelling along grown-in dislocations is commonly observed in the impurity-doped materials; it is particularly pronounced in ruby. In heat-treated crystals containing TiO_2, local differences in solid solubility can lead to the formation of etch hillocks. Thermally etched surfaces have also been characterized, and gas atmospheres are shown to affect the surface topology. Evaporation experiments in the electron microscope are reported.

Phase velocities and attenuation distances in the ionosphere, D. R. Croley, Jr., and B. S. Tanenbaum, *Radio Science J. Res. NBS/USNC–URSI* **69D,** *No. 6, 819–825 (June 1965) $1.00.*

Plane wave phase velocities and attenuation distances in an infinite, homogeneous, partly ionized gas composed of an interacting mixture of neutral molecules, ions, and electrons in the presence of a uniform magnetic field are determined for three sets of plasma conditions corresponding to the 80, 100, and 300 kilometer levels of the ionosphere. Propagation in the parallel direction and the perpendicular direction relative to the magnetic field in the frequency range from approximately 10^{-5} c/s to 10^9 c/s is considered.

International comparison of atomic frequency standards via VLF radio signals, A. H. Morgan, E. L. Crow, B. E. Blair, *Radio Science J. Res. NBS/USNC–URSI* **69D,** *No. 7, (July 1965), $1.00.*

A study was made of data obtained over an 18-month period (July 1961 to December 1962, inclusive) on the comparison of atomic frequency standards located in seven laboratories in the United States, Europe, and Canada, using the VLF signals of GBR (16 kc/s), Rugby, England and NBA (18 kc/s), Balboa, Canal Zone. Each laboratory observes the accumulated difference in phase over a 24-hour period (the same for all laboratories, or nearly so) between its own standard (either laboratory or commercially constructed) and the received VLF signal. A statistical analysis was designed to separate the observations at each laboratory into three components: (a) long-term mean differences among the atomic standards; (b) estimates of the standard deviations, $\hat{\alpha}_i$, at each receiving station; and (c) estimates of the transmitter standard deviations, $\hat{\tau}$. Each $\hat{\alpha}_i$ includes receiver fluctuations, propagation effects peculiar to the path, and measurement uncertainties; $\hat{\tau}$ includes the transmitter fluctuations and propagation effects common to all paths.

The study shows that $\hat{\alpha}_i$ at each receiver varied from a low or 0.39×10^{-10} units of fractional frequency (that is, 0.39 parts in 10^{10}) (GBR data) at LSRH to a high of 1.97×10^{-10} (GBR data) at NRC with an average for all stations of 1.01×10^{-10} measured against GBR and 0.99×10^{-10} when measured against NBA. Also, the average $\hat{\tau}$ for GBR is 1.26×10^{-10} and for NBA is 0.68×10^{-10}. Finally, it is shown that: (1) the means of the frequencies of the seven individual atomic standards laboratories agreed with the grand mean of these seven standards to within ±2 parts in 10^{10} for the 18-month period, and (2) the laboratory-type standards agreed with their grand mean to within ±1 part in 10^{10}.

Control of WWV and WWVH standard frequency broadcasts by VLF and LF signals, B. E. Blair and A. H. Morgan, *Radio Science J. Res. NBS/USNC–URSI* **69D,** *No. 7, (July 1965), $1.00.*

Since 1961 the NBS VLF and LF signals have improved the calibration and frequency control of the WWV (Maryland) HF broadcasts. Similarly, better control of the WWVH (Hawaii) HF broadcasts was achieved in early 1963 by monitoring the NBS VLF broadcasts in terms of the WWVH control oscillator. In mid 1963 WWVL (20 kc/s) and WWVB (60 kc/s) were relocated from two sites near Boulder, Colorado, to a single site near Ft. Collins, Colorado, and the transmitter power for both broadcasts was increased several fold. These higher powered broadcasts resulted in more precise control of both HF broadcasts. Through the VLF and LF signals the 24-hour average frequency values of WWV are related to the United States Frequency Standard (USFS) within a few parts in 10^{11}.

This paper describes the NBS low frequency broadcasts, the method of using them to control and calibrate the HF broadcasts, and gives an analysis of the precision of frequency control obtained at WWV over a 21-month period. An appendix discusses the short-term phase stabilities and diurnal phase shifts observed in the low-frequency signals at WWV and WWVH, and examines the accuracy-limiting effects of propagation path characteristics and background noise levels in such received signals.

Theory of coil antennas, T. Padhi, *Radio Science J. Res. NBS/USNC–URSI* **69D,** *No. 7, (July 1965), $1.00.*

In this paper, a method is presented by which the distribution of current on some structurally simple coil or multiturn loop antennas may be obtained. The input admittances of unshielded and shielded coils are determined and their operation as receiving elements is considered.

Standard cells. Their construction, maintenance, and characteristics, W. J. Hamer, *NBS Mono. 84 (Jan. 15, 1965), 35 cents.*

This Monograph contains information on the construction, maintenance, and characteristics of standard cells. The effects of temperature, pressure, electric current, light, shock, and vibration on standard cells are discussed. A history of the realization and maintenance of the unit of electromotive force is also included. A record of international comparisons of the unit of electromotive force is presented as well as information on the constancy of the National Reference Group of Standard Cells.

Effects of thermal shrinkage on built-up roofing, W. C. Cullen, *NBS Mono. 89 (Mar. 4, 1965), 10 cents.*

The effects of thermal movement of bituminous built-up roof membranes are related to some common failures of built-up roofing observed in field exposures. A procedure for determining the amount of thermal movement of built-up membranes is described. Data are given for the thermal movement of various bitumens and reinforcing felts used in the construction of built-up roofs and for the composite membranes over a temperature range of $+30$ to -30 °F. The data obtained are related to field experience and suggestions are presented which will prove beneficial in reducing the incidence of built-up failure due to thermal movement.

Calibration of liquid-in-glass thermometers, J. F. Swindells, *NBS Mono. 90 (Feb. 12, 1965), 25 cents. Supersedes NBS Circ. 600.*

This Monograph, which supersedes Circular 600, contains information of general interest to both manufacturers and users of liquid-in-glass thermometers, as well as those who wish to calibrate thermometers or submit them to the National Bureau of Standards for calibration. Instructions are provided for applicants requesting calibration services, and the techniques and equipment used in the calibration procedures are described. Important elements of thermometer design are discussed, and factors affecting the use of common types of liquid-in-glass thermometers are included together with tables of tolerances and reasonably attainable accuracies. The calculation of corrections for the temperature of the emergent stem is given in detail for various types of thermometers and conditions of use.

Automatic indexing: A state-of-the-art report, M. E. Stevens, *NBS Mono. 91 (Mar. 20, 1965), $1.50.*

A state-of-the-art survey of automatic indexing systems and experiments has been conducted by the Research Information Center and Advisory Service on Information Processing, Information Technology Division, Institute for Applied Technology, National Bureau of Standards. Consideration is first given to indexes compiled by or with the aid of machines, including citation indexes. Automatic derivative indexing is exemplified by key-word-in-context (KWIC) and other word-in-context techniques. Advantages, disadvantages, and possibilities for modification and improvement are discussed. Experiments in automatic assignment indexing are summarized. Related research efforts in such areas as automatic classification and categorization, computer use of thesauri, statistical association techniques, and linguistic data processing are described. A major question is that of evaluation, particularly in view of evidence of human inter-indexer inconsistency. It is concluded that indexes based on words extracted from text are practical for many purposes today, and that automatic assignment indexing and classification experiments show promise for future progress.

The examination of weighing equipment, M. W. Jensen and R. W. Smith, *NBS Handb. 94 (Mar. 1, 1965), $3.00. Supersedes H37.*

This Handbook is primarily directed to the presentation of a coordinated series of step-by-step Examination Procedure Outlines (EPO's) for weighing equipment, recommended for adoption and use, as minimal requirements, by weights and measures agencies, commercial service agencies, weighing equipment owners and operators, and manufacturers of weighing devices. Supporting information embraces discussions on related topics such as reference and field standards report forms, tolerances, weighing principles, and elements of scale construction and performance. Extensive weights and measures tables—basic, interrelation of units, and equivalents—and a list of references for further study are appended. An alphabetical index is supplied.

Standard frequency and time services of the National Bureau of Standards, *NBS Misc. Publ. 236 (Jan. 15, 1965), 15 cents. Supersedes editions of Dec. 1, 1960 and July 1, 1961.*

Detailed descriptions are given of eight technical services provided by the National Bureau of Standards radio stations WWV, WWVH, WWVB, and WWVL. These services are: 1. Standard radio frequencies; 2. Standard audio frequencies; 3. Standard musical pitch; 4. Standard time intervals; 5. Time signals; 6. UT2 corrections; 7. Radio propagation forecasts; and 8. Geophysical alerts. In order to provide users with the best possible services, occasional changes in the broadcasting schedules are required. This publication shows the schedules in effect on January 1, 1965. Annual revisions will be made. Advance notices of changes occurring between revisions will be sent to regular users of these services upon request.

Standard Reference Materials: Sources of information, J. L. Hague, T. W. Mears, and R. E. Michaelis, *NBS Misc. Publ. 260–4 (Feb. 1965), 20 cents.*

This annotated listing of sources of Standard Reference Materials is prepared with references to all types of materials used to standardize analytical, physico-chemical, and engineering methods. The range of Standard Reference Materials included runs from high-purity substances and carefully analyzed metals, alloys, and rocks to materials of indefinitely known composition for standardizing a single phenomenon.

Standard Reference Materials: Accuracy of solution x-ray spectrometric analysis of copper-base alloys, R. Alvarez and R. Flitsch, *NBS Misc. Publ. 260–5 (Mar. 15, 1965), 25 cents.*

X-ray fluorescence spectrometry has been investigated as an independent method for the analysis of certain major constituents in NBS standard reference materials. The determination of copper and zinc in cartridge and aluminum brass samples which were to be certified as standard materials, was selected for study. After a preliminary analysis, a solution of the unknown and a closely-matched synthetic standard were compared without the use of an internal standard or added control element. To achieve reliable results, close control of the type and concentration of acid was found necessary, and, for cells employing films as windows, the position of the film was critical. The temperature rise of the cell during irradiation was 0.1 °C, which did not contribute significantly to error. Typical coefficients of variation obtained for individual results in a group of 8 runs were 0.3% for copper and 0.4% for zinc. The agreement between chemical and x-ray results was within 0.3% of the amount present for both elements.

Optical scintillation; a survey of the literature, J. R. Meyer-Arendt and C. B. Emmanuel, *NBS Tech. Note 225 (Apr. 5, 1965), 70 cents.*

In this Technical Note, main emphasis is placed on providing the reader with an exhaustive survey of the literature, covering the field of effects of atmospheric refraction on the propagation of electromagnetic radiation at optical frequencies.

One may distinguish systematic, regular, or normal refraction on the one side from random refraction on the other. The former can be predicted theoretically, using various types of atmospheric models; the latter requires analysis by statistical methods.

Numerous observational, experimental, and theoretical aspects of random refraction, that is, of scintillation in its widest sense, are discussed. The following topics are dealt with: refraction in plane and in spherically stratified media, refractive index variations, radio refraction, scintillation as a function of aperture size, zenith distance, site location, dispersion, and meteorological conditions, the frequency spectrum of scintillation, terrestrial scintillation, image distortion and contrast reduction, refraction and diffraction theories of scintillation, autocorrelation analyses, radio star scintillation, and coherence problems. Questions of atmospheric scattering, absorption, and depolarization are excluded. Finally, a brief review is given concerning newer experimental methods for the observation, recording, and analysis of optical scintillation, including suggestions as to what further theoretical and experimental efforts should be undertaken.

The Joule-Thomson process in cryogenic refrigeration systems, J. W. Dean and D. B. Mann, *NBS Tech. 227 (Feb. 14, 1965), 30 cents.*

A comprehensive analysis of the Joule-Thomson process as applied to cryogenic refrigeration systems is presented. The descriptions of the process already in the literature are usually for specific applications. In contrast, performance characteristics are presented here for helium, para-hydrogen, and nitrogen operations over a large range of process parameters.

A tabulation of Airy functions, H. T. Dougherty and M. E. Johnson, *NBS Tech. Note 228 (Sept. 18, 1964), 20 cents.*

A tabulation is provided for Wait's formulation of the Airy function and its first derivative. The argument covers the range of real values from -6.0 to $+6.0$ in intervals of 0.1. As an aid for their application the tabulations are also graphed.

Table of attenuation as a function of vane angle for rotary-vane attenuators ($A = -40 \log_{10} \cos \theta$), W. Larson, *NBS Tech. 229 (Jan. 7, 1965), $1.25.*

The table of attenuation as a function of vane angle gives the attenuation in decibels produced by an angular displace-

ment of the vane of a rotary-vane attenuator assuming ideal behavior of the attenuator. The attenuations for vane angles corresponding to the function $A = -40 \log_{10} \cos \theta$ are given in the table, where A is the attenuation in decibels and θ is the vane angle in degrees. The attenuations in decibels are given for increments of 0.001° for the values of θ from zero to 89.999° to the sixth decimal place and for the values of θ from 89.000° to 89.999° to the fifth decimal place. The table was designed for determining the attenuation in decibels of a rotary-vane attenuation utilizing a scale marked in degrees. Also, the table can be used to determine correct decibel markings for a rotary-vane attenuator with a direct reading scale regardless of gear ratio. The table can be used as an aid in analyzing the calibration data of a rotary-vane attenuator for characteristics which include inherent error. resettability, and gearing eccentricity.

Practical aspects of the use of ac-dc transfer instruments, E. S. Williams, *NBS Tech. Note 257 (Mar. 9, 1965) 15 cents.* Electrothermic transfer instruments may be used to make direct measurements of ac-dc difference or frequency influence. With a somewhat similar procedure an "unknown" a-c voltage or current may be accurately measured by determining the difference between it and a preset and accurately measured d-c equivalent. Test circuits and procedures are described and data taking and calculations are illustrated.

Summary of current research on archival microfilm, C. S. McCamy and C. I. Pope, *NBS Tech. Note 261 (Apr. 16, 1965), 25 cents.*
The discovery of aging blemishes on microfilm in storage has prompted a study of the statistical relationship of incidence to conditions of preparation and storage, the chemical and physical nature of the blemishes, and measures to be taken to prevent their formation. This paper is a report of progress in that study with recommendations based on current information. With few exceptions, reports of aging blemishes refer to negative silver-gelatin type microfilm in roll form. Extremely small amounts of information loss have been reported. In some large collections of microfilm, no blemishes have been found. No evidence of biological attack has been found. Apparently, image silver is ionized, migrates, and is reduced to colloidal silver. The reaction often proceeds in the manner described by Liesegang for other silver-gelatin systems. In laboratory tests, blemishes formed in the presence of minute amounts of peroxides, certain imbibed chemicals, and solid contaminants. Recommendations include: avoiding excessive densities on film, careful avoidance of physical damage to the image layer, the use of a small concentration of iodide ion in the fixer, thorough washing, uniform drying, storage at low temperature and humidity in sealed cans, careful avoidance of air-borne reactants, increased use of positive copies for archival storage, and careful periodic inspection of record films.

A calorimetric determination of the enthalpy of graphite from 1200 to 2600° K, E. D. West and S. Ishihara (*Proc. 3rd Symp. Thermal Physical Properties, Purdue Univ., Lafayette, Ind., Mar. 22–26, 1965*), *Book. Advances in Thermophysical Properties at Extreme Temperatures and Pressures, pp. 146–151 (American Society of Mechanical Engineers, New York, N.Y., 1965).*
Measurements are reported of the increase in the enthalpy of high-purity graphite between room temperature and 1200 to 2600° K. A new apparatus is described briefly. Methods of operation are developed which eliminate some systematic and random errors and are especially advantageous at high temperatures. The enthalpy data fit the equation

$$H_T - H_{298.15} = 28.9004T - 1.045 \times 10^{-4} T^2 - 16{,}126.2 \log_{10} T/313.15 - 8907.3$$

where H is in absolute joules per gram atomic weight and T in degrees Kelvin.

Impedance of sealed nickel-cadmium dry cells, R. J. Brodd and H. J. DeWane, *Electrochem. Tech.* **3,** *No. 1–2, 12–17 (Jan.-Feb. 1965).*
The impedance of various sizes of nickel-cadmium dry cells was measured as a function of frequency between 50 cps and 50 kpcs. The effects of aging, discharge, and temperature on the impedance of the cells were determined. The temperature coefficient of electromotive force was determined for some cells. The discharge characteristics of AA-size nickel-cadmium and Leclanche cells were compared on two standard tests. It was found that the impedance of nickel-cadmium cells increased during discharge, decreased about 2 to 3 percent per °C increase in temperature, increased slightly during storage, was less for larger cells, and that for cells of equal rated capacity, the sintered type had a smaller impedance than the pressed-powder type.

Resins and technics used in constructing dentures, G. C. Paffenbarger, J. B. Woelfel, and W. T. Sweeney, *Dental Clinics of North America, 51–262 (W. B. Saunders Co., Philadelphia, Pa., 1965).*
Four technic dentures and usually eight clinical dentures were made with eight different types of acrylic resins, a polystyrene, a vinyl-acrylic copolymer, an epoxy resin, and hard rubber. The dentures were processed with the equipment recommended by the manufacturer.
Thick dentures had less shrinkage on processing and less dimensional change during use, when wetted, dried in air, and heated in water. Therefore, the denture should be made as thick as comfort and function will permit.
None of the dimensional changes of dentures that occurred during processing or in use could be detected clinically. The conventional acrylic resins processed with the usual dental technic of compression molding produced dentures that were just as stable in dimension as those produced by special resins and applicances.

The polarographic analysis of titanium (IV)—EDTA complex: Application to paint pigments, H. W. Berger and B. C. Cadoff, *Offic. Digest Paint Tech.* **37,** *No. 480, 28–34 (Jan. 1965).*
The Ti^{+4}-EDTA complex, buffered at *p*H 4.7, has been found to give polarographic waves suitable for the analysis of TiO_2 in paint pigments. A linear relationship between diffusion current and concentration of Ti^{+4} for the range 2.8×10^{-5} to 8.4×10^{-3}M has been observed. The pigments analyzed have been either in the dry form or extracted from whole paint. The method gives results in good agreement with the more complicated and time-consuming standard wet chemical method.

A high-speed (milliseconds) method for the simultaneous measurement of enthalpy, specific heat, and resistivity of electrical conductors at high temperatures, A. Cezairliyan (*Proc. 3rd Symp. Thermophysical Properties, 1965*), *Book, Advances in Thermophysical Properties at Extreme Temperatures and pressures, Pp. 253–262 (American Society of Mechanical Engineers, New York, N.Y., 1965).*
A method for the simultaneous measurement of enthalpy, specific heat, and electrical resistivity of electrical conductors at high temperatures (1000 °K to the melting point of the sample) in experiments of short duration (milliseconds) is described. The rapid direct joule heating is achieved by a single energy pulse obtained from a battery. The average heating rate was approximately 6600 °K s^{-1}. The sample is tubular in form with a small hole in the middle to approximate blackbody conditions, thus allowing the measurement of transient true temperatures by photoelectric methods. Results on molybdenum (up to approximately 1600 °K) are obtained and compared with available literature values.

Application of cooled air detector in an optical system, S. Abramowitz, A. M. Bass, and A. E. Ledford, Jr., *Appl. Opt.* **4,** *No. 2, p. 255 (Feb. 1965).*
A new method for cooling photoconductive detectors is described in which the detector is mounted on a copper rod attached to a refrigerant. An ellipsoid which is mounted in a common vacuum chamber with the detector is used to focus the emergent beam onto the detector.

On the relative roles of free volume and activation energy in the viscosity of liquids, P. B. Macedo and T. A. Litovitz, *J. Chem. Phys.* **42,** *No. 1, 245–256 (Jan. 1, 1965).*

The deficiencies in the rate theory approach of Eyring and the free volume theory of Cohen and Turnbull for liquid viscosities have been reconsidered. The rate theory has been reformulated using the Cohen and Turnbull expression for the probability of finding a vacant site and yields an equation of the form,

$$\eta = A_0 \exp [E^*_{V/RT} + \gamma V_{0/Vf}].$$

This result has been applied to many liquids ranging from fused silica to liquid argon and including polyatomic van der Waals as well as hydrogen bonded liquids.
Consistent fits to both temperature and pressure dependence of viscosity were obtained. A significant conclusion is that the free volume of liquids is considerably higher than that suggested by the WLF and Cohen and Turnbull equations.

Zeeman filter, D. G. Dessler and W. G. Schweitzer, Jr., *J. Opt. Soc. Am.* **55,** *No. 3, 284–288 (Mar. 1965).*
A description is given of the Zeeman Filter, a very narrow optical band-pass filter. The filtering action is achieved by Zeeman splitting a resonant absorption line in a magnetic field. With the 2537 Å-resonance absorption line of Hg^{198} such a filter can produce a filtered line as narrow as .005 cm^{-1}.

Triggered fuse for load protection, J. H. Rogers, *Rev. Sci. Instr.* **35,** *No. 12, 1715 (Dec. 1964).*
This is a circuit designed to add positive protection for sensitive loads connected to high capacity power supplies. It is especially useful for protecting klystron microwave oscillator tubes. It is reliable and uses a minimum of components, hence it is economical and easy to construct.

Safety in the use of liquid hydrogen, D. B. Chelton, *Book, Technology and Uses of Liquid Hydrogen, ed. R. B. Scott, W. H. Denton, and C. M. Nicholls, ch. 10, pp. 359–378 (Pergamon Press, Inc., New York, N.Y., 1964).*
Safety in systems using liquid hydrogen is a subject of considerable present-day importance. Reducing or eliminating the potential safety hazards involved requires a basic understanding of the physical and chemical properties of hydrogen and the application of known safety technology. These factors are reviewed and recommendations are given for safety criteria. Comparisons are made with propane and methane to assist in establishing the relative hazard. Consideration is given in the use of liquid hydrogen on a large scale and on a laboratory scale.

The performance of lenses made from inhomogeneous glasses, F. W. Rosberry, *Appl. Opt.* **4,** *No. 1, 21–24 (Jan. 1965).*
The performance of lenses made from glass elements containing defects such as bubbles, streaks, striae, etc., has been measured and an attempt made to compare the effect of the various defects. Four defective and a good or control lens, were used. The performance in the image plane was determined by four different evaluation procedures. A summary evaluation showed that the lens containing stria, although the most difficult defect to detect, produced the lowest quality image.

Stress-induced Martensite transformation in 18Cr-8 Ni Steel, R. P. Reed and C. J. Guntner, *Trans. Met. Soc. AIME* **230,** *1713–1720 (Dec. 1964).*
A commercial 18Cr–8Ni iron alloy (AISI 304L) was examined in tension at 300°, 76°, 20°, and 4°K. Continuous stress-strain recordings were made, X-ray analyses at periodic stress (strain) intervals were obtained, and the magnetic measurements were taken. From this data the percentage of martensitic products [bcc (α) and hcp (ϵ)] was computed as a function of stress (strain). It was found that up to 15 pct ϵ phase forms at low temperatures. The amount of ϵ formed increases to a maximum at about 5 pct strain, then decreases. This decrease indicates the additional transformation of ϵ to α'. The total amount of ϵ and α' was suppressed at constant stress (strain) at 4°K as compared to 76°K. It is proposed that the suppression of ϵ and α' is associated with the decreased mobility of extended dislocations at very low temperatures. The yield strength decreased as the temperature was depressed below room temperature and then increased rapidly near 4°K.

Metallized polymer film guard rings for dielectric measurements, A. H. Scott, *Mater. Res. Std. Tech. Note 5, No. 2, 76–78 (Feb. 1965).*
Dielectric measurements have been made using a metallized polymer film as a guard electrode over a tinfoil guarded electrode on three disk specimens. Comparisons with measurements using the regular tinfoil guard-ring indicate that errors of 1.5% or more in capacitance and 3×10^{-4} or more in dissipation factor can be expected under certain conditions.

All-glass sorption vacuum trap, F. B. Haller, *Rev. Sci. Instr.* **35,** *No. 10, 1356–1357 (Oct. 1964).*
An ultra high vacuum sorption trap consisting entirely of glass is described. The trapping medium is a commercially available 96% silica porous glass. Advantages offered are freedom from dust and capability of mounting in any position.

Comparisons of tearing-strength tests for leather, T. J. Carter, *J. Am. Leather Chem. Assoc.* **LX,** *No. 1, 4–14 (Jan. 1965).*
Slit-tear, double-hole stitch-tear, single-hole stitch-tear, and tongue-tear tests were made on different types of leather to determine their relative merits. Analysis of the data shows that the slit-tear and the tongue-tear tests are more sensitive than the double-hole stitch-tear and the single-hole stitch-tear tests. The double-hole stitch-tear test was found to be the least sensitive. The tearing processes in the slit-tear and tongue tests are similar, and differ considerably from the tearing processes in the double-hole and the single-hole stitch-tear tests. Results show the tearing load to be unrelated to the direction of tear.

Thermal insulation storage, transport and transfer of liquid hydrogen, R. B. Jacobs, *Book, Technology and Uses of Liquid Hydrogen, ed. R. B. Scott, W. H. Denton, and C. M. Nicholls, ch. 4, pp. 106–148 (Pergamon Press, Inc., New York, N.Y., 1964).*
This manuscript is a chapter in a book entitled "The Technology and Uses of Liquid Hydrogen" to be published by Pergamon Press. It presents information useful to the designers and users of equipment for the storage, transport, and transfer of liquid hydrogen. The topics discussed are, in general, confined to those which are unique to cryogenic equipment; those concepts and techniques which are used in connection with equipment that operates at normal temperatures are not discussed. The chapter is divided into three sections: Thermal Insulation, Containers, and Transfer Systems. The discussion of thermal insulation includes information for non-insulated equipment, for non-vacuum insulated equipment, and for vacuum insulated equipment. examples of other areas that are discussed include instrumentation, cooldown requirements, pressurization, valves, pumps, and fluid mechanical design.

The response of microwave refractometer cavities to atmospheric variations, R. O. Gilmer, R. E. McGavin, and B. R. Bean, *Proc. 1964 World Conf. Radio Meteorology and 11th Weather Radar Conf., pp. 244–247 (1964).*
The microwave refractometer has been used extensively in the study of the refractive index structure of the atmosphere. Little work has been done evaluating the sampling cavity of the refractometer as an accurate measuring probe of the short-term variations of the atmosphere. Wind tunnel, water flow tunnel, and free atmospheric tests of the microwave sampling cavities currently in use have yielded information on aspect and velocity sensitivity, and on the spacial resolution of the cavities.
The tests revealed that the air flow through the sampling cavity undergoes a transition from laminar to turbulent type flow at wind velocities in excess of 5 mph. The pressure in the cavity decreases as the wind velocity increases. The indicated error due to the pressure drop at 15°C is as high as 1 *N* unit at 135 mph for a cavity oriented into the wind. This error appears to be a function of the aspect of the cavity relative to the direction of the wind, becoming a minimum at an angle of 45°.
Flow tunnel tests gave direct visual indications of the flushing time versus the aspect angle of the sampling cavities. A

characteristic flushing length of approximately 2.5 feet for complete flushing was measured at 0° as compared to 5.75 feet at 90°.

Characteristics of dosimeter films processed in phenidone-thiosulfate monobaths, M. Ehrlich, *J. Phot. Sci. Engr.* **9,** *No. 1, 1–9 (Jan.–Feb. 1965).*

Characteristics of commercial x-ray dosimetry films exposed to photons of widely different energies were compared for processing in phenidone-thiosulfate monobaths and in x-ray and phenidone developers. Monobath processing has a number of advantages for routine dosimetry applications. There is little dependence of response on processing time and temperature and, because of lower contrast, the useful exposure range is extended. But difficulties due to rate dependence are more likely, and film sensitivity is reduced.

One of the main features of the sensitometric behavior and the grain structure obtained with monobath processing is the interplay of the characteristics of "physical development," prevailing at low density levels, and those of "chemical development" at high densities. In contrast to their appearance for conventional development, the silver aggregates corresponding to fog produced by the monobath and the aggregates corresponding to relatively low densities above fog are large, smooth, and compact. The corresponding photometric equivalent is high. For higher exposures and densities, the differences in photometric equivalent and in the structure of the image silver for conventional and monobath processing tend to disappear. This points toward a change in the predominant development mechanism with density level.

The calibration of the National Bureau of Standards' tritiated-toluene standard of radioactivity, S. B. Garfinkel, W. B. Mann, R. W. Medlock, and O. Yura, *Intern. J. Appl. Radiation Isotopes* **16,** *27–33 (1965).*

The difficulties encountered, and their solution, when calibrating a radioactivity standard of tritiated toluene by comparison with the NBS tritiated-water standard by means of liquid-scintillation counting, are described. Leaks in the seals of commercial vials, giving rise to uncontrolled oxygen quenching, were eliminated by modifying the seals. White plastic caps gave higher count rates than black plastic caps. A new and highly precise method of dilution was used.

The ratio of the activities of the two standards was determined with a standard error of less than 0.1 percent.

Conductance of glass immersed in molten salts, K. H. Stern, *J. Electrochem. Soc.* **112,** *No. 2, 208–210 (Feb. 1965).*

The electrical conductance of high SiO_2 glass was measured when immersed in a number of molten salts and salt mixtures between 800° and 900°C. Sodium and lithium ions diffuse into the glass, both from their own chlorides and from low concentrations in KCl. The glass comes to equilibrium with each melt composition, the time of equilibration depending on the particular ions in the melt. The activation energy of sodium and lithium ion conduction in glass is 75–84 kJ (18–20 kcal), with potassium it is variable between 105 kJ (25 kcal) and 167 kJ (40 kcal). The conductance method is not sufficiently precise to detect silver and cuprous ion diffusion into glass.

Other NBS Publications

J. Research NBS 69A (Phys. and Chem.), No. 3 (May–June 1965), 70 cents.

Electronic structure and magnetic properties of the neptunyl ion. J. C. Eisenstein and M. H. L. Pryce.

Heats of transformations in bismuth oxide by differential thermal analysis. E. M. Levin and C. L. McDaniel.

Phase relations between iridium and the sesquioxides in air. S. J. Schneider, J. L. Waring, and R. E. Tressler.

Phase equilibrium relationships in the system Gd_2O_3-TiO_2. J. L. Waring and S. J. Schneider.

Acid-base behavior in 50-percent aqueous methanol: thermodynamics of the dissociation of protonated tris(hydroxymethyl) aminomethane and nature of the solvent effect. M. Woodhead, M. Paabo, R. A. Robinson, and R. G. Bates.

Observations of dislocations and surface features in corundum crystals by electron transmission microscopy. D. J. Barber and N. J. Tighe. (See above abstracts.)

Low-frequency dielectric properties of liquid boric oxide. K. H. Stern.

Mass spectrometric study of the effects of nitric oxide and other additives on "purified" active nitrogen. J. T. Herron.

Synthesis and ring structure of 7-acetamido-7-deoxy-L-*galacto*-heptulose. E. J. McDonald.

J. Research NBS 69B (Math. and Math. Phys.), No. 1 and 2 (Jan.–June 1965), 75 cents.

Lectures on matroids. W. T. Tutte.

Menger's theorem for matroids. W. T. Tutte.

Single-element extensions of matroids. H. H. Crapo.

Minimum partition of a matroid into independent subsets. J. Edmonds.

Lehman's switching game and a theorem of Tutte and Nash-Williams. J. Edmonds.

On the connection between the properties of oriented linear graphs and anlyses of lumped pysical systems. H. M. Trent.

Character subgroups of *F*-groups. M. I. Knopp and M. Newman.

A note on multipliers of difference sets. R. A. Brauldi.

Modification of Edmonds' maximum matching algorithm. C. Witzgall and C. T. Zahn, Jr.

On measurable sets and functions. A. J. Goldman.

Characteristic formulation for nonperiodic solutions of Mathieu's equation. T. Tamir and H. C. Wang.

On the surface duality of linear graphs. J. Edmonds.

Maximum matching and a polyhedron with 0, 1-vertices. J. Edmonds.

Radio Sci. J. Res. NBS/USNC–URSI 69D, No. 6 (June 1965). $1.00.

Cyclotron harmonic waves in warm plasmas. F. W. Crawford.

Propagation of waves across a magnetoplasma-vacuum boundary. R. L. Gallawa.

Phase velocities and attenuation distances in the ionosphere. D. R. Croley, Jr., and B. S. Tanenbaum. (See above abstracts).

Ionospheric effects of electrostatic fields generated in the outer magnetosphere. G. C. Reid.

An experimental study of plasma sheath effects on antennas. G. Tyras, P. C. Bargeliotes, J. M. Hamm and R. R. Schell.

An approach to improve re-entry communications by suitable orientations of antenna and static magnetic field. S. N. Samaddar.

Concerning the mechanism of reflection of electromagnetic waves from an inhomogeneous lossy plasma. J. R. Wait.

Selection of Papers Presented at 1964 World Conference on Radio Meteorology, Boulder, Colo., Sept. 14–18, 1964

Angels in focus. D. Atlas.

An investigation of clear air stratification with radar and elevated instruments. D. R. Hay and K. Naito.

On inferring the refractive-index structure of the troposphere from electromagnetic scattering experiments. P. L. Smith, Jr.

The biexponential nature of tropospheric gaseous absorption of radio waves. E. J. Dutton and B. R. Bean.

Complete scattering parameters of polydispersed hydrometer in the λ 0.1 to λ10 cm range. D. Deirmendjian.

Radio Sci. J. Res. NBS/USNC-URSI 69D, No. 7 (July 1965), $1.00.

International comparison of atomic frequency standards via VLF radio signals. A. H. Morgan, E. L. Crow, and B. E. Blair. (See above abstracts).

Control of WWV and WWVH standard frequency broadcasts by VLF and LF signals. B. E. Blair and A. H. Morgan. (See above abstracts).

Measurements of the total electron content and the equivalent slab thickness of the midlatitude ionosphere. R. V. Bhonsle, A. V. da Rosa, and O. K. Garriott.

D-region absorption at 10 and 15 Mc/s during the total solar eclipse of July 20, 1963. G. M. Lerfald, J. K. Hargreaves, and J. M. Watts.
Effect of the eclipse of 20 July 1963 on VLF signals propagating over short paths. J. H. Crary and D.E. Schneible.
A comparison of radar auroral reflection data with acoustic wave theory. R. L. Leadabrand.
Electromagnetic properties of a plasma covered antenna. D. J. Jacavanco.
Influence of an inhomogeneous ground on the propagation of VLF radio waves in the earth-ionosphere waveguide. J. R. Wait.
Aspects of the terrestrial ELF noise spectrum when near the source or its antipode. L. G. Abraham, Jr.
Analysis of linear arrays focused in the Fresnel region. P. P. Lombardini, R. Doviak, and J. Goldhirsh.
Theory of coil antennas. T. Padhi. (See above abstracts).
Small prolate spheroidal antenna in a dissipative medium. R. H. Williams, R. D. Kelly, and W. T. Cowan.
Calculated curve for groundwave propagation over inhomogeneous earth with pronounced topographical features. K. Furutsu.

Radio Sci. J. Res. NBS/USNC-URSI 69D, No. 8 (Aug. 1965) $1.00.

"Ultra Low Frequency Electromagnetic Fields" Papers

Preface to "Ultra Low Frequency Electromagnetic Fields" Papers. W. H. Campbell and S. Matsushita.
Solar wind and its interaction with the magnetosphere. C. P. Sonett.
Schumann resonances. J. Galejs.
Earth-ionsophere cavity resonances and the propagation of ELF radio waves. J. R. Wait.
Resonances of the earth-ionosphere cavity observed at Cambridge, England. M. J. Rycroft.
Experimental results on the dynamics of the *F* region. W. Becker, R. Rüster, and J. Klostermeyer.
Regular oscillations near 1 c/s observed at middle and low latitudes. L. Tepley.
Preliminary results of a micropulsation experiment at conjugate points. R. E. Gendrin and V. A. Troitskaya.
Some characteristics of geomagnetic pulsations at frequencies near 1 c/s. W. H. Campbell and E. C. Stiltner.
Propagation of hydromagnetic waves in the magnetosphere. M. Sugiura.
Ionospheric perturbation (the roles played by the ionosphere in geomagnetic pulsations). S. Matsushita.
Effects of induced earth currents on low-frequency electromagnetic oscillations. A. T. Price.
Equatorial effects. R. Hutton.
Interpretation of early magnetic transients caused by high-altitude nuclear detonations. S. L. Kahalas and P. Newman.

Abstracts of ULF Conference papers not published in this issue

A note on the application of pulse compression techniques to ionospheric sounding. D. C. Coll and J. R. Storey.
Comments on a paper "Measurement of the phase velocity of VLF propagation in the earth ionosphere waveguide" by F. K. Steele and C. J. Chilton. H. F. Bates.
Reply to H. F. Bates' "Comments on 'Measurements of the phase velocity of VLF propagation in the earth ionosphere waveguide' by F. K. Steele and C. J. Chilton." F. K. Steele and C. J. Chilton.

Report of the 49th National Conference on Weights and Measures 1964, NBS Misc. Publ. 263 (Feb. 1, 1965) $1.00.
Technical highlights of the National Bureau of Standards, Annual Report 1964, NBS Misc. Publ. 264 (Dec. 1964) $1.00.
Thermal properties of aqueous uni-univalent electrolytes, V. B. Parker, NSRDS–NS 2 (Apr. 1, 1965), 45 cents.
Pipe nipples: Brass, copper, steel, and wrought-iron, CS5–65 (Jan. 15, 1965), 10 cents. Supersedes CS5–46.
Builders' template hinges, CS9–65 (Jan. 15, 1965), 10 cents. (Supersedes CS9–33).
Aluminum alloy chain link fencing, CS269–65 (Mar. 1, 1965), 10 cents.
Ponderosa pine windows, sash, and screens (using single glass and insulating glass), CS163–64 (Mar. 17, 1964) 15 cents. Supersedes CS163–59 and CS193–53.
Wood double-hung window units, CS190–64, (Mar. 17, 1964), 10 cents. Supersedes CS190–59.
Wood awning window units, CS204–64 March 17, 1964), 10 cents. Supersedes CS204–59.
Wood casement window units, CS205–64 (Mar. 17, 1964), 10 cents. Supersedes CS205–59.
Wood horizontal-sliding window units (all sash operating), CS264–64 (Mar. 17, 1964), 10 cents.
Wood horizontal-sliding window units (one or more non-operating sash), CS265–64 (Mar. 17, 1964), 10 cents.
Wood single-hung window units, CS266–64 (Mar. 17, 1964), 10 cents.
Quarterly radio noise data September, October, November 1963, W. Q. Crichlow, R. T. Disney, and M. A. Jenkins, NBS Tech. Note 18–20 (Oct. 23, 1964), 50 cents.
Quarterly radio noise data December, January, February, 1963–64, W. Q. Crichlow, R. T. Disney, and M. A. Jenkins, NBS Tech. Note 18–21 (Jan. 25, 1965), 50 cents.
Bibliography of fading on microwave line of sight tropospheric propagation paths and associated subjects, H. T. Dougherty, NBS Tech. Note 302 (Aug. 31, 1964), 60 cents.
Bibliography on tropospheric propagation of radio waves, W. Nupen, NBS Tech. Note 304 (Apr. 1, 1965), $2.00.
Atlas of Fourier coefficients of diurnal variation of foF_2. Part II. Distribution of amplitude and phase, W. B. Jones and R. M. Gallet, NBS Tech. Note 305 (Feb. 14, 1965), 60 cents.
Resonance effects of electrostatic oscillations in the ionosphere, J. A. Fejer and W. Calvert, J. Geophys. Res. **69,** 5049–5062 (Dec. 1964).
Observatory report on JILA, L. M. Branscomb, Astron. J. **69,** 700–703 (Nov. 1964). Nonlinear ambipolar diffusion of an isothermal plasma across a magnetic field, E. R. Mosburg and K. B. Persson, Phys. Fluids **7,** 1829–1833 (Nov. 1964).
Laboratory studies of helium ion loss processes of interest in the ionosphere, E. E. Ferguson, F. C. Fehsenfeld, D. B. Dunkin, A. L. Schmeltekopf, and H. I. Schiff, Planetary Space Sci. **12,** 1169–1171 (Dec. 1964).
Interaction of maxima in the absorption of soft X-ray, J. W. Cooper, Phys. Rev. Letters **13,** No. 25, 762–764 (Dec. 21, 1964).
Complex Lorentz group with a real metric. I. Group structure, A. O. Barut, J. Math. Phys. **5,** 1652–1656 (Nov. 1964).
Climatology of elevated super-refractive layers arising from atmospheric subsidence, B. A. Cahoon and L. P. Riggs, Proc. 1964 World Conf. Radio Meteorology and 11th Weather Radar Conf., pp. 52–55 (1964).
Annual report from the National Bureau of Standards, C. E. Moore, Astron, J. **68,** No. 9, 1–3 Nov. 1964).
Nuclear magnetic moment of Pr^{141} from the hyperfine structure of doubly ionized praseodymium, J. Reader and J. Sugar, Phys. Rev. **137,** No. 4B, B784–B789 (Feb. 22, 1965).
Brightness temperature of the atmosphere using a biexponential model in the 6–45 GHz/s frequency range, E. J. Dutton, B. R. Bean, and E. R. Westwater, Proc. 1964 World Conf. Radio Meteorology and 11th Weather Radar Conf., pp. 212–215 (1964).
Natural variations in the abundance ratio and the atomic weight of copper, W. R. Shields, S. S. Goldich, E. L. Garner, and T. J. Murphy, J. Geophys. Res. **70,** No. 2 479–491 (Jan. 15, 1965).
Optical heterodyne detection of the forward stimulated Brillouin scattering, D. A. Jennings and H. Takuma, Appl. Phys. Letters **5,** 241–242 (Dec. 1964).
The uses of oblique ionograms in frequency utilization, K. Davies, Telecommun. J. **31,** 281–287 (Oct. 1964).
Conductance of glass immersed in molten salts, K. H. Stern, J. Electrochem. Soc. **112,** No. 2, 208–210 (Feb. 1965).
Reversal of the diurnal phase variations of GBR (16 kilocycles per second) observed over a path of 720 kilometers,

D. D. Crombie and H. L. Rath, J. Geophys. Res. **69**, No. 23, 5023–5027 (Dec. 1, 1964).

Magnetic properties of ilmenite-hematite solid solutions, C. F. Jefferson and R. G. West, J. Am. Ceram. Soc. **47**, No. 11, 544–548 (Nov. 1964).

Thermodynamics of hydrogen solubility in cryogenic solvents at high pressures, M. Orentlicher and J. M. Prausnitz, Book, Chem. Eng. Sci. **19**, 775–782 (1964).

Liquid air, R. B. Scott, Encyclopaedic Dictionary of Physics, p. 1 (Pergamon Press, Inc., New York, N.Y., 1964).

Properties of normal and para hydrogen, R. B. Stewart and H. M. Roder, Book, Technology and Uses of Liquid Hydrogen, ed. R. B. Scott, W. H. Denton, and C. M. Nicholls, ch. 11, pp. 379–404 (Pergamon Press, Inc., New York, N.Y., 1964).

High resolution, low energy electron spectrometer, J. A. Simpson, Rev. Sci. Instr. **35**, No. 12, 1698–1704 (Dec. 1964).

The calculation of electron energy distribution functions in the ionosphere, L. R. Megill and J. H. Cahn, J. Geophys. Res. **69**, No. 23, 5041–5048 (Dec. 1, 1964).

Solar flares with associated active dark filaments and their relation to 2800 Mc/s radio bursts, M. W. Haurwitz, Astrophys. J. **140**, No. 3, 1236–1246 (Oct. 1, 1964).

Mechanism of inactivation of bacteriophages by metals, N. Yamamoto, C. W. Hiatt, and W. Haller, Biochim, Biophys. Acta **91,** 257–261 (1964).

Electron-impact studies of aromatic hydrocarbons. III. Azulene and naphthalene, R. J. Van Brunt and M. E. Wacks, J. Chem. Phys. **41,** No. 10, 2395–3199 (Nov. 15, 1964).

Early strength, flow and dimensional changes obtained on amalgam perpared with a standardized mechanical technic, H. J. Caul, W. S. Crowell, W. D. Kimmel, and G. C. Paffenbarger, J. Am. Dental Assoc. **69,** 742–748 (Dec. 1964).

Photochemical changes in thin layer chromatograms of polycyclic, aromatic hydrocarbons, M. N. Inscoe, Anal. Chem. **36,** No. 13, 2505–2506 (Dec. 1964).

Surface integral form for three-body collision in the Boltzmann equation, M. S. Green, Phys. Rev. **136,** No. 4A, A905–A910 (Nov. 16, 1964).

Nucleation characteristics of static liquid nitrogen and liquid hydrogen, J. Hord, R. B. Jacobs, C. C. Robinson, and L. L. Sparks, J. Eng. Power **86,** 485–495 (Oct. 1964).

Degree of metamerism, I. Nimeroff and J. A. Yurow, J. Opt. Soc. Am. **55,** No. 2, 185–190 (Feb. 1965).

Food for tomorrow's billions, A. T. McPherson, Proc. forum "Food in the Future: Concepts for Planning," Chicago, Ill., Oct. 8–9, 1964, pp. 51–73 (Dairy and Food Industries Supply Assoc., 1964).

Is life possible on other planets? W. R. Bozman, Science and Children **2,** No. 4, 7 (Dec. 1964).

Investigation of plasma boundaries with electromagnetic surface waves, H. W. Wassink and A. J. Estin, J. Appl. Phys. **35,** No. 10, 2795–2800 (Oct. 1964).

Comments on a paper by R. L. Closs, "An experimental investigation of back scattering or radio waves from the equatorial electrojet," R. Cohen and D. T. Farley, Jr., Proc. Phys. Soc. **84,** Pt. 4, No. 540, 619–620 (J. W. Arrowsmith Ltd., London, England 1964).

Changes in living, J. P. Eberhard, Proc. Conf. The Environment of Change, Sterling Forest, Tuxedo, N.Y., June 14–17, 1964, pp. 62–67 (1964).

Liquefied gases, handling of; R. B. Scott, Encylopaedic Dictionary of Physics, p. 1 (Pergamon Press, Inc., New York, N.Y. 1964).

Low-temperature apparatus, constructional materials for, R. B. Scott, Encyclopaedic Dictionary of Physics, pp. 1–2 (Pergamon Press, Inc., New York, N.Y. 1964).

Electron-impact studies of aromatic hydrocarbons. II Naphthacene, chrysene, tripenylene, and pyrene, M. E. Wacks, J. Chem. Phys. **41,** No. 6, 1661–1666 (Sept. 15, 1964).

Formation of NF from NF_2 by photolysis, D. E. Mann and J. J. Comford, Spectrochim. Acta **21,** 197–198 (Pergamon Press Ltd. Northern Ireland 1965).

The influence of metastable oxygen molecules on ozone and airglow, H. I. Schiff and L. R. Megill, J. Geophys. Res. **69,** No. 23, 5120–5121 (Dec. 1, 1964).

Shape of the magnetospheric boundary under solar wind pressure, R. J. Slutz and J. R. Winkelman, J. Geophys. Res. **69,** No. 23, 4933–4948 (Dec. 1, 1964)

Standards—the foundation of industrial growth, R. D. Stiehler, Industrial Times **VI,** No. 22 (Bombay, India, Nov. 15, 1964).

Hyperfine structure of the $B^2\Sigma^+$ state of CN, H. E. Radford, Phys. Rev. **136,** No. 6A, A1571–A1575 (Dec. 14, 1964).

Research for architecture, J. P. Eberhard, Res. News **II,** No. 1, 10–19 (Jan. 1965).

Spectral properties of plants, D. M. Gates, H. J. Keegan, J. C. Schleter, and V. R. Weidner, Appl. Opt. **4,** No. 1, 11–20 (Jan. 1965).

Blood:bone equilibrium in calcium homoeostasis, J. MacGregor and W. E. Brown, Nature **205,** No. 4969, 359–361 (Jan. 23, 1965).

Carbon monoxide on niobium, R. Klein and J. W. Little, Surface Science **2,** 167–176 (North-Holland Publ. Co., Amsterdam, The Netherlands, 1964).

Fracture in corrosive media, H. L. Logan, Book, Fracture of Engineering Materials, ch. 8, pp. 143–161 (American Society for Metals, Metals Park, Ohio, Nov. 1964).

Gas-phase radiolysis of *n*-pentane. A study of the decompositions of the parent ion and neutral excited pentane molecule, P. Ausloos and S. G. Lias, J. Chem. Phys. **41,** No. 12, 3962–3970 (Dec. 15, 1964).

Moderation in instrumentation, J. K. Taylor, Science Teacher **32,** No. 3, 18–19 (Mar. 1965).

Pressure-indicator-paste patterns in duplicate dentures made by different processing technics for the same patients, J. B. Woelfel and G. C. Paffenbarger, J. Am. Dental Assoc. **70,** 339–343 (Feb. 1965).

Radioisotope dilution and its application to the radioassay of Ce^{144}, L. A. Currie, G. M. France, III, and H. L. Steinberg, Intern. J. Appl. Radiation Isotopes **16,** No. 1, 1–8 (Jan. 1965).

Reference buffer solutions for *p*H measurements in 50% methanol. Dissociation constants of acetic acid and dihydrogen phosphate ion from 10 to 40°, M. Paabo, R. A. Robinson, and R. G. Bates, J. Am. Chem. Soc. **87,** 415–418 (1965).

Spectra of matrix-isolated NiF_2 and $NiCl_2$, D. E. Milligan, M. E. Jacox, and J. D. McKinley, J. Chem. Phys. **42,** No. 3, 902–905 (Feb. 1965).

The structures of anhydrous sodium trimetaphosphate, $Na_3P_3O_9$, and the monohydrate, $Na_3P_3O_9{\cdot}H_2O$, H. M. Ondik, Acta. Cryst. **18,** pt 2, 226–232 (Feb. 1965).

Vacuum ultraviolet photochemistry. VIII. Propylene, D. A. Becker, H. Ikabe, and J. R. McNesby, J. Phys. Chem. **69,** No. 2, 538–542 (Feb. 1965).

A magnetic amplifier for use with diode logic, E. W. Hogue, IEEE Trans. Commun. Electron. **83,** No. 75, 803–808 (Nov. 1964).

A study of the variation of the surface electrical resistance of lead iodide films with relative humidity at room temperature, F. E. Jones (Proc. 1963 Intern. Symp. Humidity and Moisture, Washington, D.C.), Book, Humidity and Moisture. Measurement and Control in Science and Industry, **1,** Principles and Methods of Measuring Humidity in Gases, Sec. III, Paper 37, pp. 361–365 (Reinhold Publ. Corp., New York, N.Y., 1965).

An investigation of psychrometric measurement techniques in air-conditioning calorimetry, J. C. Davis and P. R. Achenbach (Proc. 1963 Intern. Symp. Humidity and Moisture, Washington, D.C.), Book, Humidity and Moisture. Measurement and Control in Science and Industry. **2,** Applications, Sec. IV, Paper 37, pp. 303–313 (Reinhold Publ. Corp., New York, N.Y., 1965)

Calculation of the temperature of a flat-plate wet surface under adiabatic conditions with respect to the Lewis relation, T. Kusuda (Proc. 1963 Intern. Symp. Humidity and Moisture, Washington, D.C.), Book, Humidity and Moisture. Measurement and Control in Science and Industry. **1,** Principles and Methods of Measuring Humidity in Gases, Sec. I, Paper 2, pp. 16–32 (Reinhold Publ. Corp., New York, N.Y., 1965).

Clinical behavior of *o*-ethoxybenzoic acid-eugenol-zinc oxide cements, S. Civjan and G. M. Brauer, J. Dental Res. **44,** No. 1, 80–83 (Jan.–Feb. 1965).

Control of relative humidity and temperature in rubber laboratory of National Bureau of Standards, F. L. Roth and R. D. Stiehler (Proc. 1963 Intern. Symp. Humidity and Moisture. Washington, D.C.), Book, Humidity and Moisture. Measurement and Control in Science and Industry. **2,** Applications, Sec. III, Paper 35, pp. 287–292 (Reinhold Publ. Corp., New York, N.Y., 1965).

Measurement of radiation dose distributions with photochromic materials, W. E. McLaughlin and L. Chalkley, Radiology **84,** No. 1, 124–125 (Jan. 1965).

Soil corrosion, W. J. Schwerdtfeger, Encyclopedia of Electrochemistry, pp. 1068–1071 (Reinhold Publ. Corp., New York, N.Y., Mar. 1965).

A theorem on the automorphs of a skew-symmetric matrix, M. Newman, Mich. Math. J. **12,** 61–63 (1965).

On the location of the zeros of some infrapolynomials with prescribed coefficients, J. L. Walsh and O. Shisha, Pacific J. Math **14,** No. 3, 1103–1109 (1964).

On the structure of infrapolynomials with prescribed coefficients, O. Shisha, Pacific J. Math **14,** No. 3, 1039–1051 (1964).

Continuous-absorption hygrometry with a pneumatic bridge utilizing critical flow, W. A. Wildhack, T. A. Perls, C. W. Kissinger, and J. W. Hayes (Proc. 1963 Intern. Symp. Humidity and Moisture, Washington, D.C.), Book, Humidity and Moisture. Measurement and Control in Science and Industry. **1,** Principles amd Methods of Measuring Humidity in Gases, Sec. VI, Paper 53, pp. 552–570 (Reinhold Publ. Corp., New York, N.Y., 1965).

Absolute measurement of W for polonium-210 alpha particles in nitrogen, argon, and argon-methane mixture, Z. Bay and F. D. McLernon, Radiation Res. **24,** No. 1, 1–8 (Jan. 1965).

Atomic lifetime in neon I, J. Z. Klose, Astrophys. J. **141,** No. 2, 814–818 (Feb. 15, 1965).

Comment on the difference between a non-LTE and a pure absorption model for the line-blanketing effect, R. N. Thomas, Astrophys. J. **141,** 333–335 (Jan. 1, 1965).

Description and analysis of the third spectrum of cerium (Ce III), J. Sugar, J. Opt. Soc. Am. **55,** No. 1, 33–58 (Jan. 1965).

Displacement of dislocation images formed in transmission electron microscopy, R. DeWitt, J. Appl. Phys. **36,** No. 1, 329–330 (Jan. 1965).

Effect of temperature on the vacuum ultraviolet transmittance of lithium fluoride, calcium fluoride, barium fluoride, and sapphire, A. H. Laufer, J. A. Pirog, and J. R. McNesby, J. Opt. Soc. Am. **55,** No. 1, 64–66 (Jan. 1965).

Electron density measurements in the magnetically confined arc, C. K. McLane, S. Takeda, W. E. Thomas, Jr., and R. C. Thompson, J. Appl. Phys. **36,** No. 2, 327–341 (Feb. 1965).

On trapped trajectories in Brownian motion, J. L. Jackson and S. R. Coriell, J. Math. Phys. **5,** No. 8, 1075–1078 (Aug. 1964).

Observation of the products of ionic collision processes and ion decomposition in a linear, pulsed time-of-flight mass spectrometer, R. E. Ferguson, K. E. McCulloh, and H. M. Rosenstock, J. Chem. Phys. **42,** No. 1, 100–106 (Jan. 1, 1965).

Oscillator strengths for lines of Fe I between 2500 and 3200 A, R. B. King, K. H. Olsen, and C. H. Corliss, Astrophys. J. **141,** No. 2, 354–363 (Feb. 15, 1965).

Reaction $^{57}Co(p, \alpha)$ ^{56}Fe, M. Barloutaud, R. S. Caswell, J. Gasteblis, A. G. de Pinho, and J. Quidort (Proc. Intern. Congress Nuclear Physics, Paris, France, July 2–8, 1964), Compt. Rend. Cong. Intern. Phys. Nucleaire **II,** 717–719 (Centre National de la Recherche Scientifique, Paris, France, 1964).

Screening effects in elastic electron scattering, E. Zeithler and H. Olsen, Phys. Rev. **136,** No. 6A, A1546–A1552 (Dec. 14, 1964).

Stability of the shape of a solid cylinder growing in a diffusion field, R. L. Parker and S. R. Coriell, J. Appl. Phys. **36,** No. 2, 632–637 (Feb. 1964).

The intensity and spectral distribution of scattered radiation from Co^{60} sources, B. Petree and J. C. Humphreys, Radiology **84,** No. 1, 1929–1930 (Jan. 1965).

The interaction of 350 keV polarized neutrons with oriented Ho^{165} nuclei, R. Wagner, P. D. Miller, T. Tamura, and H. Marshak, Phys. Letters **10,** No. 3, 316–318 (June 15, 1964).

Vapor phase growth kinetics of potassium and mercury crystals, R. L. Parker and S. C. Hardy, Book, Condensation and Evaporation of Solids, Proc. Symp. Condensation and Evaporation of Solids, pp. 649–664 (Gordon & Breech, New York, N.Y., Nov. 1964).

Cosmic noise absorption events at geomagnetically conjugate stations, C. G. Little, E. R. Schiffmacher, H. J. A. Chivers, and K. W. Sullivan, J. Geophys, Res. **70,** No. 3, 639–648 (Feb. 1, 1965).

Fluctuations in a laser beam over 9- and 90-mile paths, W. R. Hinchman and A. L. Buck, Proc. IEEE **52,** No. 3, 305–306 (Mar. 1964).

On the effect of solar disturbances on the low-radiofrequency ionosphere reflection process, J. R. Johler and J. D. Harper, Jr. (North Atlantic Treaty Organization Advisory Group for Aeronautical Research and Development. Avionics Panel. 6th Symp. Ionospheric Research Committee, AGARD., Naples, Italy, 1961), Book, The Effect of Disturbances of Solar Origin on Communications, ed. G. J. Gassman, pp. 303–304 (Pergamon Press, Inc., New York, N.Y., 1963).

**Publications for which a price is indicated are available by purchase from the Superintendent of Documents, U.S. Government Printing Office, Washington, D.C. 20402 (foreign postage, one-fourth additional). Reprints from outside journals and the NBS Journal of Research may often be obtained directly from the authors.*

SJR-C/JUNE 46129
UNIVERSITY MICROFILMS INC
SERIALS SECTION
313 NORTH FIRST ST
ANN ARBOR MICH

UN
GOVERNMENT PRINTING OFFICE
DIVISION OF PUBLIC DOCUMENTS
WASHINGTON, D.C. 20402
OFFICIAL BUSINESS

POSTAGE AND FEES PAID
U.S. GOVERNMENT PRINTING OFFICE

JOURNAL OF RESEARCH of the National Bureau of Standards Vol. 69C, No. 3 July–September 1965
C. Engineering and Instrumentation

Contents

	Page
Two-terminal dielectric measurements up to 6×10^8 Hz. Martin G. Broadhurst and Anthony J. Bur.	165
Improved ten-picofarad fused silica dielectric capacitor. R. D. Cutkosky and L. H. Lee.	173
Errors in the series-parallel buildup of four-terminal resistors. Chester H. Page.	181
Centerable rotator for measuring properties of crystals. Charles P. Saylor and Herbert B. Lowey.	191
Equipment for single-crystal growth from the melt suitable for substances with a low melting point. Avery T. Horton and Augustus R. Glasgow.	195
Phase and amplitude contrast microscopy in partially coherent light. M. De and P. K. Mondal.	199
Exposure time relations for Kossel microdiffraction photographs. H. Yakowitz and D. L. Vieth.	213
Cartesian diver as a density comparator. Horace A. Bowman and Randall M. Schoonover.	217
Cryogenic behavior of selected magnetic materials. J. J. Gniewek and E. Ploge.	225
Publications of the National Bureau of Standards.	239

Library of Congress Catalog Card Number: 62–3900

For sale by the Superintendent of Documents, U.S. Government Printing Office, Washington, D.C., 20402. Price 75 cents (single copy). Subscription price: $2.25 a year; 50 cents additional for foreign mailing.
UNITED STATES GOVERNMENT PRINTING OFFICE, WASHINGTON : 1965